NASA Technical Memorandum 107130

Evaluation of F/A–18A HARV Inlet Flow Analysis With Flight Data

C. Frederic Smith, Steve D. Podleski
NYMA, Inc.
Brook Park, Ohio

Wendy S. Barankiewicz
Lewis Research Center
Cleveland, Ohio

Susan Z. Zeleznik
NYMA Inc.
Brook Park, Ohio

December 1995

National Aeronautics and
Space Administration

Evaluation of F/A-18A HARV Inlet Flow Analysis with Flight Data
Final Report

C. Frederic Smith, Steve D. Podleski
NYMA, Inc.
Brook Park, Ohio

Wendy S. Barankiewicz
Lewis Research Center
Cleveland, Ohio

Susan Z. Zeleznik
NYMA Inc.
Brook Park, Ohio

Table of Contents

List of Tables

List of Figures

Nomenclature

C_p	$\frac{P-P_\infty}{0.5\rho_\infty V_\infty^2}$
Corrected flow rate	$\frac{\dot{m}\sqrt{\theta}}{\delta}$
Distortion (D2)	$\frac{P_{t_{max}}-P_{t_{min}}}{P_{t_{avg}}}$ at engine face
FS	Fuselage Station in full scale inches (FS = 0 at 60.5 inches ahead of nose)
$\dot{m}$	mass flow rate
P	Local static pressure
P_∞	Free-stream static pressure
P_t	Local total pressure
$P_{t_{avg}}$	Average total pressure at engine face
P_{t_∞}	Free stream total pressure
$P_{t_{min}}$	Minimum total pressure
$P_{t_{max}}$	Maximum total pressure
Recovery	$\frac{P_{t_{avg}}}{P_{t_\infty}}$ from 40 probe rake
S	Wing Span
$T_{t_{avg}}$	Average total temperature at engine face
V_∞	Free-stream velocity
y^+	$\frac{y\sqrt{\tau_w/\rho}}{\nu}$
Z	Spanwise Distance
α	Angle-of-attack
β	Angle of yaw (+ Windward, - Leeward)
δ	$\frac{P_{t_{avg}}}{14.696 lb/in^2}$
ν	Viscosity
ρ_∞	Free stream density
ρ	Density
τ_w	Wall shear stress
θ	$\frac{T_{t_{avg}}}{519^\circ R}$

Summary

The F/A-18A aircraft has experienced engine stalls at high angles-of-attack and yaw flight conditions which were outside of its flight envelope. Future aircraft may be designed to operate routinely in this flight regime. Therefore, it is essential that an understanding of the inlet flow field at these flight conditions be obtained. Due to the complex interactions of the fuselage and inlet flow fields, a study of the flow within the inlet must also include external effects. Full Navier-Stokes (FNS) calculations on the F/A-18A High Alpha Research Vehicle (HARV) inlet for several angles-of-attack with sideslip and free stream Mach numbers have been obtained. The predicted forebody/fuselage surface static pressures agreed well with flight data. The surface static pressures along the inlet lip are in good agreement with the numerical predictions. The major departure in agreement is along the bottom of the lip at 30° and 60° angle-of-attack where a possible streamwise flow separation is not being predicted by the code.

The circumferential pressure distributions at the engine face are in very good agreement with the numerical results. The variation in surface static pressure in the circumferential direction is very small with the exception of 60° angle-of-attack. Althought the simulation does not include the effect of the engine, it appears that this omission has a second order effect on the circumferential pressure distribution. An examination of the unsteady flight test data base has shown that the secondary vortex migrates a significant distance with time. In fact, the extent of this migration increases with angle-of-attack with increasing levels of distortion. The effects of the engine on this vortex movement is unknown. This implies that the level of flow unsteadiness increases with increasing distortion. Since the computational results represent an asymptotic solution driven by steady boundary conditions, these numerical results may represent an arbitrary point in time. A comparison of the predicted total pressure contours with flight data indicates that the numerical results are within the excursion range of the unsteady data which is the best the calculations can attain unless an unsteady simulation is performed.

1.0 Introduction

1.1 Overview

The High Alpha Technology Program (HATP), is part of a cooperative program, among NASA's Lewis, Langley, Ames, and Dryden facilities Ref. [1]. The overall objective of the NASA Inlet Experiments portion of the HATP, which NASA Lewis leads, is to develop and enhance inlet technology that will ensure high performance and stability of the propulsion system during aircraft maneuvers at high angles-of-attack. To accomplish this objective, Computational Fluid Dynamics and flight experiments are used to obtain steady-state and dynamic data.

The flight regime being investigated represents an especially challenging problem for high speed inlets because of the adverse effect thin lips have on recovery and distortion at these conditions. This results in reduced thrust and stability of the propulsion system. Other propulsion system/airframe integration programs have provided an experimental data base applicable to maneuverable supersonic aircraft, but not at low subsonic speed/high angle-of-attack conditions.

Several different types of distortions must be considered in the design of these inlets. One type, total pressure distortion, is the most commonly encountered distortion and has received the greatest attention to date. It can result when the inlet is at high angle-of-attack and/or angle-of-side-slip conditions. Total pressure distortion of a quasi-steady type can result from a yaw rate maneuver at high angles-of-attack. Another type of distortion is caused by swirl (vortices with an axial velocity component), such as when an inlet ingests a vortex shed from the aircraft during maneuvers. Swirl can also be encountered when an inlet is attached to an S-shaped (offset) duct, and is due to secondary flow generation in the duct. Any of these types of distortion will adversely effect engine stability. Severe distortion of any one type can cause engine stall. Combining several types of moderated distortion can also cause engine stall.

The HATP utilizes the F/A-18A High Alpha Research Vehicle (HARV) for full scale validation of the technologies associated with high angle-of-attack aerodynamics and post wing stall control. The HARV is an ideal vehicle because of its high angle-of-attack capability and stable propulsion system characteristics. During the Navy envelope expansion program, the F/A-18A aircraft experienced some instances of thrust loss, flameout and/or engine stall when performing dynamic maneuvers outside the normal flight envelope. This might be a propulsion system/airframe integration problem

caused by high angle-of-attack and yaw rates or steady state high angle-of-attack and yaw, or it could be a propulsion-related problem. To investigate the cause of these anomalies, NASA obtained the HARV from the Navy, where it was used as the unique high alpha test aircraft during the F-18 development program.

1.2 Experiments

The experimental part of the program consists of expanding the data base to increase inlet angle-of-attack capability and to determine the effect of ingesting vortices on engine stall. Prior experiments to increase inlet angle-of-attack capability considered only isolated inlets. The installation effects on inlet performance was not investigated. The HARV represents an excellent aircraft on which to focus research interest because of its well defined inlet/forebody configuration and its high angle-of-attack capability.

Both diagnostic and research flights were conducted at Dryden as part of the Inlet Experiments Program. The diagnostic flights determined whether the loss of thrust, flameout, and engine stall previously encountered in Navy F-18 aircraft envelope expansion flights were due to inlet-related phenomena or a fuel system anomaly. The research flights gathered detailed information inside, as well as outside, the inlet duct.

The research portion of the flight program acquired steady state and dynamic data to investigate inlet-related problems suggested from diagnostic flights or occurring during research flights, investigate scale effects, generate a data base for CFD code evaluation, and investigate effects of the method used to pump air through the inlet during subscale model tests.

Steady state tests were conducted in the Ames National Full-Scale Aerodynamic Complex (NFAC) using a full scale F-18 aircraft model but with engines removed. This is a flow through model with a maximum design corrected airflow of 85 percent. A study has been completed which determined what is required to increase the airflow to 100 percent.

1.3 Computational Fluid Dynamics

The computational part of the Inlet Experiments Program consists of applying and evaluating computational tools. This will be concerned solely with steady state conditions, since the codes

have not matured to the point where they can be used for dynamic data. CFD codes will be evaluated by using data from the flight test data base.

Four facilities were involved in the CFD effort in one way or another. Langley used the CFL3D code Ref. [2] and Ames the F3D code Ref. [3] to model the external aerodynamics of the HARV with faired over inlets. Lewis worked with both these centers. The initial plan was to use the output of their codes to provide input to the Lewis code, NPARC, which would be dedicated to flow in the inlet duct. Lewis found it easier to perform the complete installed inlet analysis (including external flow simulation) with NPARC than to get input from the codes used by Langley and Ames. Dryden provided the data from the HARV flights for the evaluation the NPARC results.

2.0 Experimental Program

The flight data was obtained using a specially equipped F/A-18A HARV aircraft. This aircraft has rows of static pressure taps located at several axial stations along the fuselage and LEX upper and lower surfaces. The inlet lip and duct contained ESP (low response, 67 hz) and Kulite (high response, 2143 hz) static pressure probe pairs located at several circumferential and axial locations. At the engine face, a rake consisting of 40 ESP and Kulite total pressure probe pairs distributed on an equal area basis were used to measure the total pressure distortion as a function of time.

The data reduction process consisted of the following steps:

1. The data base is created by time synchronizing the inlet parameters with the aircraft parameters which were collected on separate systems.

2. The Kulite pressure data is temperature and bias corrected. The bias correction adjusts the Kulite drift by normalizing the DC component to the steady-state (ESP) pressure measurement.

3. Data is checked for malfunctioning probes and data spikes using the General Electric Quality Check Program (QCP). If a probe malfunctions, it is replaced by a linear interpolation between adjacent circumferential probes. Data spikes are eliminated from the database.

4. The General Electric HARV Analysis Program (HAP) program filters the high response bias corrected Kulite data to a low-pass cut-off frequency of 100 Hz. It also calculates various inlet performance parameters (i.e. distortion, mass flow rate, recovery) and generates total pressure contour plots.

3.0 Numerical Modeling

In this section, the major features of the NPARC code are presented along with a discussion of the boundary conditions used. A brief discussion of the development of the computational grid is also presented.

3.1 NPARC Code

The NPARC code, Version 2.0 Ref. [4] solves the full three-dimensional Reynolds averaged Navier-Stokes equations in strong conservation form using the Beam and Warming approximate factorization scheme to obtain a block tridiagonal system of equations. Pulliam's scalar pentadiagonal transformation provides for an efficient solver. The code uses the Baldwin-Lomax turbulence model Ref.[5,6] along with several other models which include the RNG Ref. [7], Baldwin-Barth Ref. [8] and $\kappa - \epsilon$ Ref. [9] turbulence models. The calculations presented in this study were done using the Baldwin-Barth, Baldwin-Lomax and $\kappa - \epsilon$ turbulence models. The Baldwin-Barth turbulence model was incorporated after much of the non-zero sideslip calculations were completed. A couple of these cases were revised with the Baldwin-Barth model. The comparisons with the Baldwin-Lomax results were very similar and did not warrant the use of limited computational resources to rerun all cases. More discussion on the turbulence model comparisons is in Section 6.3. The zero sideslip cases were revised using the Baldwin-Barth turbulence model because they required significantly less computational time. The implicit scheme uses central differencing with artificial dissipation to eliminate oscillations in the solution associated with the use of central differences. The code allows the use of multiple grid blocks. Trilinear interpolation Ref. [10] is used to transfer information at the grid block interfaces.

3.2 Boundary Conditions

The farfield type boundary conditions were imposed along the outer computational boundaries. This type of condition uses a one-dimensional Riemann invariant to maintain the free-stream flow conditions. Along the windward side of the airframe, no-slip, adiabatic conditions are specified. Along the leeward side of the aircraft, inviscid flow is specified. The static pressure at the engine face was adjusted to obtain the rake corrected mass flow rate (144 lbm/sec) based upon total

pressure at the engine face plane obtained from an average of 40 total pressures in a configuration of 8 equally spaced legs with 5 equal area total pressure locations per leg. Slip conditions are assumed along the plane of symmetry of the aircraft for zero sideslip cases.

3.3 Grid Generation

The grid used to model the F/A-18A in this study was a very important factor in obtaining a good solution. Accurate modeling of the geometry and judicious clustering of grid points are needed for a correct numerical solution and an economical computation. The complex multi-block grid used for these calculations was created with the GRIDGEN, version 6.0, grid generation package Ref. [11]. This grid generator has proven to be very effective in creating complex multi-block grids.

A geometry data base which accurately defines the surface geometry is essential for the creation of a good grid. The data base used to create the grid for this study was obtained from McDonnell Aircraft Company. The data base consisted of x,y,z coordinate points given at axial cuts along the fuselage. The data base included the definition of the fuselage, LEX, wing, tail, ramp, inlet, inlet lip, LEX slot and upper and lower diverters. A shade rendering of the computational model is shown in Fig. 1a.

Due to the complex interactions between the fuselage flow field and the inlet flow field, the forebody, fuselage, LEX, ramp and wing were all included in the grid. The horizontal tail, vertical tail, and the nozzle were not modeled because of their minimal effects on the inlet flow field. The wing leading edge flap, is deflected down 34 degrees when the aircraft is at 30 degrees angle-of-attack or greater and was modeled undeflected for $\alpha = 3°$. A pair of vortex generators located at the bottom wall of the inlet were modelled but calculations were limited to two cases. It was found that for high distortion, they had very little effect.

The data base was modified in selected areas using the program I3GVIRGO (Interactive Graphics for Geometry Generation). This program was written at the Wright Research and Development Center, and it runs interactively on the IRIS workstation. It is mainly used for geometry database manipulation, such as rotations, translations, and scaling. It can also be used to join together, or split apart surface definitions. For instance, the top of the LEX was split from the bottom of the LEX in order to generate a viscous grid under the LEX and an inviscid grid above the LEX.

I3GVIRGO is also useful for geometry generation using lines, elliptic arcs, and curves.

The first program in the GRIDGEN grid generation package is GRIDBLOCK. This is an interactive program which runs on the Iris workstation. This program was used to create the blocking structure of the grid. The blocking structure was affected most significantly by the surface geometry. It is difficult to create adequate grid blocks around areas of complex geometry, such as the inlet lip. The advantage GRIDBLOCK has over other grid generators is the graphical representation of the blocking structure. This helps to keep the user more organized and allows for the discovery of block anomalies before time is spent creating the grid itself. The blocking structure was also affected by the flow solver boundary condition requirements and block interface requirements. A flow solver, NPARC for example, which allows very general boundary condition specification and grid embedding can make the grid generation process easier. Another factor in determining the blocking structure was the maximum number of grid points per block allowed by computer memory limitations. However, this becomes less important with the availability of large memory computers.

The blocks are constructed in GRIDBLOCK by creating each block one edge at a time. These edges can be created with straight lines, elliptic arcs, and smooth cardinal spline curves. Edges which must lie on a data base network are created by tracing the desired edge shape onto the database network.

The blocking structure used for the F-18 consists mainly of O-grids wrapped around the fuselage, in the cross-flow plane. The entire F/A-18 blocking structure can be seen in Figure 1b. The inlet block is an O-grid extending from the inlet lip to the compressor face. The blocks were created such that the blocks under the LEX could be run viscous, while the blocks over the LEX could be run Euler. This was done because it was felt that the viscous effects above the LEX did not significantly effect the flow into the inlet. This also decreased the required number of grid points and thus the run times. Blocks were extended approximately one body length away from the surface in order to minimize the effects of the freestream boundary condition on the solution near the inlet. The GRIDBLOCK program also requires specification of the computational directions and dimensions of each block. The boundary conditions may also be specified for each face in the block. This makes it possible for a flow solver input file to be created in GRIDGEN3D, which will be discussed later.

Once the blocking structure was completed, the second GRIDGEN program, GRIDGEN2D, was used to create the grid on the six block faces. This program, like GRIDBLOCK, runs interactively on the Iris. The first step in GRIDGEN2D is to define the grid spacing on the edge of a block face. The shape of each edge is usually defined with the shape which was created for that edge in GRIDBLOCK. GRIDGEN2D contains a variety of stretching functions for point distribution on face edges. The stretching function which was used in the majority of cases for this grid was the one based on Vinokour's functions. The grid for viscous flow was packed so that spacing at the wall was .0002". This produced a y^+ approximately 1.

After the edges on a face are defined, the points on the interior of the face are defined. An algebraic solver using transfinite interpolation with arc based interpolants was used to initialize the grid for most faces. If the resulting grid needed smoothing or orthogonality along an edge, the elliptic solver was used. The Thomas and Middlecoff along with Sorenson's method proved to be the most effective.

The third GRIDGEN program, GRIDGEN3D, is a batch code that runs on a Cray computer. It creates the grid in the interior of each block. Most of the blocks only required the algebraic solver to initialize the interior points. However, some blocks with excessive skewness required the elliptic solver to smooth the grid. GRIDGEN3D also creates a NPARC input file based on the boundary conditions specified in GRIDBLOCK. The final grid contained approximately 1 million grid points for the zero sideslip cases and approximately 2 million points for the non- zero sideslip simulations. A grid block description for the symmetrical model is shown in Table 1. The grid on the symmetry plane and on the F-18 surface can be seen in Figure 1c.

One of the main problems with creating a multi-block grid is maintaining correct interfaces between grid blocks. Many multi- block CFD codes require that all the face points of an interface must lie along the boundaries of the adjoining block. This requirement is hard to meet with non-contiguous interfaces with curved edges. This is most difficult when a grid is packed very closely, for a viscous wall boundary condition, at one of these edges. The only solution is to carefully space the grid points along the curved edge so that each point on the edge lies entirely along the other block's boundary, or project one overlapping surface onto another.

3.4 Numerical Issues

For such a complex problem, determining the convergence of the solution is not a straightforward task. Residuals are not very reliable since they tend to drop a few orders of magnitude and then level off for complex viscous flows. Therefore, we follow the flow quantities of interest as the solution iterates to determine when these quantities stop changing or the changes per iteration become insignificant. Several quantities are presented for convergence criteria in the following discussion.

The calculated forces on the aircraft served as one measure of convergence of the external flow field. The predicted lift and drag coefficients varied by less than one percent as the solutions were converged. The surface static pressure distributions maintained nearly constant values as the solution iterated. The external force coefficients converged more rapidly than the internal flow parameters. Inlet flow distortion and total pressure recovery changed less than 2% and 1%, respectively. For the inlet duct flow, the variation in mass flow rate at each axial computational station was compared to the entrance value. The variation was within one percent of the entrance values.

4.0 Background for Computational Work

At the time this work began, there was a large question of the capabilities of CFD codes to accurately predict the installation effects of an inlet operating at high angle-of-attack, low Mach number conditions. Therefore, the initial objective was to assess the capabilities of the NPARC code to handle this type of flow. The initial computational grid was generated using the existing F/A-18A geometry database which was made available by McDonnell-Douglas. Since the company's interests are primarily external flow about the airframe, very little detail was available for the region near the inlet. The significant missing regions were the slot, upper and lower diverters, leading edge flap, and the inlet lip.

Results indicated that the NPARC code could be used to analyze these types of flow fields Ref. [12,13]. However, several deficiencies in the solutions were observed. The surface static pressure distribution around the lip was very "rough" and the pressure gradients were not defined well. Also, the predicted inlet recovery was much lower than experimental data. The total pressure distortion pattern indicated that the LEX vortex had migrated to the engine which also was not apparent in the experimental total pressure contours.

After reviewing these results, it was decided to obtain a complete definition of the aircraft and to include all the details along the forebody, near the inlet (LEX slot, upper and lower diverters, leading edge flap and inlet lip). This complete model is the one used for the computations presented in this report and discussed in the grid generation section. Several papers and reports describing various aspects of this work are cited in Ref. [14,15,16,17,18,19,20,21,22,23].

5.0 Results

5.1 External Flow

In this section the external flow is visualized by free and restricted particle traces using the FAST graphics program Ref. [24]. The effects of angle-of-attack and sideslip on the external flow is discussed. Since only one inlet was instrumented for the flight tests, the HARV was flown twice for positive and negative sideslip to simulate both inlets. Hence, the leeward and windward sides of the aircraft are also referred to as negative and positive beta, respectively.

Alpha=30°, beta=±10°, 0°, mach=0.3

Restricted and free particle traces are shown by the upper figure of Fig. 2a for the windward side of the aircraft, as computed by NPARC for an angle-of-attack of 30°, sideslip angle of 10° and Mach number of 0.3. The restricted traces simulate oil flows or friction lines and therefore remain on the surface of the aircraft. Slightly off center of the bottom centerline of the aircraft is the attachment line which is analogous to the stagnation point in 2-D flow. A weak separation line runs along the bottom of the fuselage and continues, although slightly weaker, on the ramp/splitter plate.

Another attachment line can be seen on the nacelle, slightly behind the highlight. A herring-bone pattern reattachment line can be seen on the underside of the LEX. The separation and reattachment lines are the footprint of a vortex that is generated by the corner of the lower surfaces of the LEX and fuselage walls. Some of this vortex is ingested by the inlet and the remainder is diverted by the ramp/splitter plate.The particle trace that is seen above the aircraft is the flow from the diverter that has been caught by a large reverse flow region above the aircraft. The lowest figure of figure 2a shows the restricted and free particle traces on the leeward side of the aircraft. The separation line is better defined and the vortex is stronger with a larger portion of the vortex ingested by the inlet. Particle traces show that the vortices ingested by both inlets are swallowed by the inlet boundary layer.

The results for 0° sideslip the middle figure of Fig. 2a appear to resemble the leeward particle traces more than the windward surface. The separation line is fairly "tight" with a significant amount of LEX vortex ingestion as is indicated on the leeward side results. The windward side

indicates more of the LEX vortex has been captured by the lower diverter behind the ramp. This may be consistent with wind on the windward side pushing the LEX vortex closer to the fuselage than experienced by the leeward side.

Alpha=30°, beta=±10°, 0°, mach=0.4

The restricted particle traces on the windward side of the aircraft, shown in the bottom figure of Fig. 2b have a more diffuse separation line along the fuselage and ramp/splitter plate. The free particle traces show a portion of the LEX/fuselage vortex taken by the side and upper diverters and the remainder of the vortex ingested by the inlet. The attachment line on the lower surface of the LEX is further inboard than that on the leeward side.

The restricted particle traces on the leeward side of the aircraft, shown in the top of figure of Fig. 2b, show two distinct parallel separation lines running along the fuselage. The LEX lower surface attachment line is further outboard than that at Mach 0.3 which results in a larger area of cross-stream separation and LEX/fuselage vortex. This vortex seems to be stronger than that on the windward side. The particle traces for 0° sideslip are very similar to the leeward side.

Alpha=50°, beta=±5°, mach=0.3

Particle traces for an angle-of-attack is 50 deg., sideslip angle of 5 deg. and the Mach number is 0.3, shown in Fig. 2c show that the leeward side has two pairs of vortices under the LEX. The restricted particle traces show a complex pattern of saddle points in the separation and reattachment lines. One vortex pair occurs near the LEX apex where one portion of the vortex moves upstream and is engulfed by the flow over the forebody. The other portion of the vortex moves downstream where it meets a vortex from the other pair; the combined vortices flow around the LEX leading edge into the aircraft wake. The other pair originates at about 30% of the LEX chord; most of the downstream moving vortex is ingested by the inlet with remainder caught by the diverter.

The windward side shows one vortex pair that originates near the LEX apex. The separation and reattachment lines have a simple herring-bone pattern similar to those at the lower angles of attack. Most of the vortex is caught by the diverter. The weak separation line on the ramp/splitter plate shows that a vortex weaker than that on the leeward side is ingested into the inlet. The traces that are labelled as "slot back flow" are the traces swallowed by the diverter. It seems that this case is a transition case between the angles-of-attack of 30 deg. and 60 deg.

Alpha=60°, beta=±5°,0°, mach=0.3

Restricted and free particle traces on the windward side of the aircraft, as computed by NPARC for an angle-of-attack of 60°, sideslip angle of 5° and Mach number of 0.3, are shown by the upper figure of Fig. 2d. The flow is more complex as some of the flow moves upstream in a manner similar to stagnation flow. About midway between the LEX apex and the inlet, the flow is split into two with one half moving upstream, and the other half moving downstream; therefore less of the vortex is ingested by the inlet. The main separation lines on the lower fuselage and reattachment lines on the lower LEX surfaces originate at mid fuselage and end at the LEX apex for the upstream portion and at the diverter for the downstream portion. The sudden increase in curvature of the restricted particle traces on the fuselage near the ramp/splitter plate is due to the influence of the diverter wedge. Again the traces seen above the aircraft is the flow from the diverter caught in a reverse flow above the aircraft. The attachment line on the nacelle is farther back from the highlight as compared to the lower angle-of-attack.

The bottom figure of figure 2d shows the restricted and free particle traces on the leeward side of the aircraft. The vortices are stronger with a larger portion of the downstream vortex ingested by the inlet.

The particle trajectories for 0° sideslip differ from the non- zero results. The major departure is in the LEX vortex structure. There appears to be a second split of the LEX vortex near the LEX apex similar to the 50° alpha and ±5° sideslip case. The 0° sideslip results indicate a small amount of LEX vortex ingestion by the inlet as is the case for the leeward side of the aircraft in the nonzero sideslip cases.

5.2 Forebody/LEX Surface Static Pressures

Figure 3a shows the locations of surface pressure taps on five forebody and three LEX stations (Ref 25). Figure 3b-d compares the calculated and test surface pressures. The circumferential station of 0° on the forebody is defined as the 6 o'clock location and the angle increases counter-clockwise, looking aft. The test conditions are not exact duplicates of the calculated conditions but are the test conditions nearest those to calculations. These tests were done to study external aerodynamic problems, during a different test program.

At an angle-of-attack of 30°, sideslip angle of 10° and Mach number of 0.3 shown in Fig. 3b, comparisons are good for fuselage stations, FS 70, FS 85 and FS 107. FS 142 shows two spikes in the pressure distribution curves. One spike, at a circumferential angle near 90°, is due to an antenna that is not modeled by the grid. The second spike, at a circumferential angle near 150°, is the footprint of the primary vortex which is not captured by calculations because of the relatively coarse gridding of the forebody. At FS 184 there is a problem with the data from 0° to 180°. Comparisons of the surface pressure of the lower LEX surface show similar trends in pressure profile to test. The spike in the calculation curve at z/s=0 is due to the definition of z/s=0; z/s=0 is defined as the junction of the LEX and fuselage and the left and right LEX are separated by the fuselage diameter at that station.

Results for an angle-of-attack of 60°, sideslip angle of attack 5° and Mach number of 0.3 are shown in Fig. 3c. Although calculations show pressure distributions lower than test, the comparison remains satisfactory except for FS 107 and FS 142 where the secondary vortex peaks are stronger than that at the lower angle-of-attack. Calculations at FS 184 do not compare well except for the trends. The surface pressure profiles on the upper surface of the LEX are flat indicating that the leading-edge-generated vortices have collapsed. A small, separate side study of the calculations of these vortices showed there may be vortex shedding during the early stages of the calculations. The end result is the absence of the vortices on the upper surfaces.

Results for an angle-of-attack of 50°, sideslip angle 5° and Mach number of 0.3 are compared with data in Fig. 3d. The effects of sideslip for an angle-of-attack of 30°, sideslip angle 0° and 10° and a Mach number of 0.4 are shown in Fig. 3e.

5.3 Internal Flow

In this section the internal flow field is described by particle traces and vortex cores generated by the FAST graphics program.

Alpha=30°, beta=±10°,0°, mach=0.3

Calculated restricted and free particle traces for the windward inlet at Mach number of 0.3, an angle-of-attack of 30° and sideslip angle of 10°, are shown by Fig. 4a-b. The restricted traces show no evidence of flow separation along the lower lip but there is cross-stream separation as shown by a separation line that runs along the lower inboard edge of the inlet. The free traces that terminate in the low pressure well at the fan face shows that the origin of this flow is from the lower half of the lip. Figure 4b, a side view of the particle traces, shows a separation zone on the outboard lateral edge of the lip. A vortex lifts off the corner of the separation zone and migrates parallel to the leading edge until it is convected downstream by the unseparated flow on the lower lip where it dissipates.

For the same conditions as above, the calculated restricted and free particle traces for the leeward inlet are also shown in the bottom figure of Fig. 4b. Again, there is no evidence of flow separation on the lower lip, but there is cross-stream separation along the lower inboard duct wall. Free traces, terminating at the low pressure well at the engine face, originate from the lower lip, shows a separation zone on the outboard lateral edge of the lip that is smaller than that on the windward side. The resultant vortex is weaker and quickly dissipates as it migrates parallel to the leading edge. The windward inlet lateral edge, exposed to a relative positive angle-of-attack induced by sideslip, would be expected to have a larger separation zone.

Although not shown, calculations done with the Baldwin-Barth turbulence model for an angle of attack of 30°, a sideslip angle of 10° and Mach number of 0.3, show similar simulated oil flow patterns to the Baldwin-Lomax/PD Thomas turbulence model calculations, but for a weaker liftoff vortex on the windward lip.

The 0° sideslip results indicate a closer resemblance to the leeward side than the windward side as shown in the middle figure of Fig. 4b. In particular, the vortex core along the outboard side of the inlet lip is more pronounced than the leeward side, but much less prominent than the

windward side vortex core. This is consistent with the 0° sideslip case being "between" the 10° sideslip results.

Alpha=30°, beta=±10°, 0°, mach=0.4

Free and restricted particle traces for the windward inlet at the Mach number of 0.4 and an angle-of-attack of 30° and sideslip of ±10°, are shown in Fig. 4c-d. The flow pattern along the lower lip is similar to and the cross-stream separation line is weaker than the Mach 0.3 case. The separation region along the outboard edge of the lip is smaller with weaker and shorter liftoff vortices. The attachment line along the outer edge of the lip is nearer the highlight than the Mach 0.3 case.

Free and restricted particle traces for the leeward inlet are also shown in Fig. 4c-d. There is no evidence of separation on the outboard edge of the lip. The cross-stream separation line is weaker than that of the Mach 0.3 case. This is also the case for 0° sideslip.

Alpha=50°, beta=±5°, mach=0.3

Figures 4e-f show the traces inside the leeward inlet. A moderate region of streamwise flow separation is seen on the outboard edge of the inlet. A vortex lift-off the focus located on the upper edge of the separation zone and migrates down the lip until it is caught by the main flow through the inlet and flows downstream to the low total pressure region on the engine face. The usual cross-stream separation line can also be seen. A similar but smaller region of streamwise separation on the leeward inlet outboard edge is seen in Fig. 4e-f. The lift-off vortex is dissipated as it moves down the lip. A zero degree sideslip case was not calculated for these conditions.

Alpha=60°, beta=±5°,0°, mach=0.3

The upper figures of figures 4g-h show the particle traces on the windward inlet at a Mach number of 0.3, an angle-of-attack of 60° and sideslip angle of 5°. The separation zone on the lateral edge now extends to over half of the lower lip. A strong vortex lifts off the upper corner of the separation zone, migrates along the lip leading edge and then moves downstream to terminate in the low pressure well at the engine face.

Particle traces on the leeward inlet are shown in the lower figures of Figures 4g-h. The separation zone, which originated from the lateral edge, now covers the whole lower lip. Two strong vortices can

now be seen; one vortex originates from the upper corner of the separation zone and another vortex lifts off the lip surface from the opposite corner of the separation zone. Both vortices migrate down the lip until they meet at the lower inboard corner of the inlet where they are convected downstream to terminate in the low pressure well at the engine face.

The 0° sideslip case again resembles the leeward inlet move than the windward. The surface separation lines obtained for 0° sideslip are very similar to those obtained for the leeward side.

5.4 Inlet Lip and Engine Circumferential Pressures

In this section, the predicted surface pressures along the inlet lip and at the engine face are compared with flight data in Figure 5. With the observer facing downstream, the 12 o'clock location of the inlet face is the 0° station; the 90° station the outboard edge; the 180° station is at 6 o'clock; and the 225° station is the lower junction of the inlet/fuselage walls. There is only one data point inside the duct and this probe is located at 180°.

Non-zero sideslip conditions were not obtained for 3° angle-of-attack. At 3° angle-of-attack, the comparison of the data with NPARC results is very good as shown in Fig. 5a-b. This is consistent with attached flow more likely being present at the low angle-of-attack flight condition. For this case, the leeward (0° position) minimum pressure is lower than the windward (180° position). This is due to the top portion of the inlet highlight region being thinner than the bottom region. There is one data point for the inlet duct at the 180° station.

Figures 5c and 5d compares the calculated and time-averaged flight test surface pressures on the inlet lip and duct at several circumferential stations; the flight conditions are for a nominal angle-of-attack of 30° and sideslip angle of ±10°,and Mach numbers 0.3 and 0.4, respectively. Comparison between test and calculations is good except that peak pressures at stations 0°, 90° and 225° are not captured. The broad pressure profile at the base of the pressure peak shown by test data at station 180° may imply a thick boundary layer or boundary layer separation that is not reflected by calculations. The discontinuity in the pressure profile shown by the calculations is due to the block interface between the lip and duct grids.

The results of doubling the lip grid block dimensions in all directions are compared to the present grid in Ref. 14 for 30° angle-of-attack, 0° sideslip and a Mach number of 0.3 and are not shown in this report. The static pressure distributions obtained with the fine grid [Ref. 14] indicate that the minimum pressure at Station 0° was reached whereas the present grid missed that point. However, along the lower portions of the highlight (Station 180° and 225°), the fine grid results were very similar to the present grid. Since the data indicates a thickening boundary layer, a deficiency in the turbulence model may be the source of the discrepancies between NPARC results and data. The agreement between NPARC and data improves with increasing Mach number.

Comparisons of inlet lip and duct surfaces pressures for a Mach number of 0.3, and sideslip

angle of $\pm 5°$, are shown in Fig. 5e and 5f, for angles of attack 50° and 60°, respectively. Again the comparison is good, and the peak pressures are captured by calculations. Test data, again, show the broad pressure profiles at the base of the pressure peaks for stations 180° and 225°. Simulated oil traces, shown later, indicate flow separation on the bottom lip but this separation is not reflected by calculated pressure profiles. The data and results for 0° sideslip fall between the leeward and windward results and data for 30° and 60° angle-of-attack.

A comparison of the engine face circumferential pressure flight data with the NPARC results are shown in Figure 6 for several angles-of-attack and Mach numbers. It is important to note that the NPARC boundary condition at the engine face was an extrapolation of the static pressure gradient for β=0 and a constant value for non-zero sideslip. This gradient was scaled by a single pressure value to adjust the mass flow rate to the desired value. The exception to this was the 60° angle-of-attack case in which a constant uniform static pressure was applied for 0° sideslip. This was done due to streamwise flow separation occurring with the extrapolated boundary condition. The circumferential pressure gradients determined by NPARC are due only to pressure gradients that develop within the duct without any simulation of the influence of the engine. The experimental pressure gradients are very small with the exception of 60° angle-of-attack. For the 60° angle-of-attack case, the extrapolation of the static pressure gradient may have improved the agreement between the data and the NPARC results. Although the effect of the engine is important, its influence appears not to have an overwhelming effect on the circumferential pressure gradient.

5.5 Inlet Performance

Table 2 gives a summary of the comparison of total pressure recovery and flow distortion at the engine face where a range of min/max values are given for the test data. Again, calculations are taken from the interpolation of the CFD grid unto the flight-test rake grid. In general, the calculated performance values either lie within the min/max test band or are slightly outside the test band; calculations compare better with flight tests as the angle-of-attack increases. In all cases, calculations and tests show that the leeward inlet has a lower performance compared to the windward inlet. This may be due to the leeward inlet being in the wake of the fuselage.

Although not shown in Table 2, the Baldwin-Barth results for an angle-of-attack of 30°, a sideslip angle of 10° and a Mach number of 0.3 shows a 2% point decrease in flow distortion and 1% point increase in total pressure recovery; there was no significant change in total pressure contour shape at the engine face.

The predicted recoveries and distortions obtained for 0° sideslip are more consistent with windward side results than the leeward side at a given Mach number and angle-of-attack. The recoveries were lower and distortions higher on the leeward side than the 0° sideslip results. In fact, the predicted performance on windward side was slightly better than the performance obtained for 0° sideslip. This again is consistent with the 0° sideslip case results following somewhere between the leeward and windward results obtained for non-zero sideslip at a given Mach number and angle-of-attack.

5.6 Inlet Entrance Total Pressure Contours

Alpha=3°, beta=0°, mach=0.3,0.4

From examining the total pressure contours, in Fig. 7a-b, for both Mach numbers, several observations can be made. The first one is that there is a large region of cross-stream separation along the outboard section of the inlet lip. This region diminishes in size with increasing Mach number. This is due to the captured streamline stagnation location moving towards the highlight of the inlet as the free-stream Mach number increases. Another observation is that the boundary layers are fairly thin along the inlet circumference away from the region of flow separation. This indicates that the flow around the inlet lip is contains a minimum amount of losses. There were no

non-zero sideslip cases available for comparison.

Alpha=30°, beta=±10°,0°, mach=0.3, 0.4

For 30° alpha, a similar region of separation can be seen along the outboard section of the inlet entrance in Fig. 7c-d. Again, its size shrinks with increasing Mach number. A comparison with the nonzero beta cases indicates that the windward (+10 deg) inlet total pressure contours resembles more closely the zero sideslip case than the leeward side inlet (-10 deg). This trend appears to indicate that the windward side or "unshielded" inlet capture streamtube stagnates farther outside of the inlet than the leeward side or "shielded" inlet.

Alpha=60°, beta=±5°, 0°, mach=0.3

For 60 deg alpha, the nonzero and zero sideslip cases total pressure contours all appear similar in appearance in Fig. 7e. This is due to the large amount of distortion and flow separation along the lower protion of the inlet lip masking more subtle features of the flow field.

5.7 Engine Face Total Pressure Contours

The last aspect of the internal flow analysis to be examined is the total pressure distortion at the engine face. This topic has several issues associated with it. The major issue is flow unsteadiness which will be discussed in detail and how steady state computations handle this type of flow situation.

The comparison of the NPARC predicted total pressure contours at the engine face with experimental unsteady data are shown in Figure 8 for several mach numbers and angles-of-attack. A complete report on the flight test database is found in Ref. [26]. The experimental contours taken at a point in time were obtained using the General Electric High Alpha Program (HAP). The total pressure contours showing the limits of the migration of the low total pressure region were obtained using the FAST program. Each time slice (1/2143 sec) of total pressure data was placed in a PLOT3D Ref. [27] function file with the rake total pressure probe coordinates in a PLOT3D grid file. Time was treated as the x-axis (k index) in FAST. The migration of the low total pressure region was examined by moving through time along the x-axis using the FAST program. An examination of predicted vector plots (not shown) indicates that this low total pressure region represents

the position of the inlet duct secondary flow vortex for 30° and 60° angles-of-attack. This region represents the location of the inlet lip cross-stream separation which has migrated to the engine face for 3° angle-of-attack.

Several issues are pointed out from studying the comparison of the NPARC results with the flight data. The comparison of the NPARC results with the data indicates a qualitative agreement with the data in terms of the general flow structure. The position and strength of the predicted low total pressure region is different from the data due to the unsteady nature of the flow field as shown in the accompanying total pressure contours. These indicate the extent of the migration of the low total pressure region as a function of time. The strength (total pressure loss in this region) also varied with time. The NPARC results fall within the migration range of this region. The NPARC asymptotic solution may represent a "snapshot" of the dynamic flow field which is at an arbitrary point in time fixed by the boundary conditions imposed. Therefore, the best obtainable solution is one that lies within the excursion of the unsteady flow field. In order to perform an unsteady flow analysis an unsteady engine face boundary condition may be required. From observing the experimental total pressure contours at the engine face as a function of time, the flow field appears cyclical with some randomness requiring a statistical or probability representation of the pressure field at the engine face. The migration range of the vortex or low total pressure region increased with increasing levels of distortion. This indicates that the flow becomes more unsteady as the distortion levels increase. The presence of the engine may have a significant effect on the movement of the secondary flow vortex.

Alpha=3°, beta=0°, mach=0.3,0.4

Having discussed some of the general observations made concerning unsteady flow, the specific comparisons of the NPARC results with the flight data will be made. For 3 deg. alpha, the data indicates very limited amount of unsteadiness for both 0.3 and 0.4 free stream Mach numbers as shown in Fig. 8a-b. The NPARC results indicate a region of very low total pressure near the top of the duct which is not present in the experimental contours. The source of this low total pressure region is a separation which formed along the outboard region of the inlet lip and migrated to the engine face. For this particular case, it appears that either the predicted separation is false or that the mixing in the inlet duct is not adaquate to remove its presence at the engine face. There was

no non-zero sideslip case available for comparison.

Alpha=30°, beta=±10°, 0°, mach=0.3,0.4

For alpha 30 deg. the data indicates an increase in the level of unsteadiness in the flow as indicated by the migration and change in intensity of the low total pressure regions at the engine face as shown in Fig. 8c-d. The unsteadiness is diminished somewhat for a free-stream Mach number of 0.4 as compared with 0.3. The NPARC results indicate that the low pressure region is at 180 deg. while the data shows the low pressure region migrating between 90° and 200° angular positions for 0.3 Mach number and from 135 to 200 deg. for 0.4 Mach number.

For the non-zero sideslip cases, the amount of unsteadiness is similar for both free-stream Mach numbers with the angular position of the low total pressure region moving from 90 deg. to 200 degrees for both cases. The NPARC results for the non-zero sideslip cases appear to shift the low total pressure region in the same circumferential direction as indicated by the data for +/- 10° of sideslip. The +10° sideslip case is much more similar to the 0 deg. sideslip than the -10° sideslip case in terms of overall contour levels. This comparison is due to the fuselage "shielding" the side wind from the leeward (-10°) inlet and thus allowing more low energy flow to enter the inlet than the windward side (+10°) inlet.

Alpha=50°, beta=±5°, mach=0.3

The NPARC contours are flanked by the flight test contours at their extreame azimuthal travel. The NPARC results are within the flight test range of travel, as shown in Figure 8e.

Alpha=60°, beta=±5°,0°, mach=0.3

For 60° alpha the amount of unsteadiness has increased significantly from the lower alpha cases as can be seen in Fig. 8f. For beta=0 deg, the low pressure region migrates between 180 and 300 deg circumferentially. For the nonzero sideslip cases, the angular migration is from 200 deg. to 300 deg. The NPARC results fall within this migration range. The comparison of the zero sideslip case with the +/-5 deg. sideslip cases are very similar. This is due to the large amount of distortion in the flow field not revealing many subtle differences that may exist between the two inlets in the nonzero sideslip case.

6.0 Related Studies

In this section, several studies related to specific issues concerning the HARV flow field calculations are presented.

6.1 Effect of Grid Refinement

In an effort to study the effects of grid density on inlet performance, the grid density of the inlet duct and lip was increased. It was not deemed feasible to increase the grid density of either the whole model or even the viscous blocks because of the large number of grid points and the time needed to obtain a solution.

The duct grid was increased by a factor of three in the axial and azimuthal directions. To keep the block size within dimensions that would give acceptable turnaround times on the Cray YMP, the duct was split into 3 blocks of 66x146x49 grids. The lip grid was doubled in all directions with dimensions of 65x75x65. The lip and duct grids now total near 1.7 million grid points.

The test case is the symmetrical grid model at an angle-of-attack of 30 deg. and Mach number of 0.3. Figure 9a and 9b shows the particle traces along the inlet lip and duct walls. The separation on the outboard edge of lip is better defined with two vortex cores lifting off the surface and migrating parallel to the flow as opposed to being parallel to the highlight as in the case with the coarser grid seen in Fig. 9c. This implies that the separation region is thicker. The cross-stream separation line, seen on the inboard lower corner (Fig. 9c), is weaker for the coarser grid results.

The flow patterns through the inlet are different from the lower density grid results. Contributions from the various lip and duct portions are more defined. Fig. 10a is a series of cross-sectional cuts along the duct. Station 1 is near the throat while station 6 is near the engine face. Cross-stream separations can be seen at both the upper and lower inboard corners and the outboard edge. The corner separations grow in size and migrate counter-clockwise towards the bottom of the inlet. The corner flows grow into finger-like or bubble projections into the main flow that give indications of shedding. Figure 10b shows the sources of the main regions of low total pressure.

As mentioned elsewhere in this report, the actual flow in the test aircraft inlet is unsteady. Figure 10c shows experimental total pressure contours for a sequence of times. The lighter shaded contours are regions of high total pressure recovery. The sequence of time is shown by the numbers

at the center of each plot. The total elapsed time between contour 1 and contour 2 is nearly 10 milliseconds. The growth of a "finger" of low total pressure region is seen near 8 to 9 o'clock in plot 4. In contour plot 5, the finger is fully formed and begins to dissappear in plot 6. This effect is very visible when the contours are "animated" in time.

The increase in calculated performance of the densely-gridded inlet was significant. The distortion decreased by 3 percentage points and the pressure recovery increased by one percentage point. Although the effect of grid density is very significant, due to limited computational resources, the coarser grids were used for the HARV calculations. The high density grid provides an important benchmark for the calculations.

6.2 Effects of Turbulence Models

A major consideration during the course of this study was the effect of the turbulence model chosen on the solution. In this section, a comparison of results obtained using three models: Baldwin-Lomax, Baldwin-Barth, and K-epsilon are discussed for a particular condition and scale. The scale is the proposed Lewis test model (19.78%) and the upstream wind tunnel conditions are 0.2 Mach number, 30 deg. angle-of-attack and 0 degrees sideslip. The decision to use the Baldwin-Barth turbulence model was based upon the results presented in this section.

The effects of the chosen turbulence model on the external flow are shown in Figure 11a-c. The Baldwin-Lomax turbulence model solution results in separation line along the fuselage under the LEX due to the under LEX vortex that is significantly lower than the separation line obtained from the Baldwin-Barth or K-epsilon models. Contours of turbulent viscosity, normalized by laminar viscosity are shown in Figure 11d-f. These were taken at a station midway along the LEX. The Baldwin-Lomax solution indicates almost a completely laminar flow field with the exception of the very near-wall region. The other two models indicate a large region of turbulence off the wall due to the under LEX and fuselage vortex. The viscosity distributions obtained with the Baldwin-Barth and k-epsilon turbulence models appear to be more consistent with the flow field physics than the contours obtained with the Baldwin-Lomax solution.

A comparison of the inlet flow fields, reveals another difference between the solutions obtained with the three turbulence models. Near the inlet entrance, a region of cross-stream separation present the Baldwin-Lomax solution is significantly diminished in the Baldwin-Barth solution and almost non-existent in the K- epsilon solution. These comparisons are shown in the vector plots in Figure 12a-c. Total pressure contours normalized by free-stream total pressure also indicate a similar trend in the low total pressure region associated with the cross-stream separation (Fig. 12d-f). For this region, the turbulent viscosity contours, shown in Figure 12g-i, do not show as marked a difference as those obtained along the fuselage. The significant difference is that the Baldwin-Barth and k-epsilon contours are much smoother and more evenly distributed than the contours associated with the Baldwin-Lomax model. It may be this smoother distribution has an influence on the development of the separation region.

A comparison of the total pressure contours at the engine face obtained for the three different

models are shown in Fig. 13a-c. All solutions are similar. The major item to note is that the secondary vortex shear layer increases in thickness from the Baldwin-Lomax to the Baldwin-Barth to the k-epsilon turbulence models. The turbulent viscosity contours are shown in Figure 13d- f. The Baldwin-Lomax results show a very erratic distribution of turbulent viscosity while the other two models show a very smooth distribution with the highest values of turbulent viscosity appearing in the core region of the secondary vortex which is due to the lift-off of the wall boundary layer. This behavior is more consistent with the flow field physics than the Baldwin- Lomax turbulent viscosity distributions.

Based upon these observations, the Baldwin-Barth and k-epsilon turbulence model were deemed to be more physically consistent with the flow physics than the Baldwin-Lomax model which was developed for two-dimensional flows. The Baldwin-Barth turbulence model was chosen due to being more computationally efficient and stable than the k-epsilon model.

6.3 Installation Effects

A short study was undertaken to investigate the effect of installation on the F/A-18A HARV inlet. The NPARC grid model was used with all blocks shut off except for the inlet where total conditions were similar to the installed entry without distortions present were used as upstream boundary conditions at grid station i=3. These conditions were used since this study was supporting planned but now-cancelled wind-tunnel tests of a 20% F/A=18A HARV model.

Figure 14 compares total pressure contours at stations near the throat and engine face of the plug flow with the installed inlet at 30 deg. angle-of-attack. The flow near the throat is very clean as expected with plug flow. No cross-flow separation is present at the engine face where there is very low distortion and high pressure recovery. The table below compares inlet performance.

installation	Prec	D2	Mcorr
plug flow	98.6%	9.7	144
installed	92.7%	24.1	143

6.4 Effect of Vortex Generators

Industry has a high interest in the use of vortex generators in eliminating or reducing flow separation inside ducts. A CFD code that could model and analyze various vortex generator geometries would be a useful tool. The HARV duct has a pair of vortex generators located at the bottom of the duct to prevent possible flow separation due to the bump of the wheel well.

The HARV vortex generator pair was modelled by adding five grid blocks to the HARV grid structure with minimal impact on computer memory requirements. Preliminary NPARC calculations Ref. [19] of the F/A-18A at an angle-of-attack of 3.8 degrees and Mach number of 0.8, show that the vortex generators have a significant local effect on the boundary layer at approximately the 6 o'clock location of the engine face which was also indicated in the experimental total pressure contours. Experimental results at these same aircraft conditions showed that the generators increased the overall total pressure recovery by only 0.33%.

A study was undertaken to investigate the effects of a pair of vortex generators located at the bottom wall of the inlet duct. The vortex generators were installed by manufacturer to mitigate the effect of the wheel well protrusions into the inlet wall. The vortex generators grids added five blocks to the F/A-18A model. The small size of the vortex generators can be seen in Fig. 15a which illustrates the placement of the vortex generators on the inlet's bottom grid surface; the chord of the vortex generators fall within the existing inlet duct grid points.

Because of the large disparity in grid density between the vortex generators and inlet grid, the transfer of flow variables between the vortex generator grid and inlet block interfaces would slow convergence considerably. To alleviate this problem, the grid density of a portion of the inlet grid surrounding the vortex generator was increased by an average factor of three in the circumferential direction and by a factor of eight in the axial direction as shown in Fig. 15b. This intermediate grid was extended downstream to the engine face to capture the vortex generators trailing tip vortices.

Test data taken during an earlier set of flight tests of the F/A- 18A [Ref. 28], compare the effect the vortex generators for a Mach number of 0.8 and angle-of-attack of 3.8 deg. Figure 16a compares total pressure contours between flight test and calculations. Total pressure contours compare well but, as seen earlier, the flow distortion is overestimated by NPARC and total pressure recovery is underestimated. The vortex generators have a significant thinning effect on the boundary layer

near the 6 o'clock location of the engine face. The effect on pressure recovery is small and there is insignificant effect on distortion. Figure 16b shows the trajectory of the particle traces off the vortex generators.

Calculations made at higher angles-of-attack and lower Mach numbers show that the vortex generators have no significant effect. No flight test data are available at higher angles-of-attack. Further details can be found in Ref. 19.

7.0 Conclusions and Recommendations

The results of this study indicate several important conclusions.

The first one is the need to include the external airframe in the calculations of the flow within the F/A-18A inlet due to the high degree of integration of the inlet with the airframe. Also, these results indicate the need for accurate modelling of geometric details. Earlier results indicated significantly different solutions due to the lack of sufficient details of the airframe geometry. The Baldwin-Barth turbulence model was found to provide the best results while being very stable and improved the convergence of the residuals three orders of magnitude as compared to the Baldwin-Lomax results. The NPARC results compared well with the forebody and lower LEX surface static pressures which indicates that the pertinent aspects of the external flow field were modelled well for the inlet flow field simulation. Although of little apparent effect on inlet performance, the collapse of the vortices over the LEX upper surface for nonzero sideslip cases, the use of NPARC for external flow calculations at high angles-of-attack where highly unsteady flows are present needs further study.

The effects of the inlet lip are also very important to the inlet flow field. The measured surface pressures along the lip were in good agreement, in general with the NPARC results. Possible flow separation shown in the data was not present in the numerical results along the lower region of the highlight. This may be done to the lack of an adequate transition model in the turbulence model. Therefore, more work may be needed in the area of turbulence modelling. All the present models have insufficient mixing resulting in higher distortion and lower pressure recoveries than experimental data. The effects of the presence of the engine appear to be small with regards to the surface circumferential pressure distribution at the engine face. The NPARC predictions agreed well with the flight data. It is unknown how significant the presence of the engine is on the migration of the secondary flow vortex or the unsteadiness of the flow field.

The effects of sideslip provide a perturbation to the zero sideslip results. The effects of the fuselage becomes more significant with a nonzero siedeslip present. Local flow along the inlet lip was also influenced by the presence of sideslip. The zero sideslip inlet performance was in between the performance of the leeward and windward inlets with nonzero sideslip. Although, the zero sideslip case performance was closer to the windward inlet performance than the leeward inlet.

This is consistent with less distorted flow from the fuselage entering the windward inlet than the leeward inlet, as is the case for the zero sideslip condition.

Although, the NPARC results represent an asymptotic solution, it was able to capture the essential physics associated with the inlet flow field which is inherently unsteady. Due to the limited amount of data obtainable from the flight tests, a scale model wind tunnel test program is strongly recommended. Steady state tests were planned in the Lewis 9x15 low Speed Wind Tunnel (LSWT). These tests were cancelled due to changing priorities and a resulting lack of funding to support the experiments. These tests were to use a 19.78 percent model of the F/A-18A HARV, which was completed, to investigate effects on inlet performance of the aircraft forebody and the effect of scale. The model was also to be used to investigate the effect of inlet pumping on inlet performance, using either a vacuum or simulator fans, and forebody with and without faired over inlets. Comparisons were to be made with flight results from the HARV. Furthermore, a data base was to be generated for CFD code calibration.

A few numerical studies should be undertaken with simple geometries. An isolated inlet with a lip should be modelled for high angles-of-attack and the results compared to existing test data. A cylinder in a free-stream at Reynolds numbers sufficient to shed a von Karman vortex street and a diffuser with large sidewall angles should be simulated with NPARC to study how a "steady state" solution models an inherently unsteady flow.

8.0 Acknowledgements

Support of this work by the Lewis Research Center of the National Aeronautics and Space Administration under contract NAS3-27186 is gratefully acknowledged. Interest shown by Project Manager, Thomas Biesiadny, is particularly appreciated. Thanks also to June Thompson of NASA Lewis for her contributions to setting up the data analysis system. In addition, the authors express their appreciation to Tammy Langhals and Maryann Johnston for their outstanding work, as usual, in producing the text and figures for this paper.

Others we wish to recognize since this paper represents the conclusion of this program are Bob Coltrin (retired Branch Chief) and Dick Burley (retired Program Manager) of Lewis. Thanks to Dr. Lonnie Reid and Dr. Joseph Nenni of NYMA for their technical reviews of program related papers and support over the years. The exceptional grid generation work provided by Jim Bruns (formerly of Sverdrup Technology, Inc.) is noted by the authors. We thank Ray Cosner of McDonnnell-Douglas Company for his assistance in supplying the F/A-18A airframe geometry database. Finally, we express our pleasure in working with all the High Alpha Technology Program team members at NASA Lewis, Langley, Ames, and Dryden Research Centers and at the General Electric Company.

9.0 References

1. Bowers, A.H., Regenie, V.A. and Flick, B.C., "F-18 High Alpha Research Vehicle: Lessons Learned," NASA CP-10143, Vol. 2, Presented at the 4th High Alpha Conference, July 12-14, 1994, NASA Dryden Flight Research Center.

2. Ghaffari, F., Bates, B.L., Luckring, J.M., Thomas, J.L., and Bierdron, R.T., "Navier-Stokes Solutions About the F/A-18 Wing-LEX-Fuselage Configuration with Multi-Block Structured Grids", AIAA Paper No. 91-3291, Presented at the 9th Applied Aerodynamics Conference, Baltimore, Maryland, September 23-25, 1991.

3. Gee, K., Tavella, D. and Schiff, L.B., "Computational Optimization of a Pneumatic Fuselage Forebody Flow Control Concept", AIAA Paper No. 91-3249. Presented at the 9th Applied Aerodynamics Conference, Baltimore, Maryland, September 23-25, 1991.

4. "A User's Guide to NPARC, Version 2.0", The NPARC Alliance, 1994. Arnold Engineering Development Center, Tullahoma, TN.

5. Baldwin, B.S. and Lomax, H., "Thin-Layer Approximation and Algebraic Turbulence Model for Separated Turbulent Flows", AIAA Paper No. 77-257., Jan. 1978.

6. Sirbaugh, J.R. and Reichart, B.A., "Computation of a Circular-to-Rectangular Transition Duct Flow Field" AIAA Paper No. 91-1741, Presented at the 22nd Fluid Dynamics, Plasma Dynamics and Lasers Conference, June 24-26, 1991, Honolulu, Hawaii.

7. Ahn, K.H., "Performance of Renormalized Group Algebraic Turbulence Model on Boundary Layer Transition Simulation", NASA CR 194466, NASA Lewis Research Center, February 1994.

8. Baldwin, B.S. and Barth, T.J., "A One-Equation Turbulence Transport Model for High Reynolds Number Wall-Bounded Flows", NASA TM 102847.

9. Georgiadis, N.J., Chistsomboon, T., and Zhu, J., "Modification of the Two Equation Turbulence Model in NPARC to a Chien Low Reynolds Number $\kappa - \epsilon$ Formulation", NASA TM 106710, NASA Lewis Research Center, September 1994.

10. Stokes, M.L. and Kneile, K.L., "A Search / Interpolation Algorithm for CFD Analysis", Presented at the World Congress on Computational Mechanics, University of Texas, Austin, Texas, September 1986.

11. Steinbrenner, J.P., Chawner, J.R., and Fouts, C.L., "The Gridgen 3-D Multiple Block Grid Generation System", WRDC-TR-90-30222, 1991.

12. Bruns, J.E. and Smith, C.F., "Full Navier-Stokes Calculations on the Installed F/A-18 Inlet at a High Angle-of- Attack," AIAA Paper No. 92-3175, Presented at the 28th Joint Propulsion Conference, Nashville, Tennessee, July 6-8, 1992.

13. Bruns, J.E. and Smith, C.F., "Installed F/A-18A Inlet Flow Calculations at a High Angle-of-Attack", Journal of Propulsion and Power, Vol. 10, No. 1, pp. 110-115, Jan.-Feb. 1994.

14. Smith, C.F., Podleski, S.D., and Barankiewicz, W.S., "Comparison of F/A-18A High Alpha Research Vehicle Inlet Flow Analysis Results with Flight Data: Part I (Without Sideslip)," AIAA Paper No. 95-2758, Presented at the 31st Joint Propulsion Conference, July 10-12, 1995, San Diego, California.

15. Podleski, S.D., Smith, C.F., and Barankiewicz, W.S., "Comparison of F/A-18A High Alpha Research Vehicle Inlet Flow Analysis with Flight Data: Part II," AIAA Paper No. 95-2756, Presented at the 31st Joint Propulsion Conference, San Diego, CA, July 10-12, 1995.

16. Podleski, S.D., "F/A-18 Inlet Calculations at 60° Angle-of-Attack and 10° Sideslip," Journal of Propulsion and Power, Vol. 10, No. 6, Nov-Dec 1994, pp. 848-854.

17. Smith, C.F., "Prediction of Wind Tunnel Effects on the Installed F/A-18A Inlet Flow Field at High Angles-of-Attack," NASA CR 195429, January 1995.

18. Smith, C.F. and Podleski, S.D., "Installed F/A-18A Inlet Flow Calculations: A Grid Study", Journal of Propulsion and Power, in press, 1995.

19. Podleski, S.D., "PARC3D Calculations of the F/A-18 Inlet Vortex Generators", NASA Contractor Report, 195456, September 1995.

20. Podleski, S.D., "Installed F/A-18 Inlet Flow Calculations at 60° Angle-of-Attack and 10° Sideslip," AIAA Paper No. 93-1806, Presented at the 29th Joint Propulsion Conference, Monterey, California, June 28-30, 1993.

21. Smith, C.F. and Podleski, S.D., "Installed F/A-18 Inlet flow Calculations at 30° Angle-of-Attack: A Comparative Study," NASA CR 195297, April 1994.

22. Smith, C.F. and Podleski, S.D., "Installed F/A-18 Inlet Flow Calculations at 30°; Angle-of-Attack: A Comparative Study," AIAA Paper No. 94-3213, Presented at the 30th Joint Propulsion Conference, Indianapolis, IN, June 27-29, 1994.

23. Podleski, S.D., "Installed F/A-18 Inlet Flow Calculations at High Angles-of-Attack and Moderate Sidelip," NASA CP-101, Vol. 2, 4th NASA High Alpha Conference, NASA Dryden Flight Research Center, July 12-14, 1994.

24. Walatka, P.P., Plessel, T., McCabe, R.K., Clucas, J. and Elson, P.A., "FAST User's Manual", NASA Ames Research Center: WAO and RND, Beta 2.0, RND-91-011, Dec. 1991.

25. Fisher, D.F., Banks, D.W., Richwine, D.M., "F-18 High Alpha Research Vehicle Surface Pressures: Initial In-Flight Results and Correlation with Flow Visualization and Wind Tunnel Data", NASA TM 101724. 1990.

26. "Inlet Distortion for Stabilized Maneuvers on an F/A-18A Aircraft at High Angles-of-Attack," NASA TM, 1996. In writing.

27. Walatka, P.P., Buining, P.G., Pierce, L., and Elson, P.A., "PLOT3D User's Guide", NASA TM 101067, March 1990.

28. Amin, N.F., Richards, C.J., de la Vega, E.G., and Dhanidan, M.A., "F/A-18A Engine Inlet Survey Report, Vols. 1,2 and 3," NOR 81-316, Northrup Corp., Aircraft Division, Hawthorne, CA, Nov. 1981.

Block	I x J x K	Grid Type	
1	49 x 41 x 65	O–H	forebody
2	90 x 33 x 18	O–H	canopy and upper surface of fuselage and LEX
3	82 x 49 x 50	O–H	lower surface of fuselage and LEX
4	42 x 49 x 41	O–H	free stream wrap of blocks 2 and 3
5	34 x 50 x 33	H–H	side diverter
6	35 x 25 x 42	O–H	belly next to cowl
7	26 x 58 x 58	O–H	ramp/splitter plate and lower surface of LEX
8	66 x 50 x 49	O–H	inlet
9	34 x 26 x 41	H–H	upper diverter and lower surface of LEX
10	27 x 34 x 34	O–H	front portion of cowl
11	9 x 41 x 34	O–H	mid portion of cowl
12	27 x 25 x 18	O–H	rear portion of cowl and lower fuselage
13	27 x 33 x 18	O–H	upper fuselage and LEX to the rear of the canopy
14	18 x 25 x 18	O–H	upper fuselage and LEX to the rear of block 13
15	34 x 57 x 41	O–H	free stream wrap to the rear of block 4
16	43 x 49 x 26	O–H	lower surface of wing
17	43 x 33 x 26	O–H	upper surface of wing
18	11 x 41 x 9	O–H	free stream wrap of wing block
19	9 x 41 x 33	O–H	rearmost fuselage block
20	41 x 27 x 33	H–H	side diverter slot through LEX
21	33 x 37 x 33	C–H	inlet lip
22	41 x 21 x 26	C–H	leading–edge flap

Table 1: F/A–18A Grid Block Description

Mach	α	β	Prec	D2	$\dot{m}$	Source
0.30	3.0	0	95.8	15.7	144.5	NPARC
0.30	3.0	0	96–98	9–15	146	Test
0.40	3.0	0	97.4	12.5	142.9	NPARC
0.40	3.0	0	97–98	9–14	145.8	Test
0.30	30.0	10.0	95	19	143	NPARC
0.31	28.5	10.5	96–98	9–14	146	Test
0.30	30.0	–10.0	92	23	145	NPARC
0.32	30.5	–9.0	95–97	10–17	146	Test
0.30	3.0	0	95.1	19	143	NPARC
0.30	3.0	0	97–98	9–13	145.8	Test
0.40	30.0	10.0	96	18	144	NPARC
0.42	27.3	7.5	97–98	8–12	146	Test
0.40	30.0	–10.0	93	23	144	NPARC
0.40	31.5	–7.0	94–96	10–20	146	Test
0.40	30.0	0	95.9	16.9	143.8	NPARC
0.40	30.0	0	97–98	8–14	145.9	Test
0.30	50.0	5.0	92	24	145	NPARC
0.29	48.5	5.0	94–96	11–19	146	Test
0.30	50.0	–5.0	92	28	145	NPARC
0.30	49.5	–5.0	92–94	13–26	146	Test
0.30	60.0	5.0	90	29	144	NPARC
0.31	59.0	4.0	90–92	16–33	146	Test
0.30	60.0	–5.0	88	35	144	NPARC
0.32	59.0	–2.5	88–91	15–34	146	Test
0.30	60.0	0	88.5	31.5	143.7	NPARC
0.30	60.0	0	90–92	14–28	145.9	Test

Table 2: F/A–18A Inlet Performance Summary

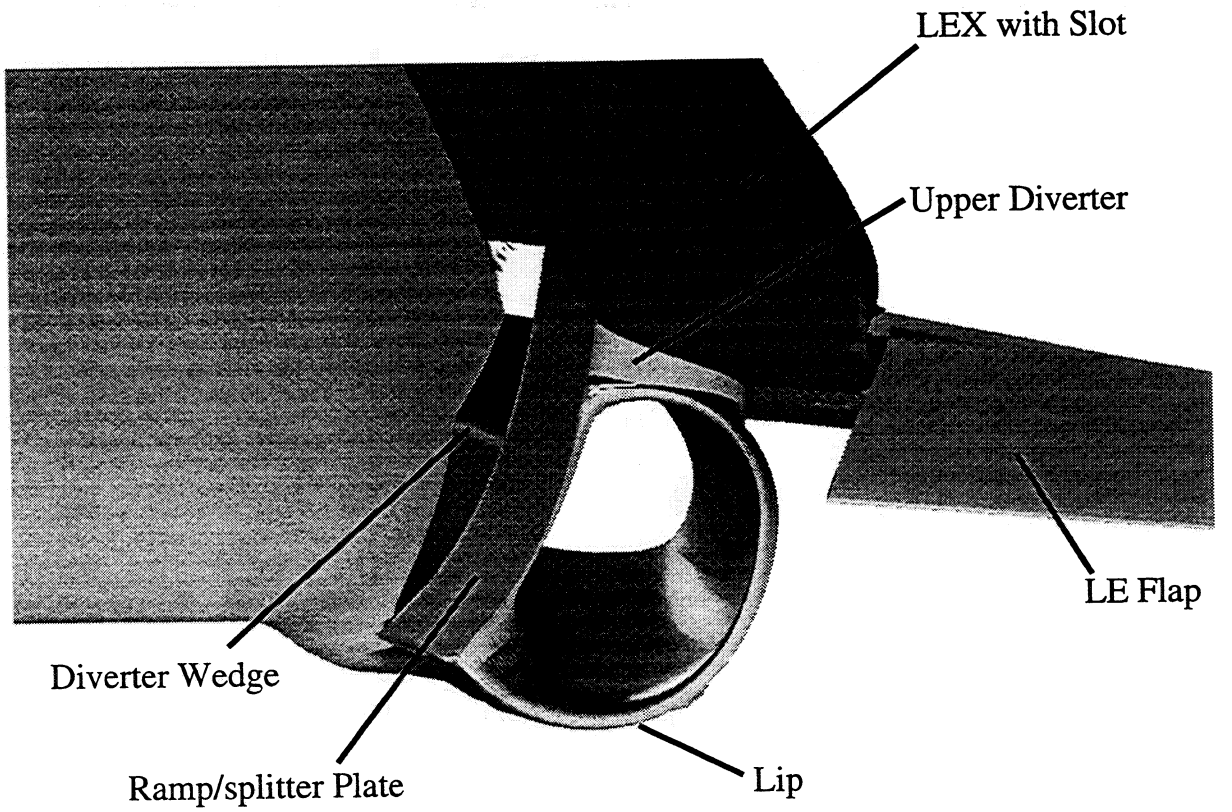

(a) – F/A–18A Geometry

Fig. 1: F/A–18A Computational Model

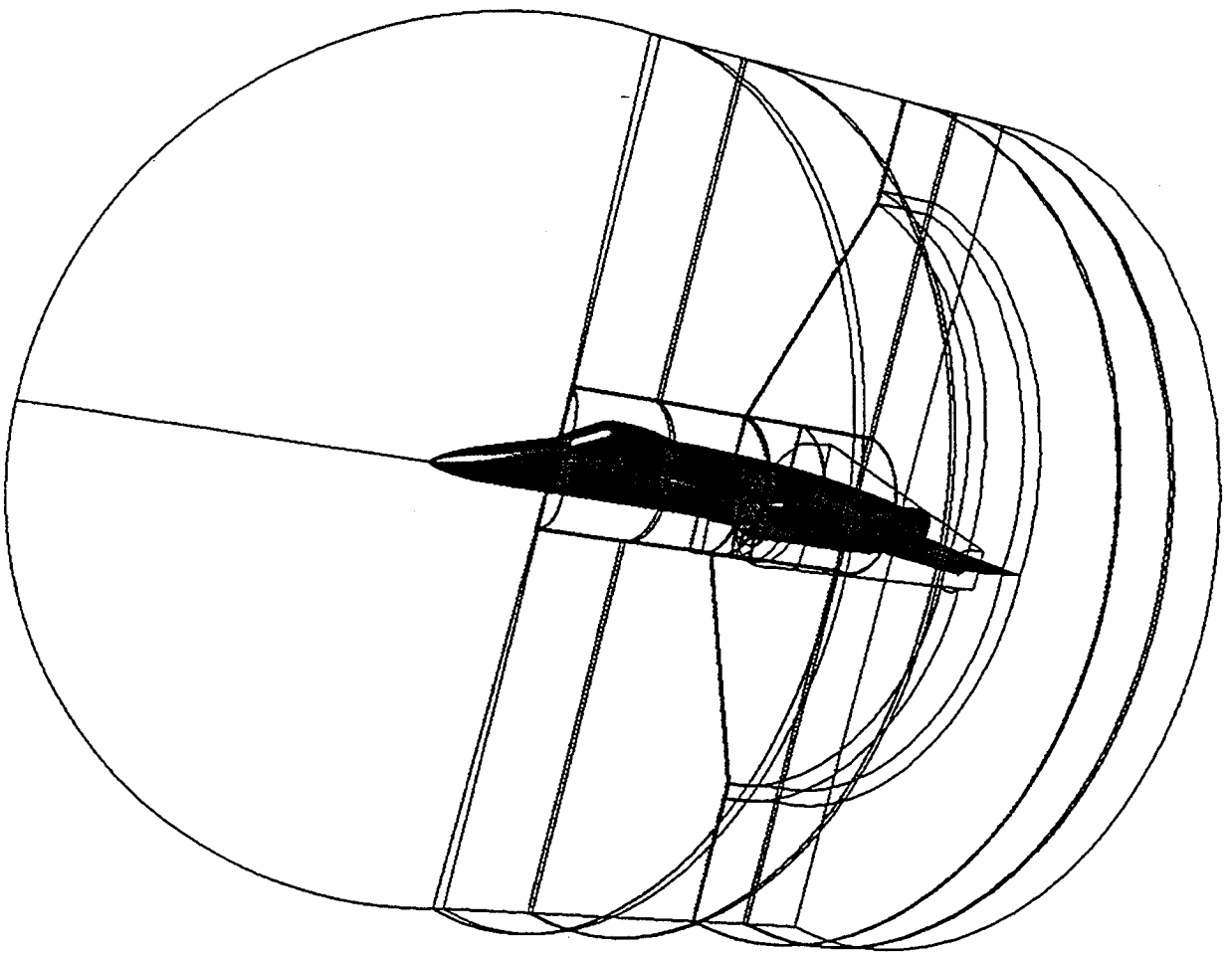

(b) – F/A–18A Grid Block Structure

Fig. 1: F/A–18A Computational Model

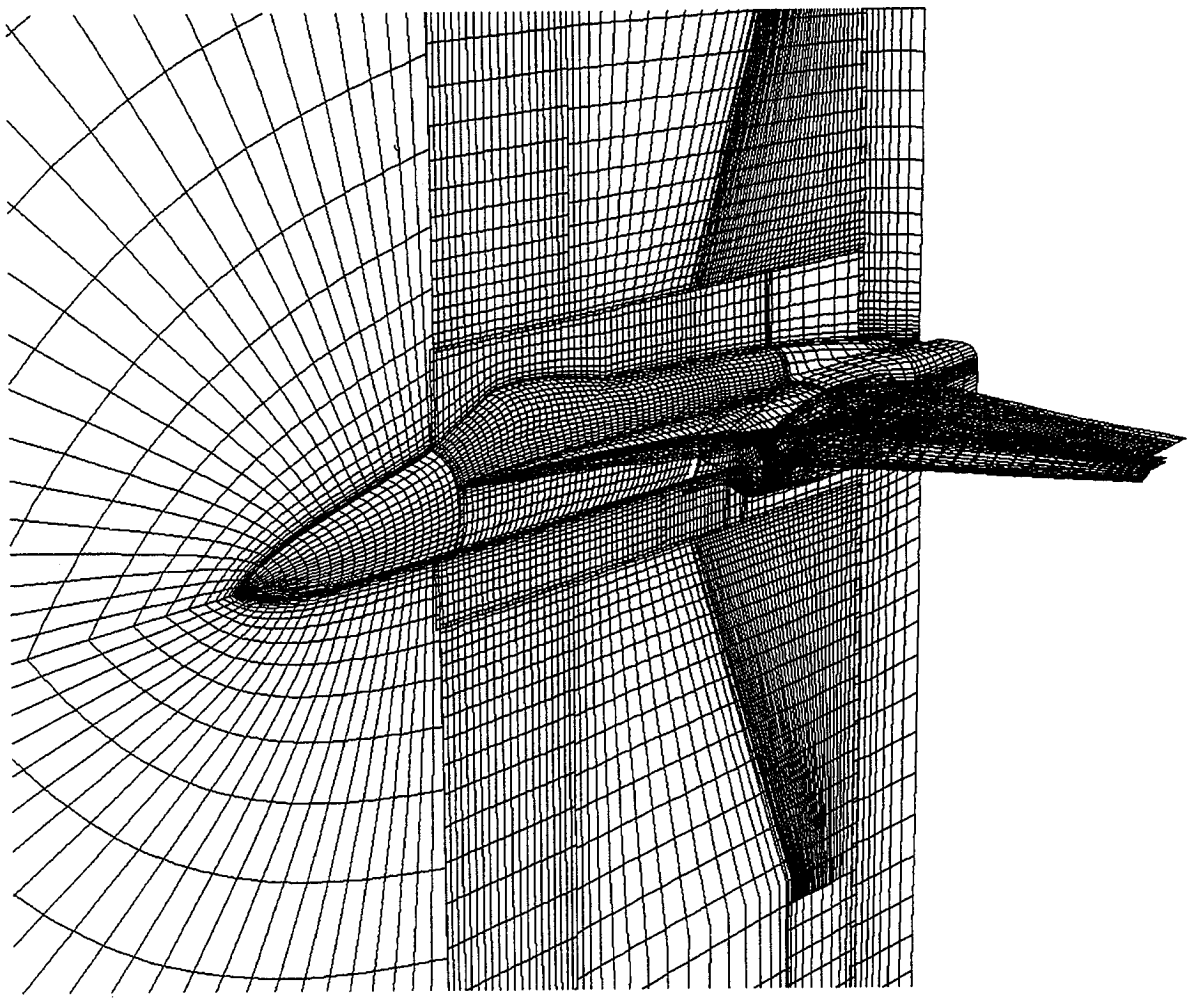

(c) – F/A – 18A Surface and Plane of Symmetry Grid

Fig. 1: F/A–18A Computational Model

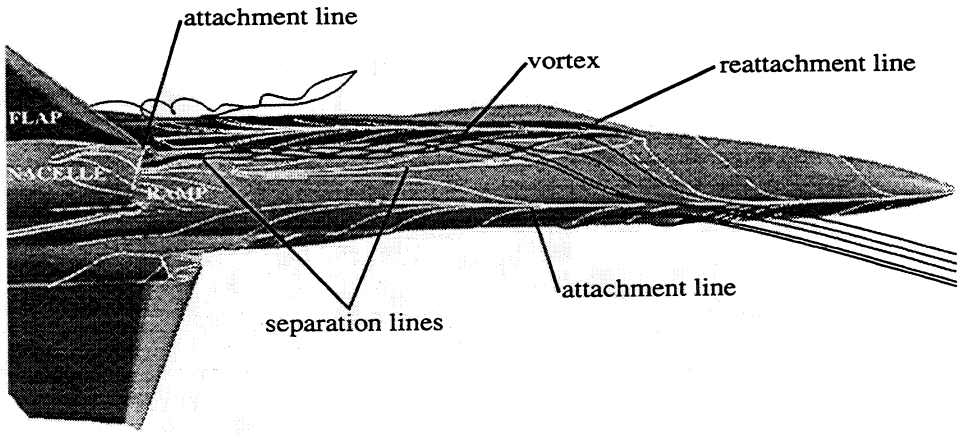

Particle traces along windward side for $\alpha = 30°$, $\beta = +10°$, $M_\infty = 0.3$

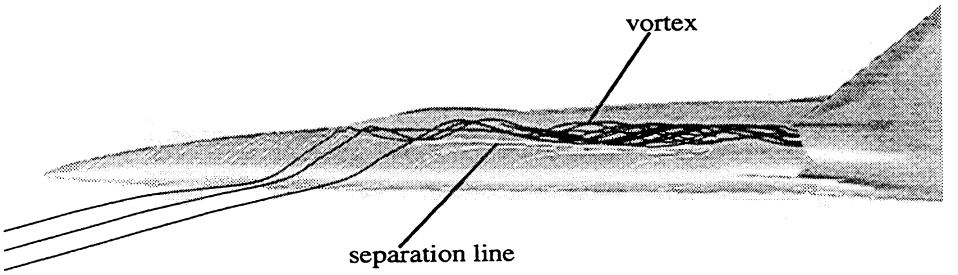

Particle traces along leeward side for $\alpha = 30°$, $\beta = 0°$, $M_\infty = 0.3$

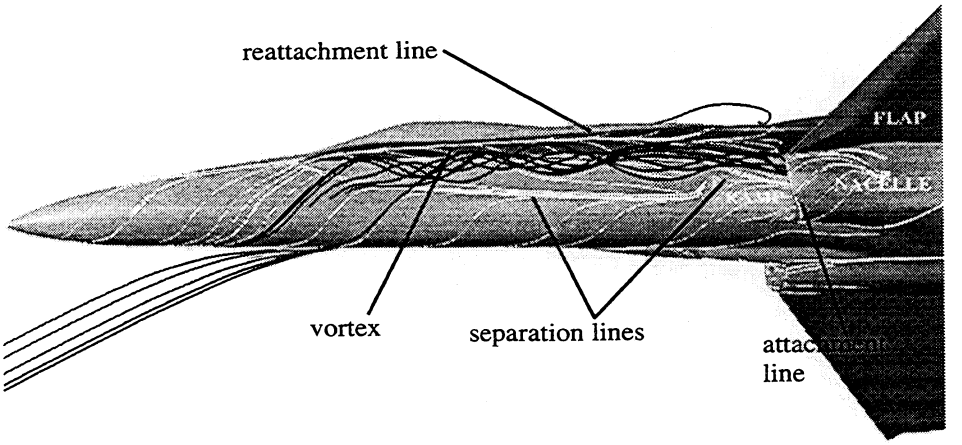

Particle traces along leeward side for $\alpha = 30°$, $\beta = -10°$, $M_\infty = 0.3$

(a) $\alpha = 30°$, $\beta = \pm 10°, 0°$, $M_\infty = 0.3$

Fig. 2: External Flow Particle Trajectories

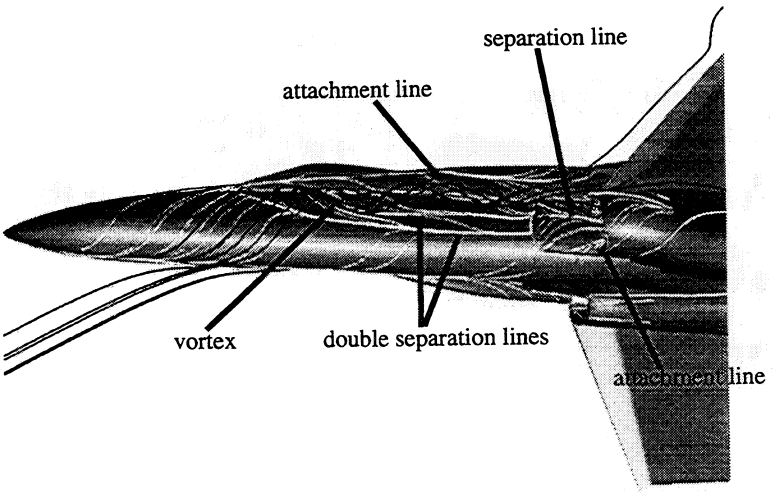

$\alpha = 30°, \beta = -10°, M_\infty = 0.4$

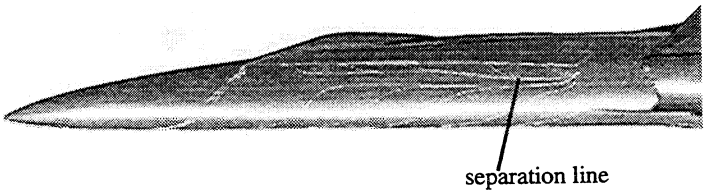

$\alpha = 30°, \beta = 0°, M_\infty = 0.4$

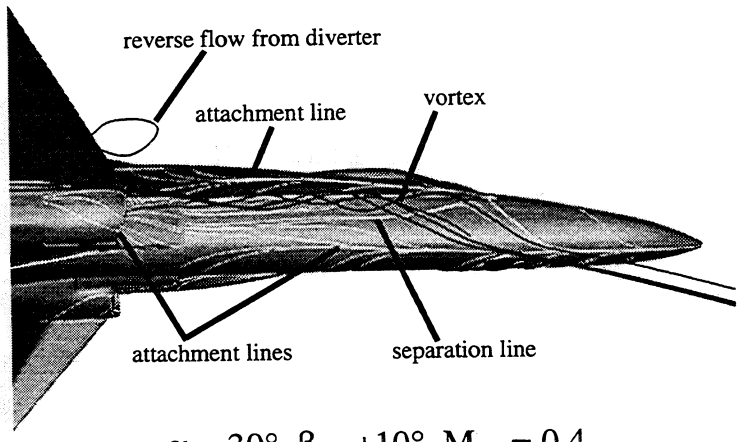

$\alpha = 30°, \beta = +10°, M_\infty = 0.4$

(b) $\alpha = 30°, \beta = \pm 10°, 0°\ M_\infty = 0.4$

Fig. 2: External Flow Particle Trajectories

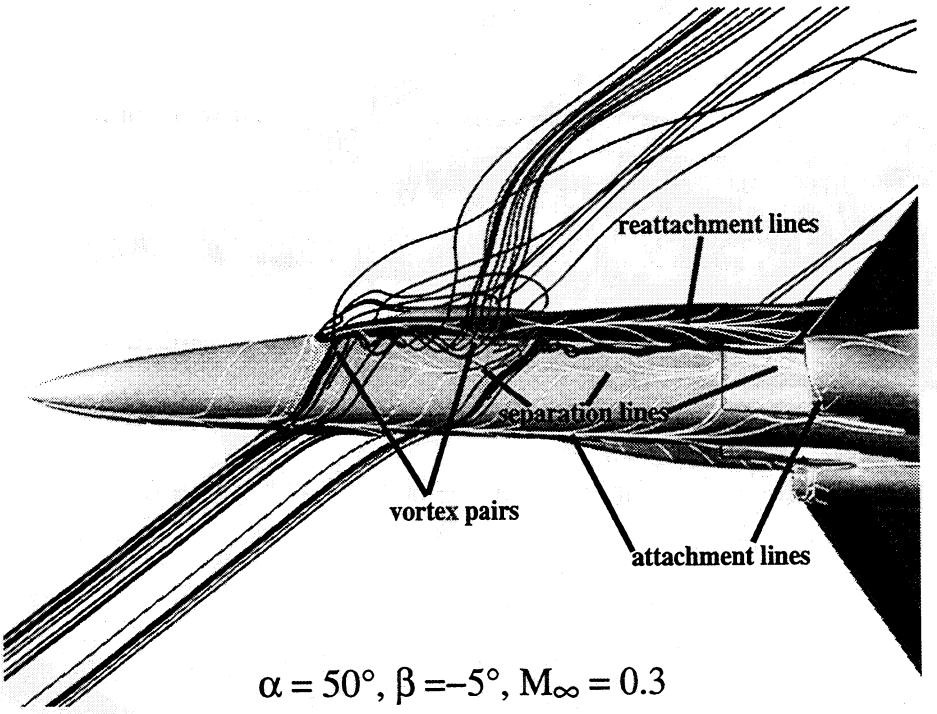

$\alpha = 50°, \beta = -5°, M_\infty = 0.3$

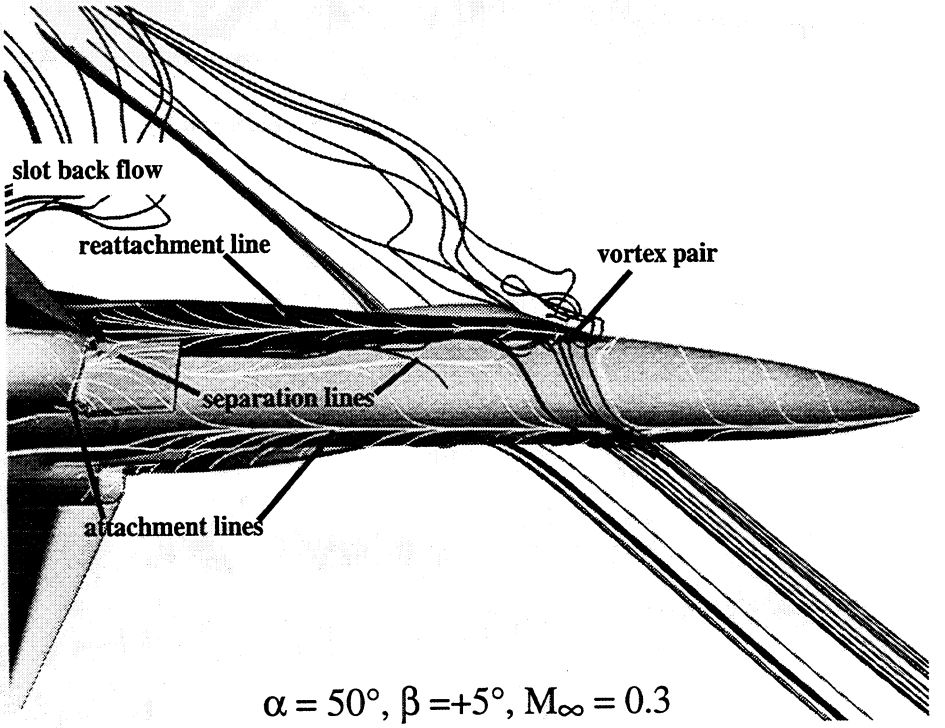

$\alpha = 50°, \beta = +5°, M_\infty = 0.3$

(c) $\alpha = 50°, \beta = \pm 5°, M_\infty = 0.3$

Fig. 2: External Flow Particle Trajectories

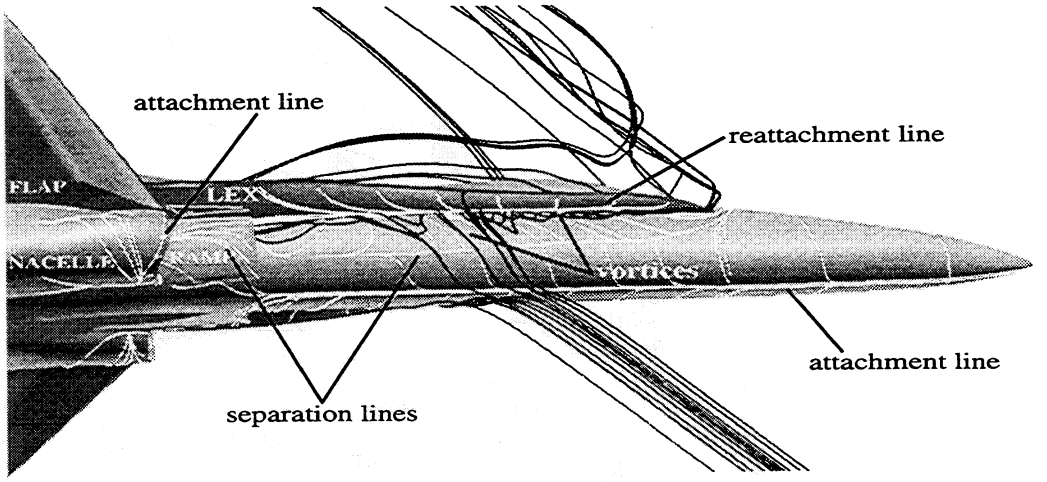

Particle traces along windward side for $\alpha = 60°$, $\beta = +5°$, $M_\infty = 0.3$

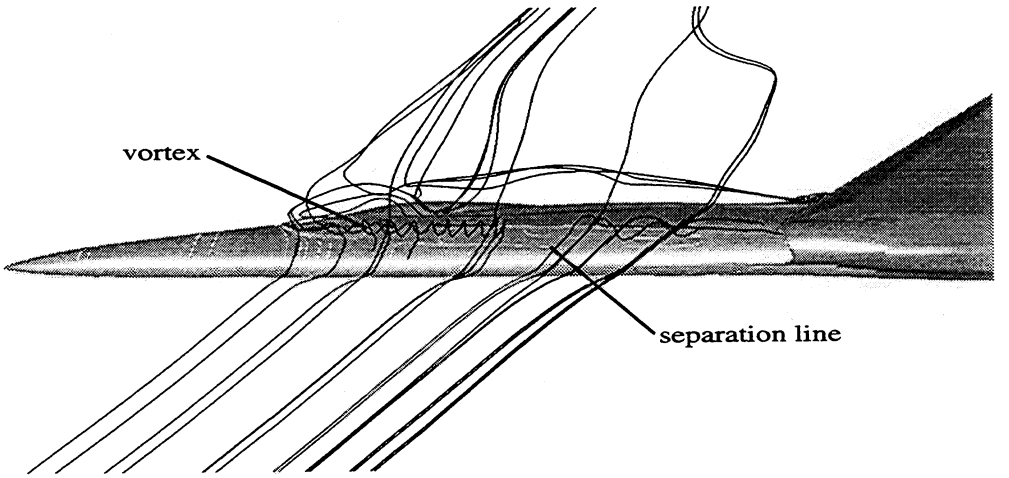

Particle traces along leeward side for $\alpha = 60°$, $\beta = 0°$, $M_\infty = 0.3$

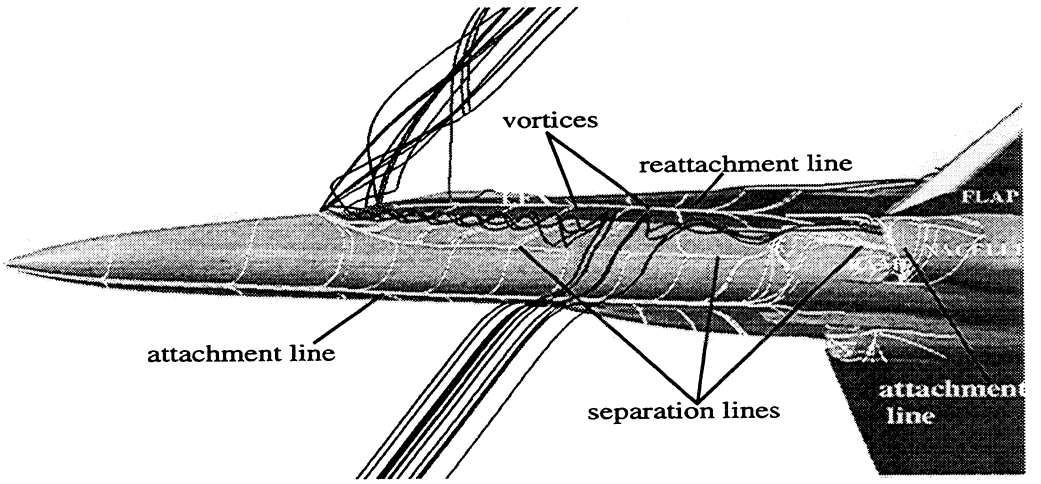

Particle traces along leeward side for $\alpha = 60°$, $\beta = -5°$, $M_\infty = 0.3$

(d) $\alpha = 60°$, $\beta = \pm 5°$, $0°$, $M_\infty = 0.3$

Fig. 2: External Flow Particle Trajectories

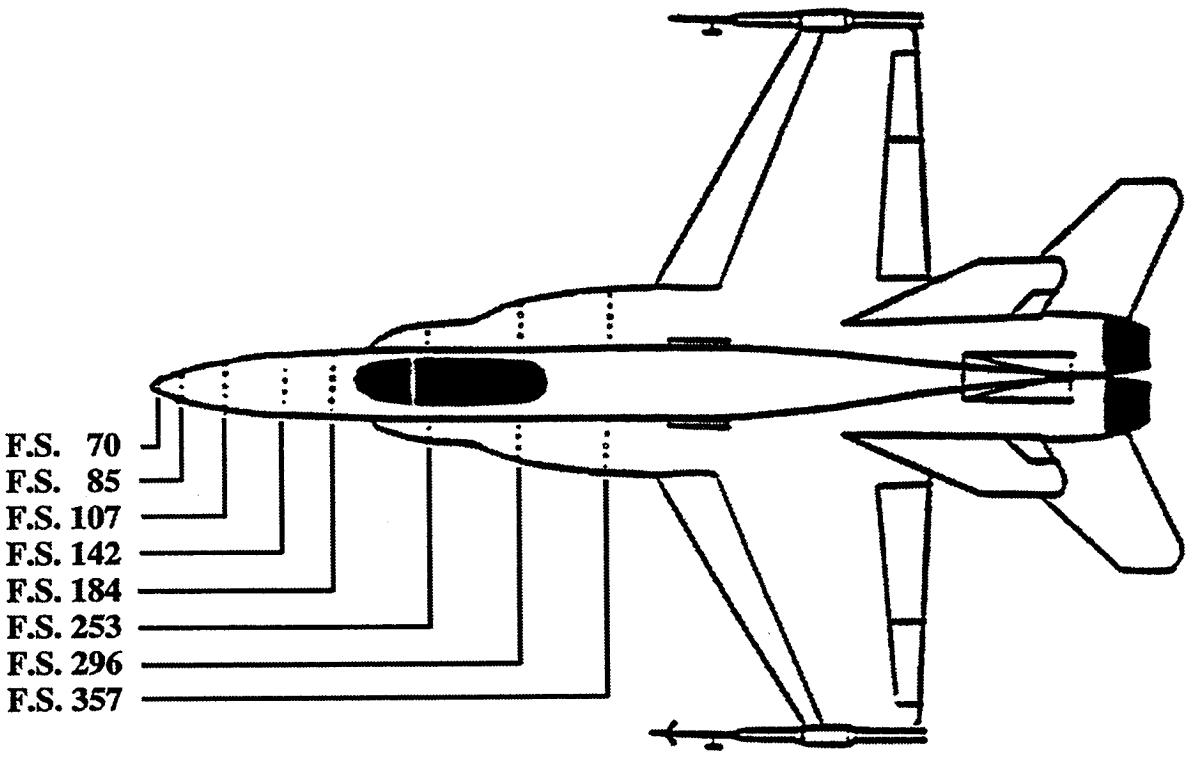

Fig. 3a: Forebody/LEX Surface Pressure Measurement Stations

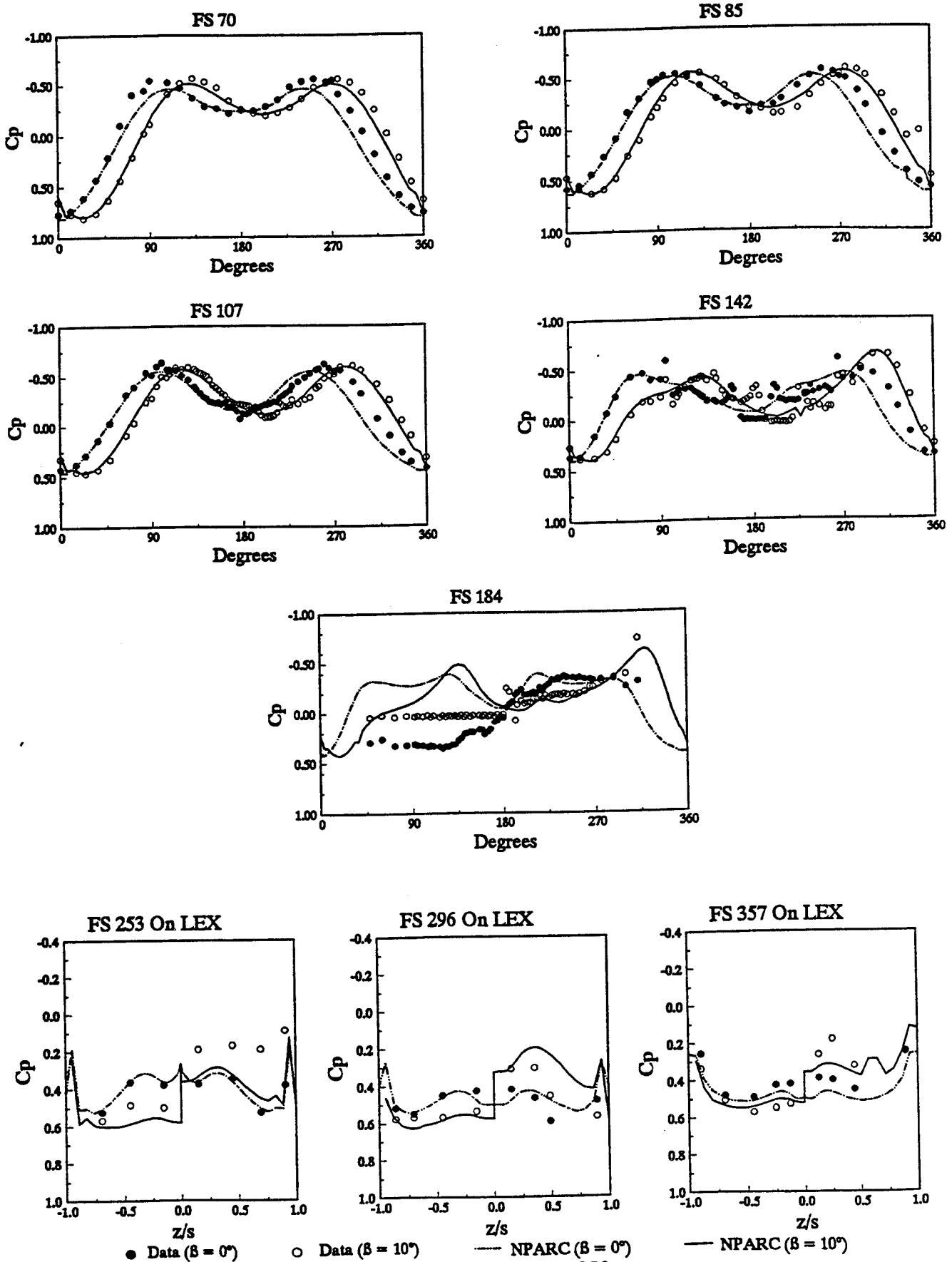

(b). $M\infty = 0.3, \alpha = 30°$

Fig. 3 - Forebody/Lower LEX Surface Static Pressure Distributions

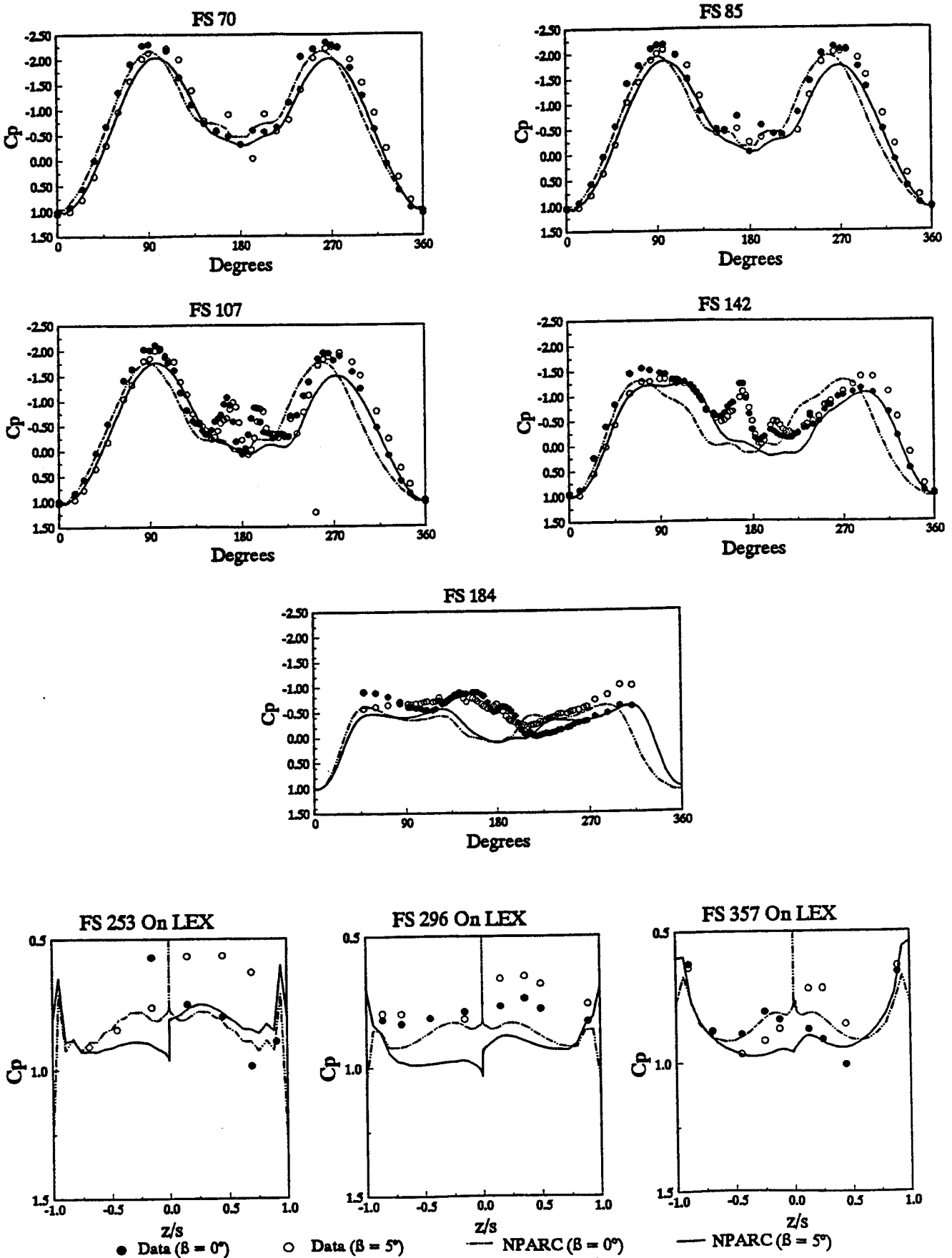

(c). $M\infty = 0.3, \alpha = 60°$

Fig. 3 - Forebody/Lower LEX Surface Static Pressure Distributions

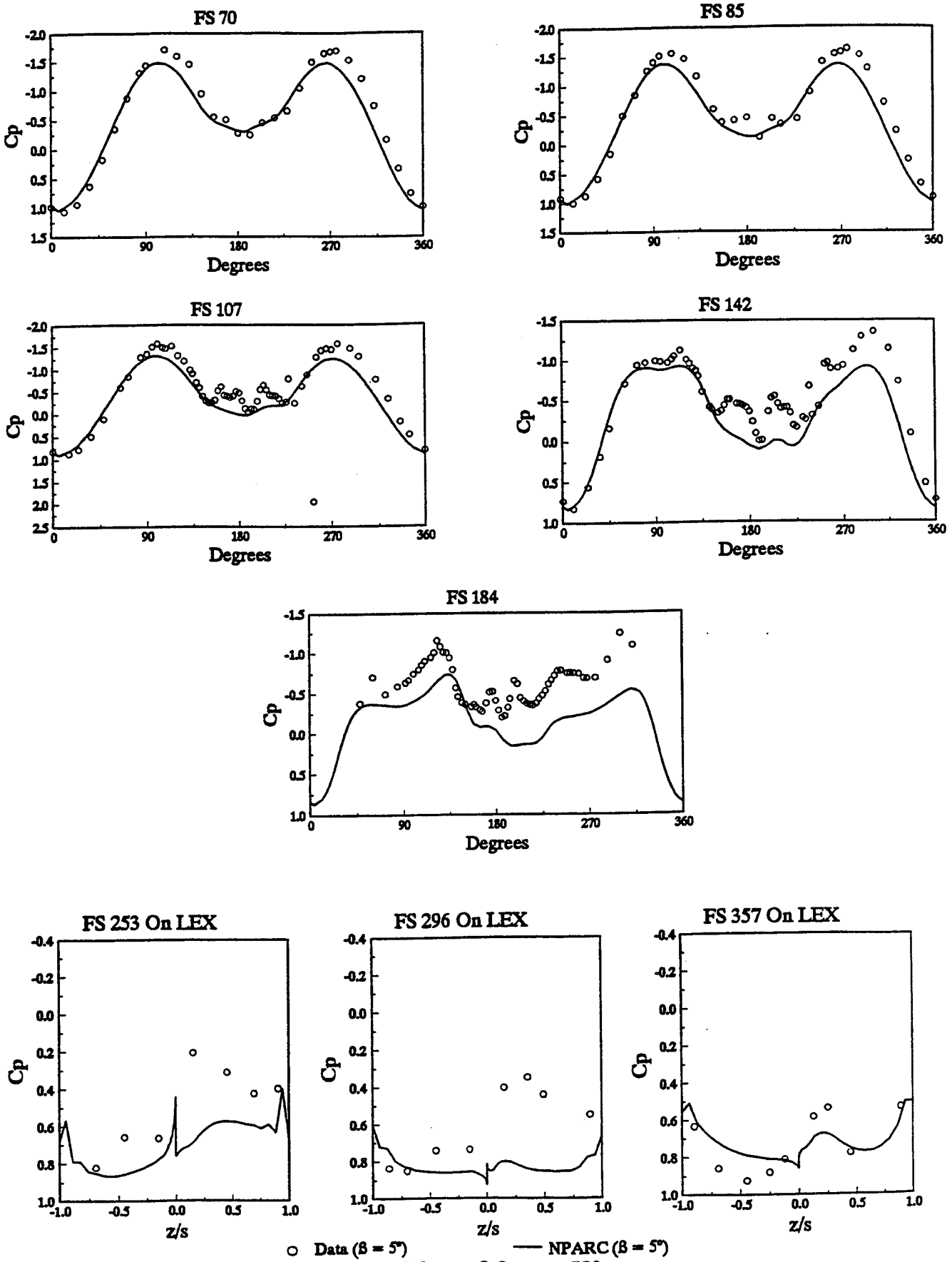

(d). $M\infty = 0.3, \alpha = 50°$

Fig. 3 - Forebody/Lower LEX Surface Static Pressure Distributions

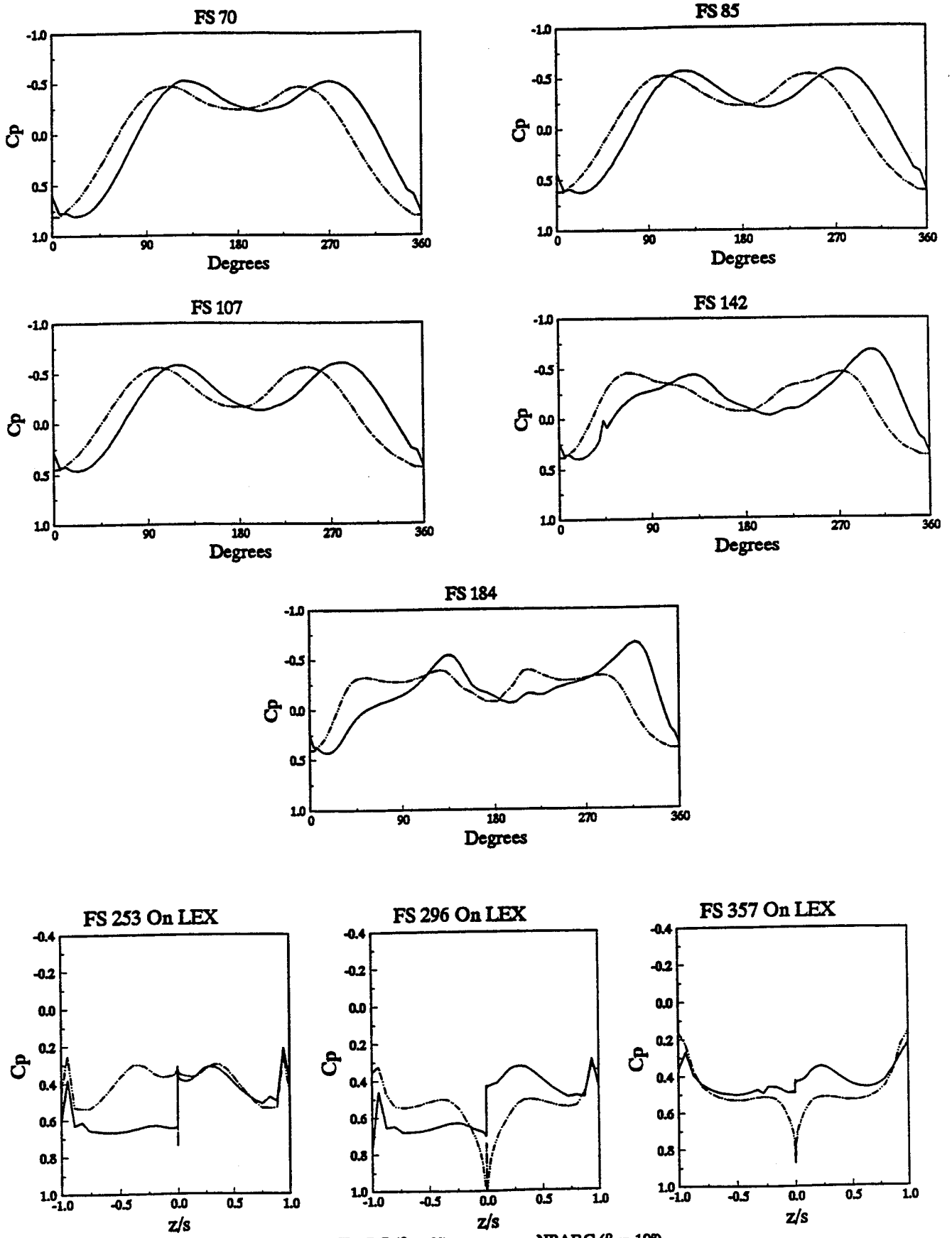

(e). $M\infty = 0.4, \alpha = 30°$

Fig. 3 - Forebody/Lower LEX Surface Static Pressure Distributions

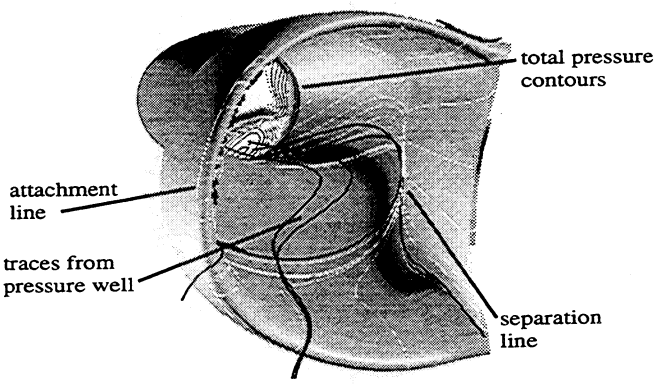

Particle traces for windward inlet at $\alpha = 30°$, $\beta = +10°$, $M_\infty = 0.3$

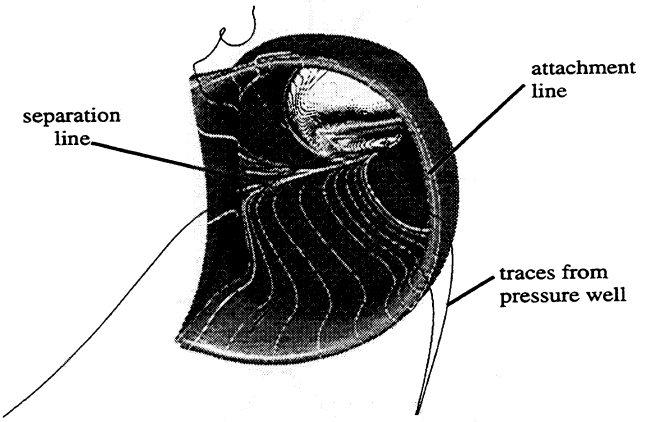

Particle traces for windward inlet at $\alpha = 30°$, $\beta = 0°$, $M_\infty = 0.3$

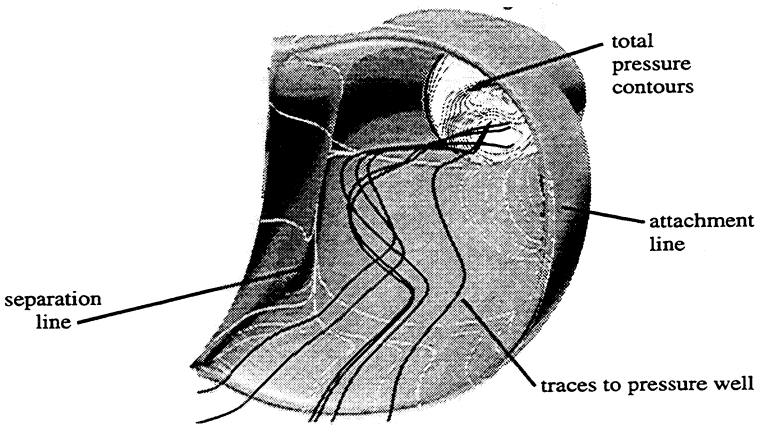

Particle traces for leeward inlet at $\alpha = 30°$, $\beta = -10°$, $M_\infty = 0.3$

(a) Front View ($\alpha = 30°$, $\beta = \pm 10°, 0°$, $M_\infty = 0.3$)

Fig. 4: Inlet Flow Particle Trajectories

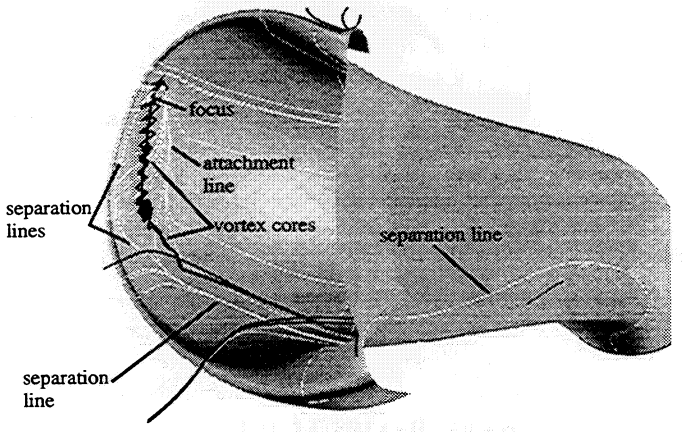

Particle traces for windward inlet at $\alpha = 30°$, $\beta = +10°$, $M_\infty = 0.3$

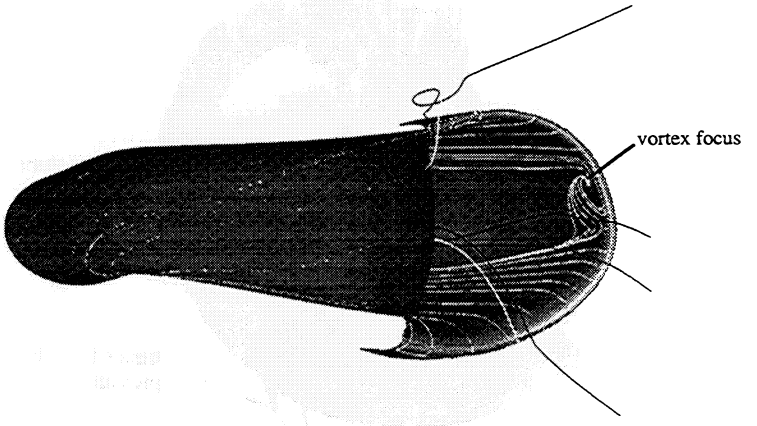

Particle traces for leeward inlet at $\alpha = 30°$, $\beta = 0°$, $M_\infty = 0.3$

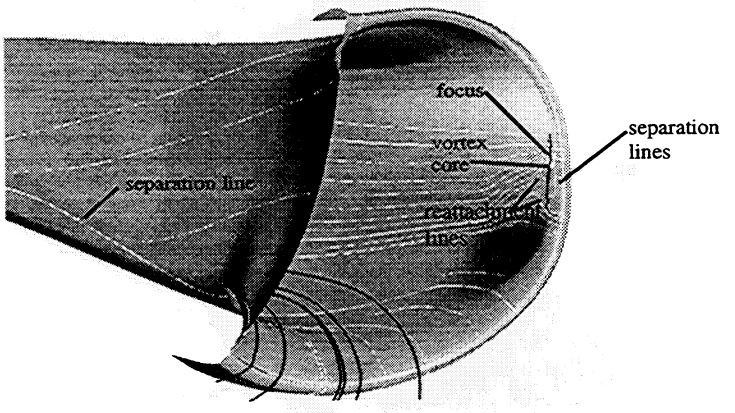

Particle traces for leeward inlet at $\alpha = 30°$, $\beta = -10°$, $M_\infty = 0.3$

(b) Side View ($\alpha = 30°$, $\beta = \pm 10°, 0°$, $M_\infty = 0.3$)

Fig. 4: Inlet Flow Particle Trajectories

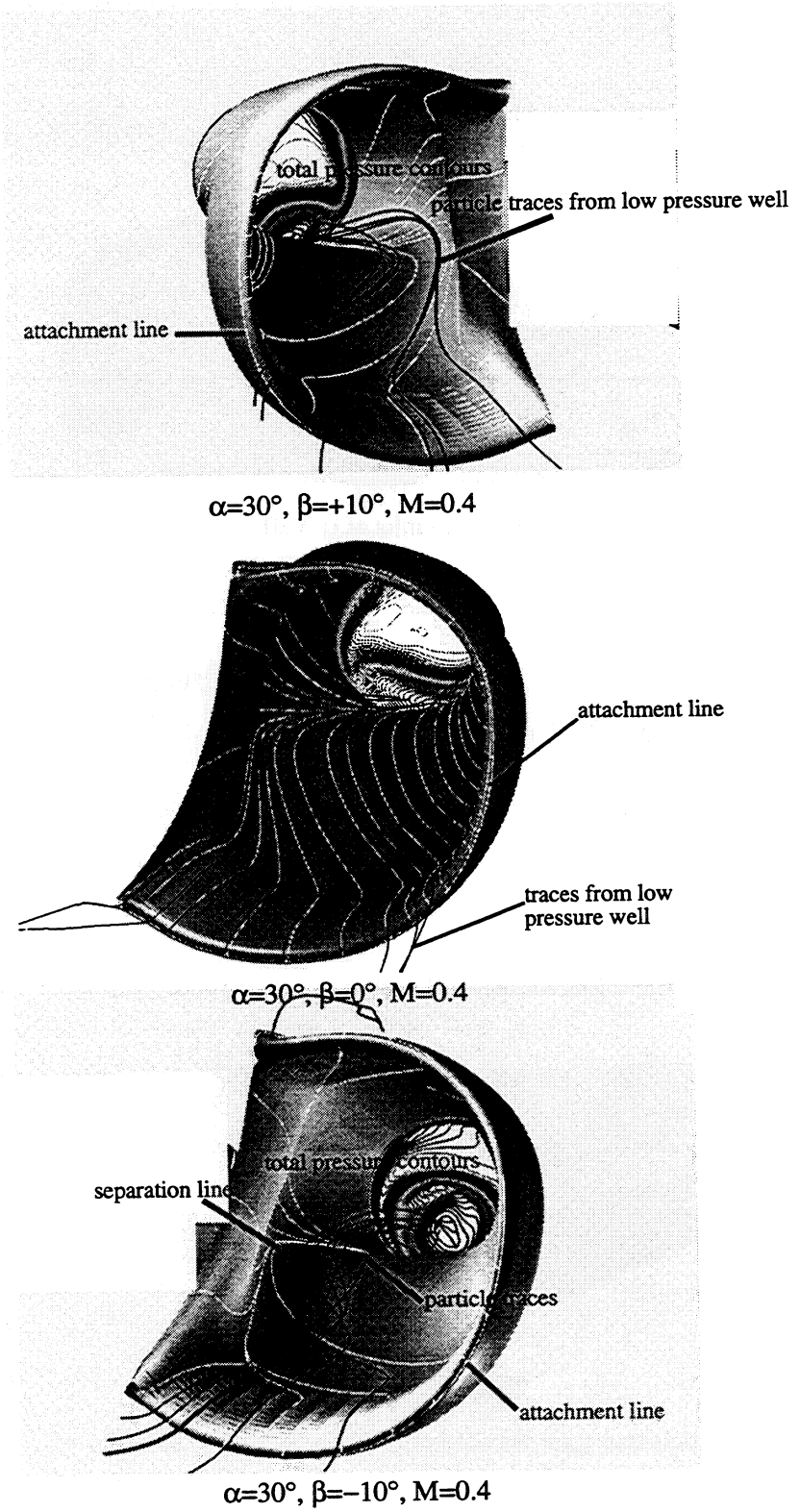

(c) Front View ($\alpha = 30°$, $\beta = \pm 10°, 0°$, $M_\infty = 0.4$)

Fig. 4: Inlet Flow Particle Trajectories

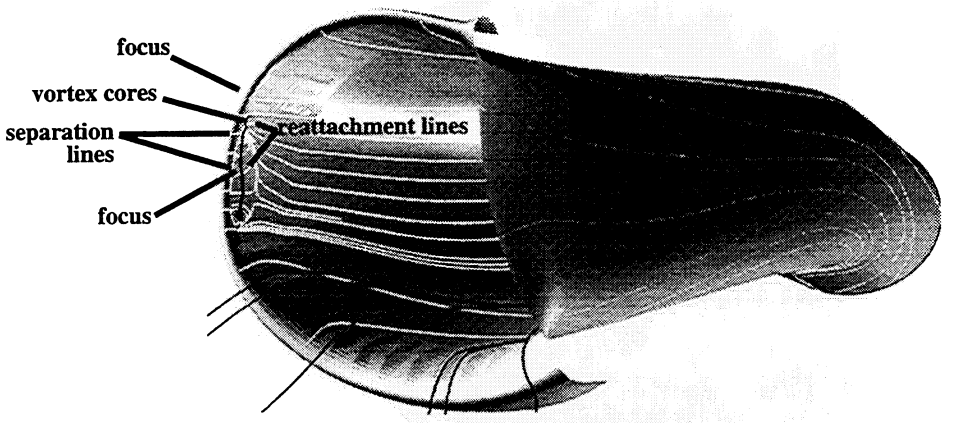

$\alpha = 30°, \beta = +10°, M_\infty = 0.4$)

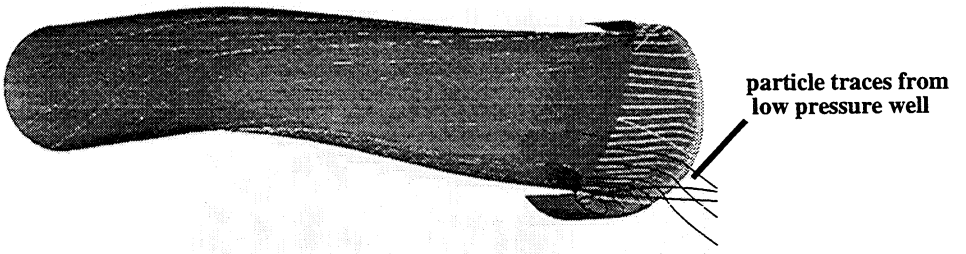

$\alpha = 30°, \beta = 0°, M_\infty = 0.4$)

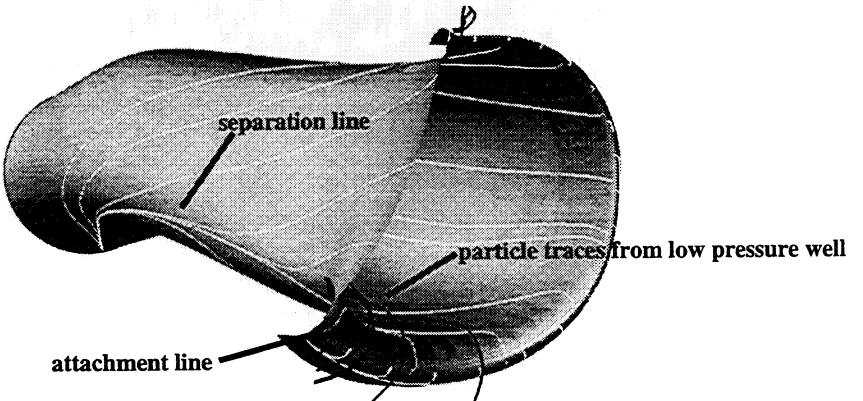

$\alpha = 30°, \beta = -10°, M_\infty = 0.4$)

(d) Side View ($\alpha = 30°, \beta = \pm 10°, 0°, M_\infty = 0.4$)

Fig. 4: Inlet Flow Particle Trajectories

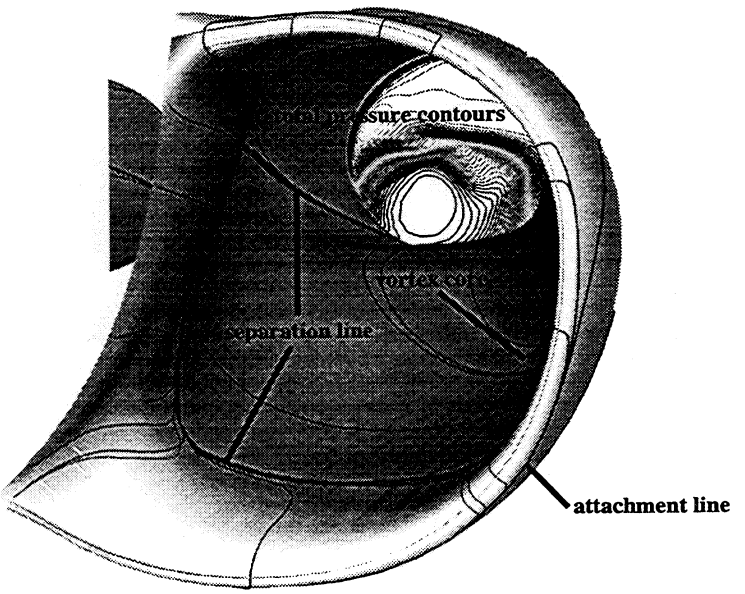

$\alpha = 50°, \beta = +5°, M_\infty = 0.3$

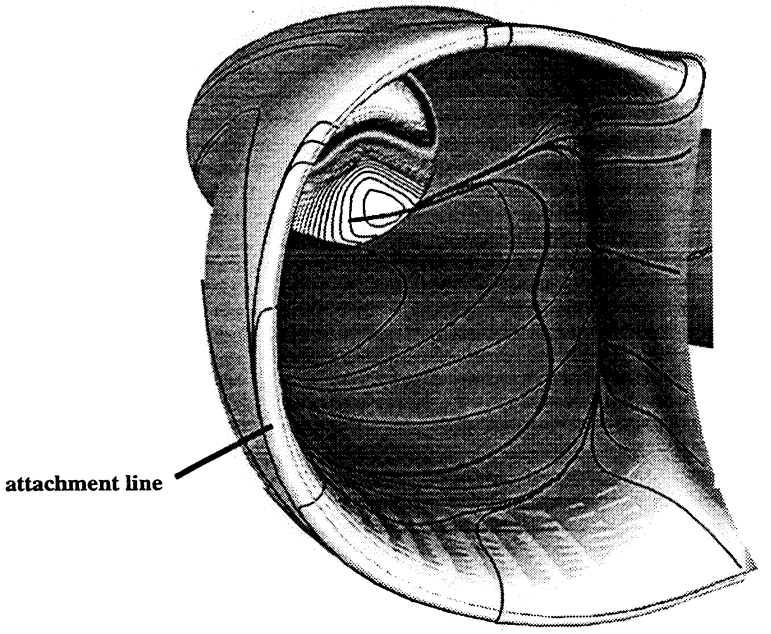

$\alpha = 50°, \beta = -5°, M_\infty = 0.3$

(e) Front View ($\alpha = 50°, \beta = \pm 5°, M_\infty = 0.3$)

Fig. 4: Inlet Flow Particle Trajectories

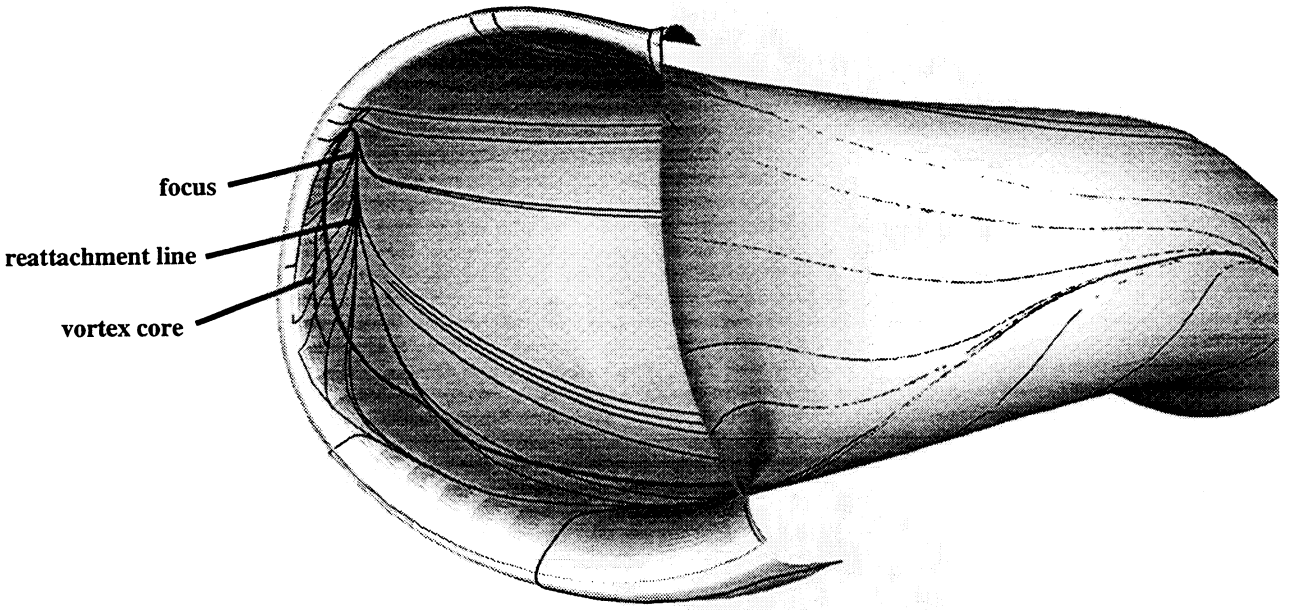

α=50°, β=+5°, M_∞=0.3)

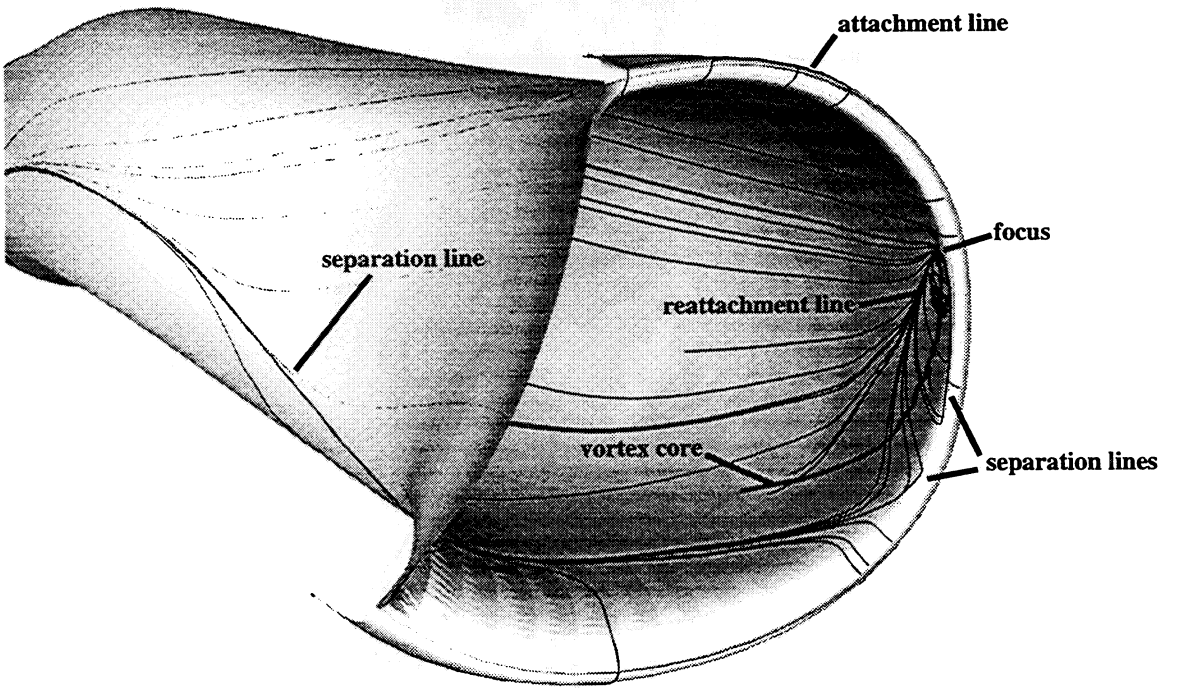

α=50°, β=–5°, M_∞=0.3)

(f) Side View (α=50°, β=±5°, M_∞=0.3)

Fig. 4: Inlet Flow Particle Trajectories

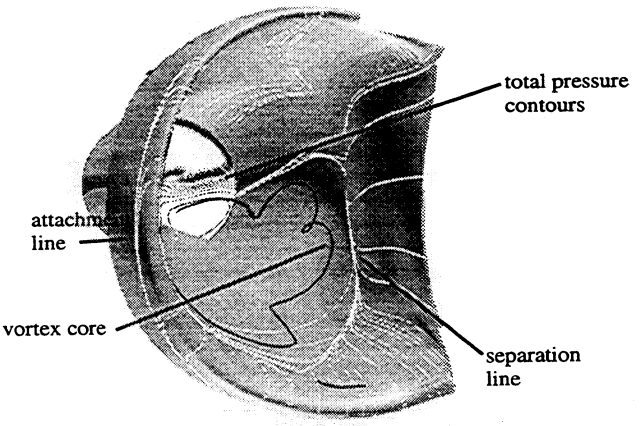

Particle traces for windward inlet at $\alpha = 60°$, $\beta = +5°$, $M_\infty = 0.3$

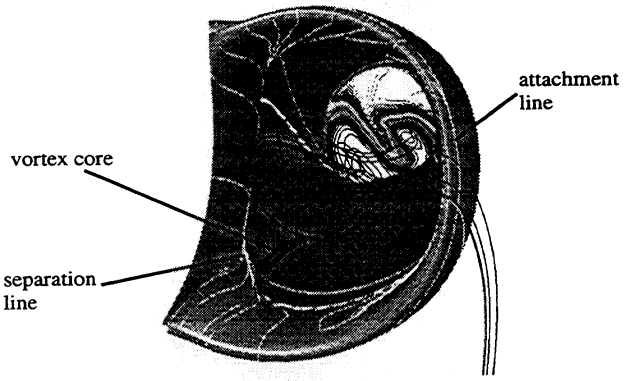

Particle traces for leeward inlet at $\alpha = 60°$, $\beta = 0°$, $M_\infty = 0.3$

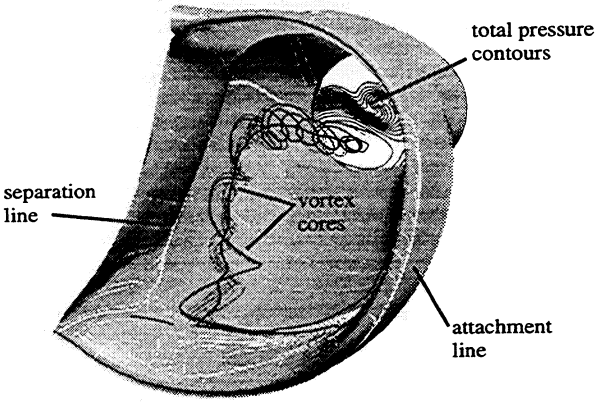

Particle traces for leeward inlet at $\alpha = 60°$, $\beta = -5°$, $M_\infty = 0.3$

(g) Front View ($\alpha = 60°$, $\beta = \pm 5°$, $0°$, $M_\infty = 0.3$)

Fig. 4: Inlet Flow Particle Trajectories

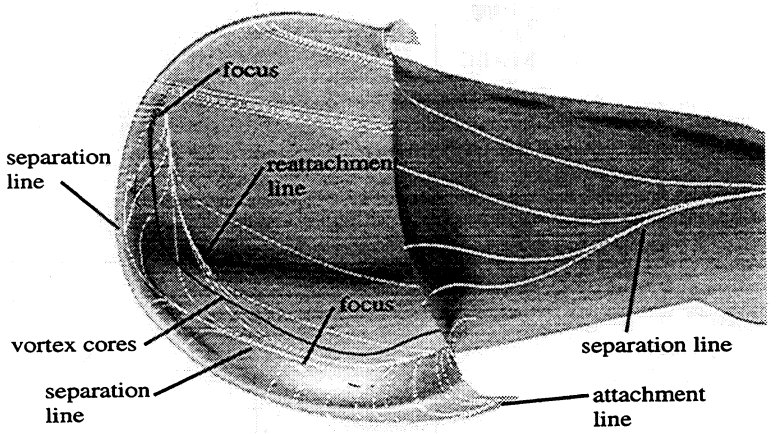

Particle traces for windward inlet at $\alpha = 60°$, $\beta = +5°$, $M_\infty = 0.3$

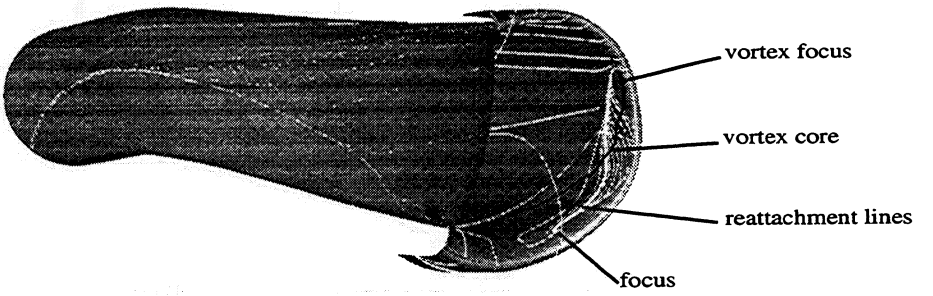

Particle traces for leeward inlet at $\alpha = 60°$, $\beta = 0°$, $M_\infty = 0.3$

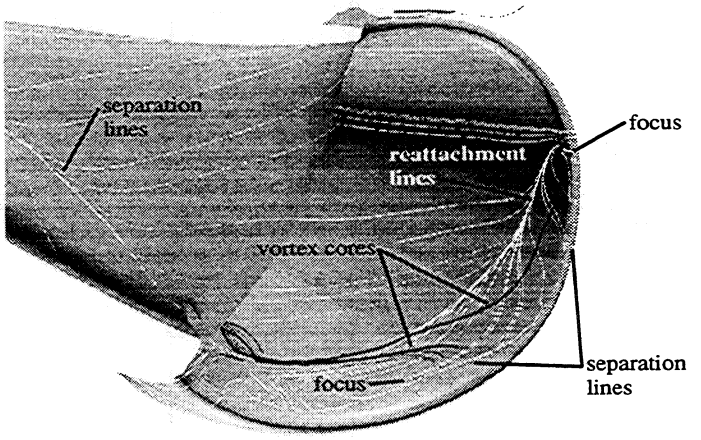

Particle traces for leeward inlet at $\alpha = 60°$, $\beta = -5°$, $M_\infty = 0.3$

(h) Side View ($\alpha = 60°$, $\beta = \pm 5°, 0°$, $M_\infty = 0.3$)

Fig. 4: Inlet Flow Particle Trajectories

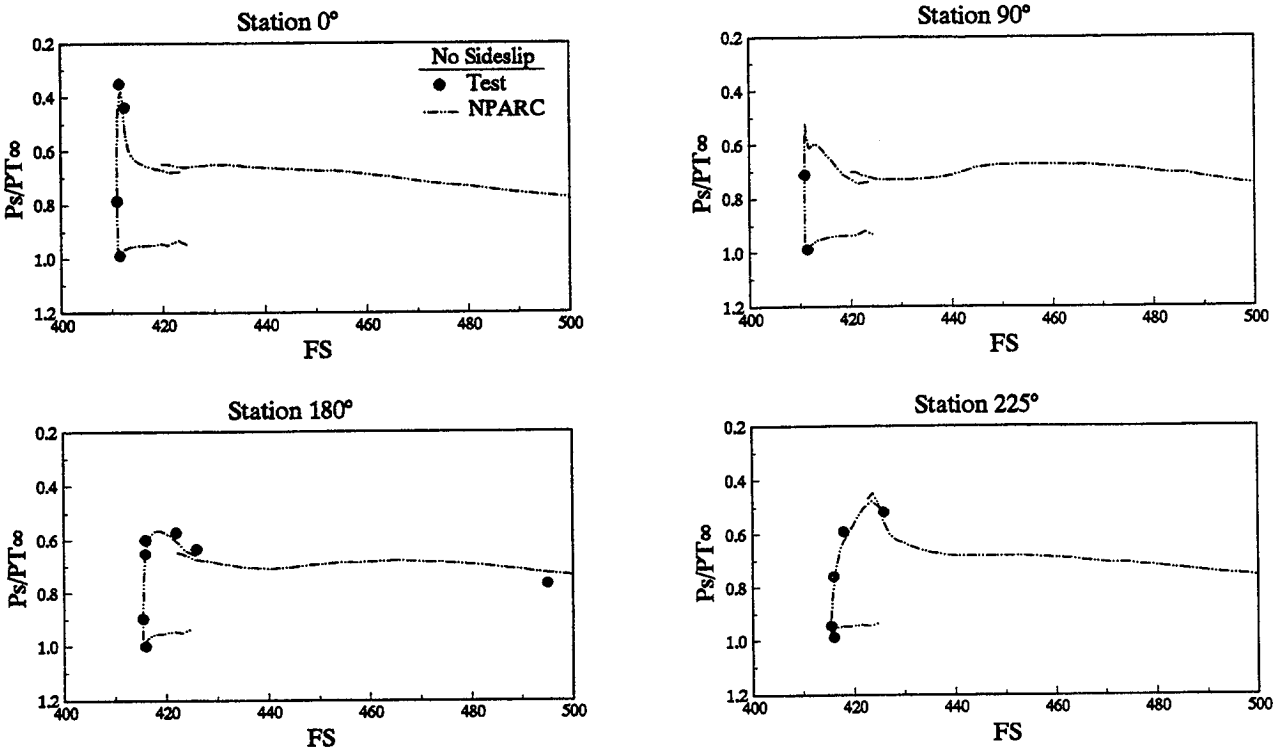

(a). $M\infty = 0.30, \alpha = 3°$

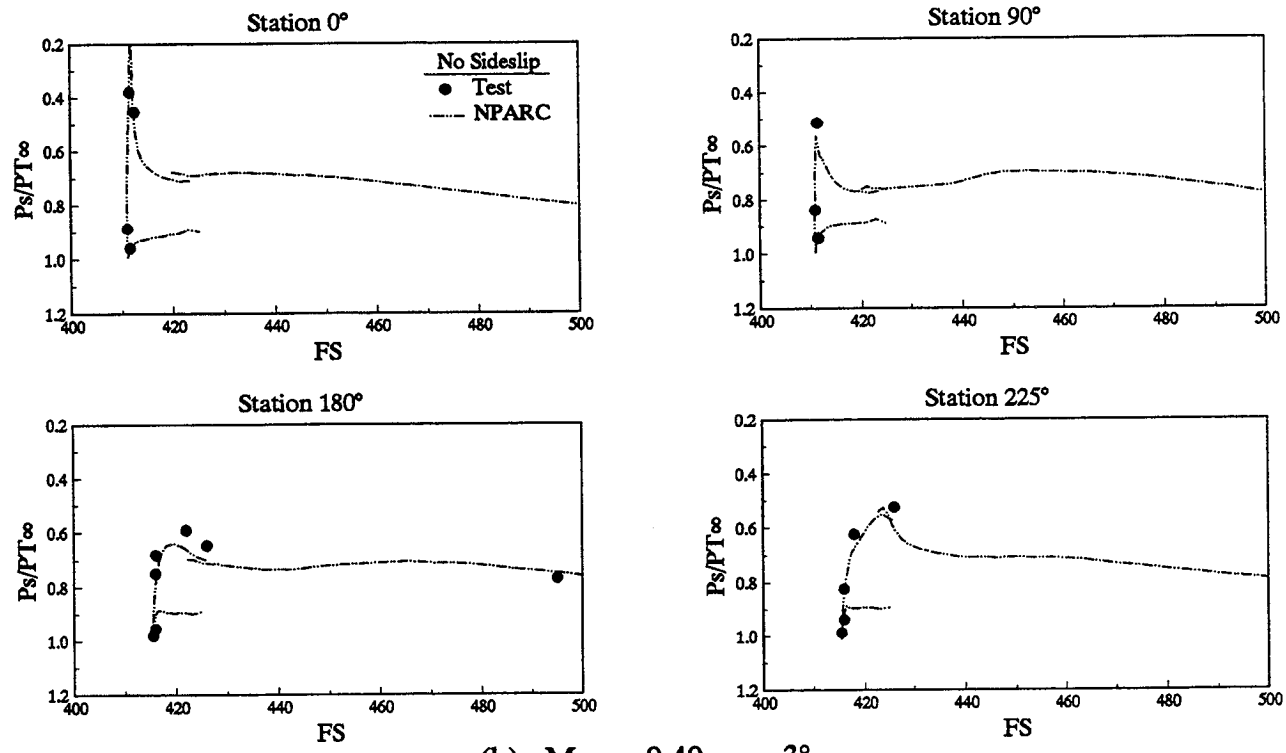

(b). $M\infty = 0.40, \alpha = 3°$

Fig. 5 - Inlet Lip and Duct Surface Pressures

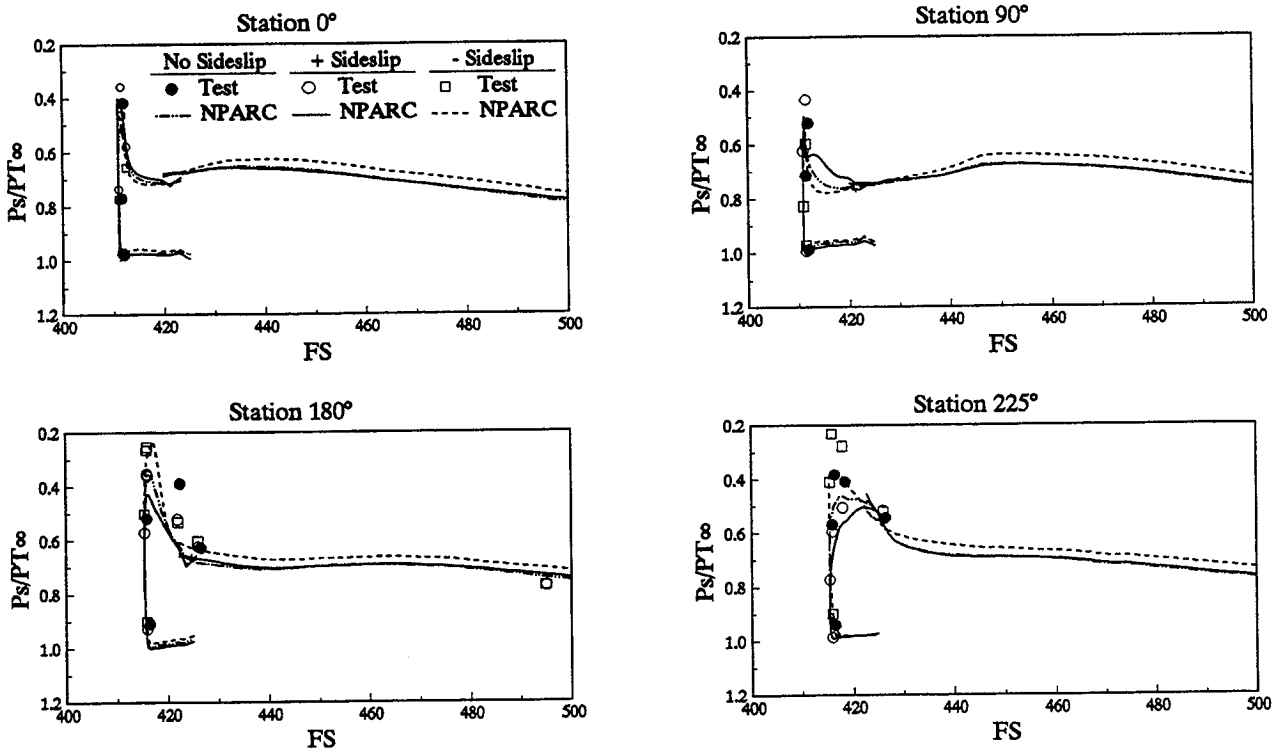

(c). $M\infty = 0.30, \alpha = 30°, ß = 0°, \pm 10°$

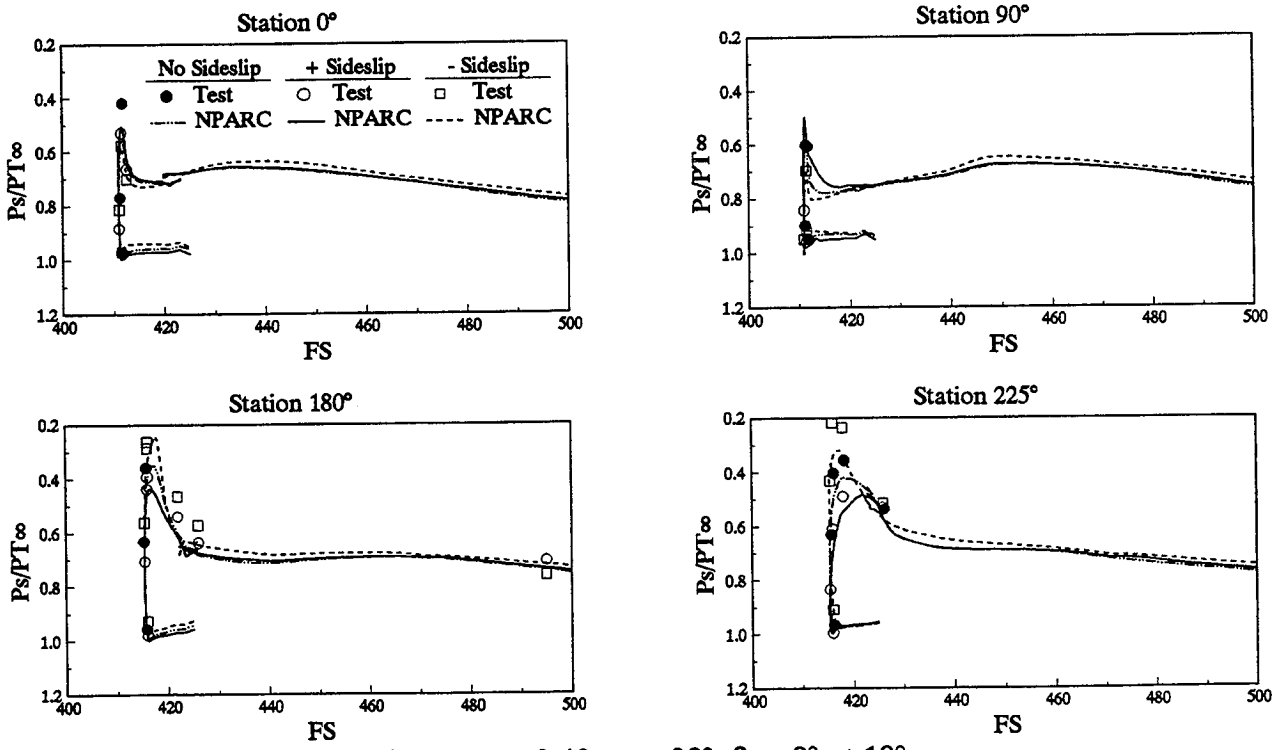

(d). $M\infty = 0.40, \alpha = 30°, ß = 0°, \pm 10°$

Fig. 5 - Inlet Lip and Duct Surface Pressures

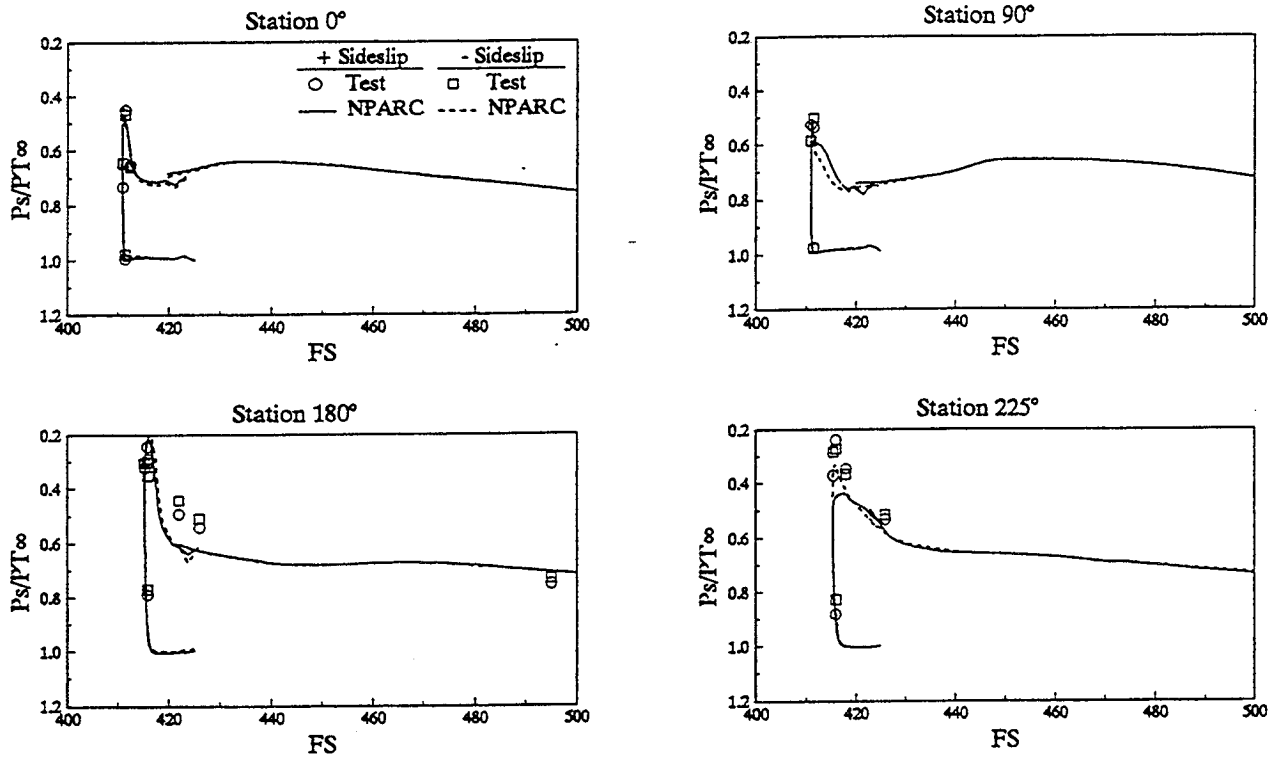

(e). M∞ = 0.30, α = 50°, ß = ±5°

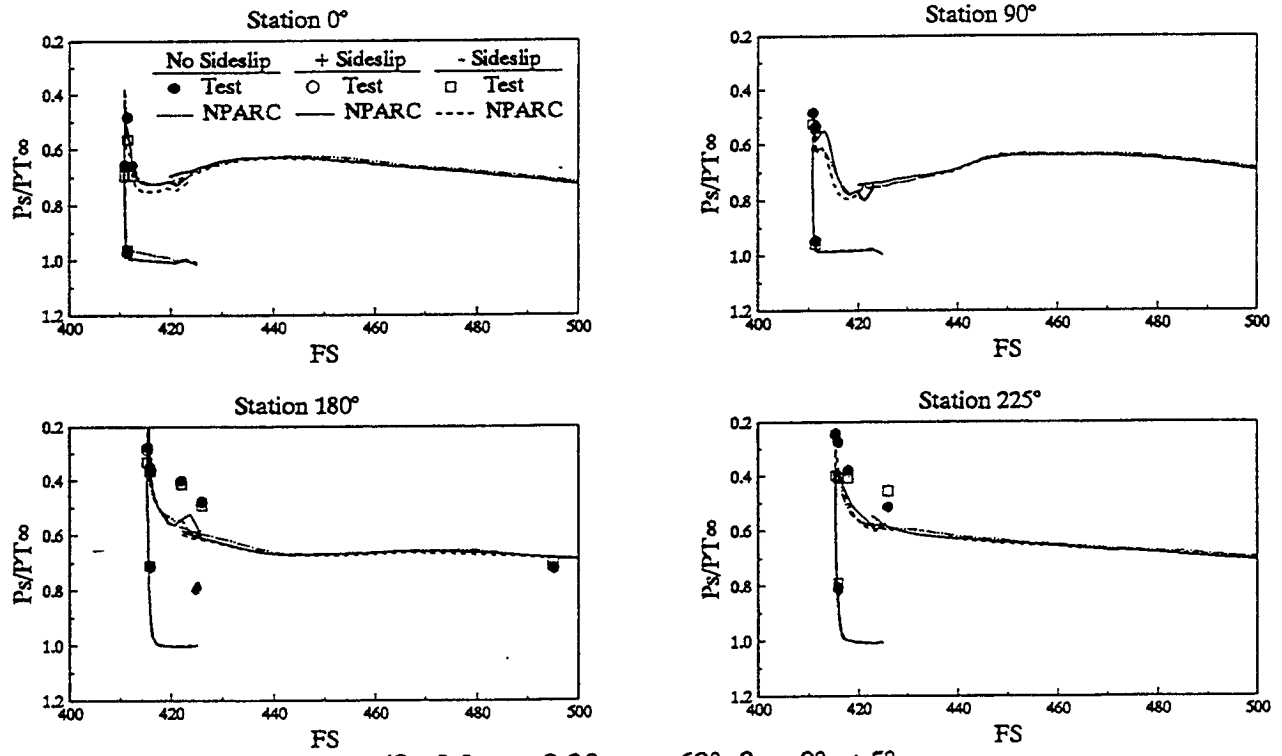

(f). M∞ = 0.30, α = 60°, ß = 0°, ±5°

Fig. 5 - Inlet Lip and Duct Surface Pressures

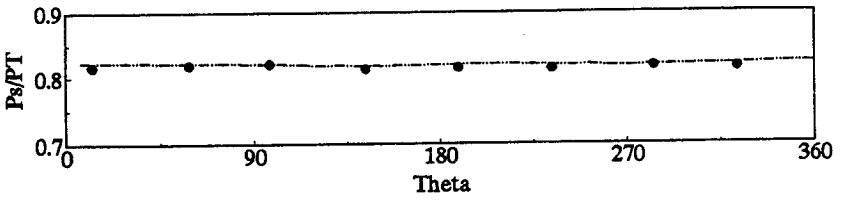

a). $M\infty = 0.30, \alpha = 3°, \beta = 0°$

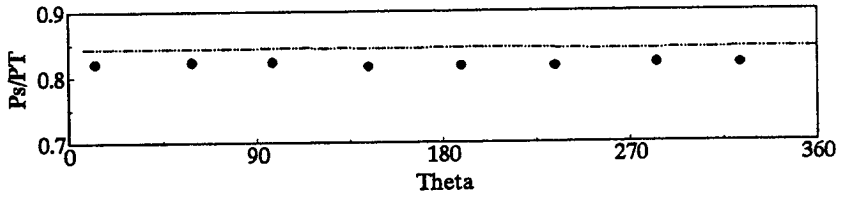

b). $M\infty = 0.40, \alpha = 3°, \beta = 0°$

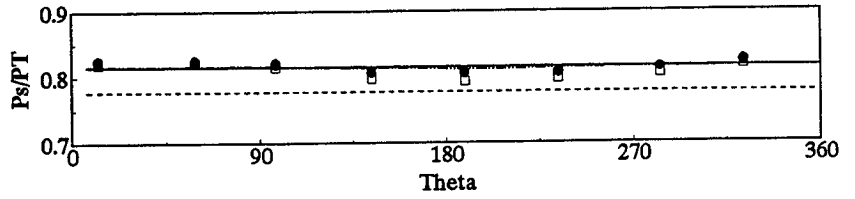

c). $M\infty = 0.30, \alpha = 30°, \beta = 0°, \pm 10°$

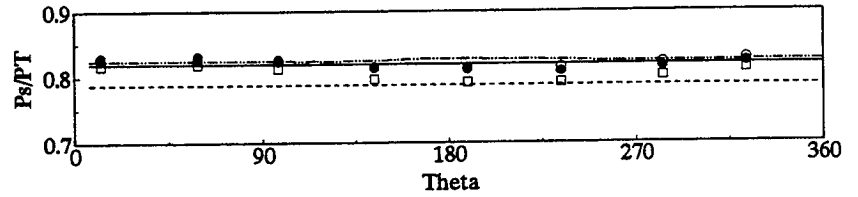

d). $M\infty = 0.40, \alpha = 30°, \beta = 0°, \pm 10°$

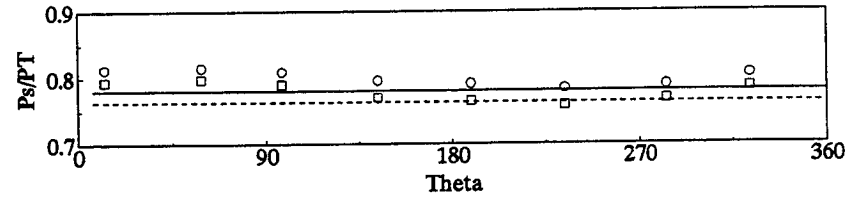

e). $M\infty = 0.30, \alpha = 50°, \beta = \pm 5°$

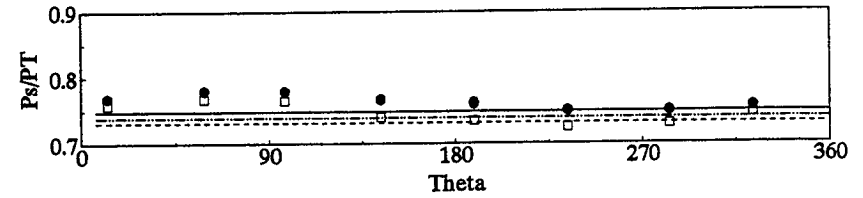

f). $M\infty = 0.30, \alpha = 60°, \beta = 0°, \pm 5°$

● Test, No Sideslip —— NPARC, (No Sideslip)
○ Test, + Sideslip —— NPARC, (+ Sideslip)
□ Test, - Sideslip ---- NPARC, (- Sideslip)

Fig. 6 - Engine Face Circumferential Surface Pressures

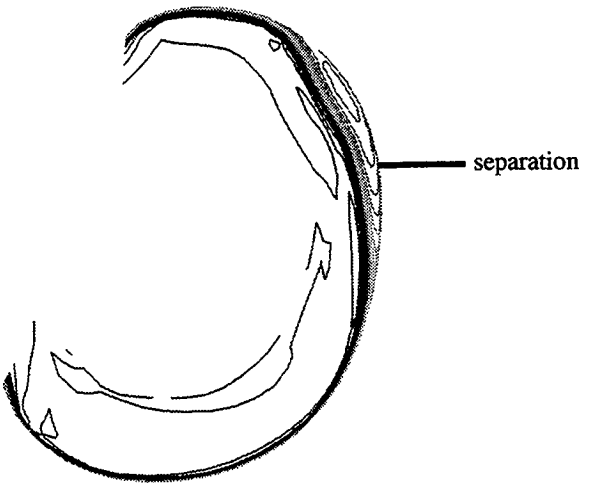

(a) $\alpha = 3°, \beta = 0°, M_\infty = 0.3$

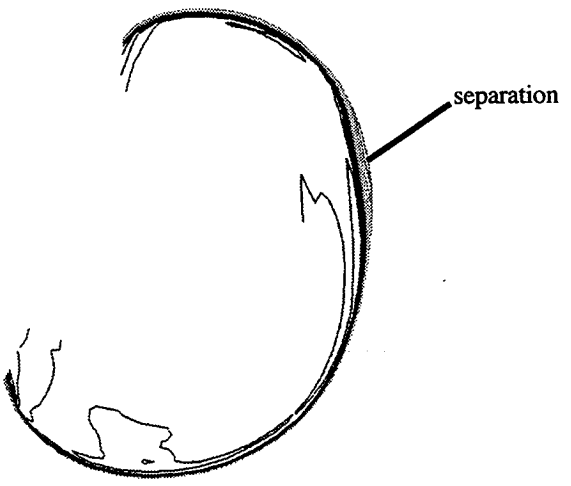

(b) $\alpha = 3°, \beta = 0°, M_\infty = 0.4$

Fig. 7: Inlet Entrance Total Pressure Contours

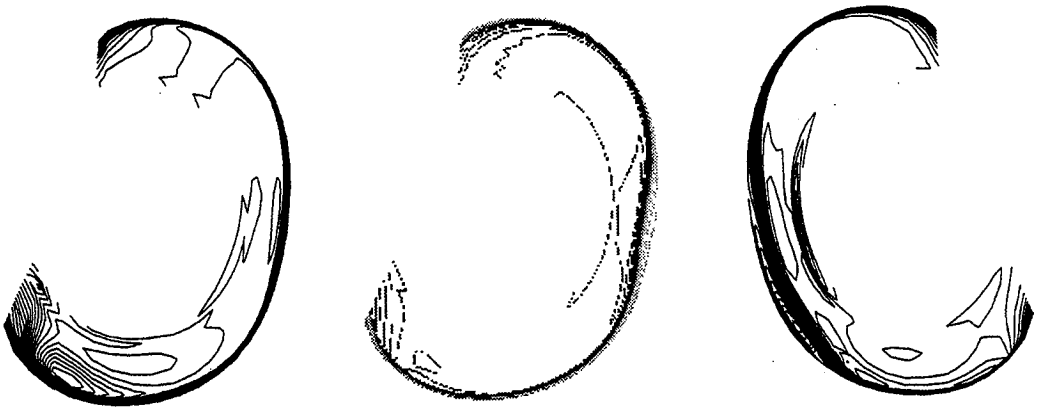

(c) α=30°, β=–10°, M_∞=0.3 α=30°, β=0°, M_∞=0.3 α=30°, β=+10°, M_∞=0.3

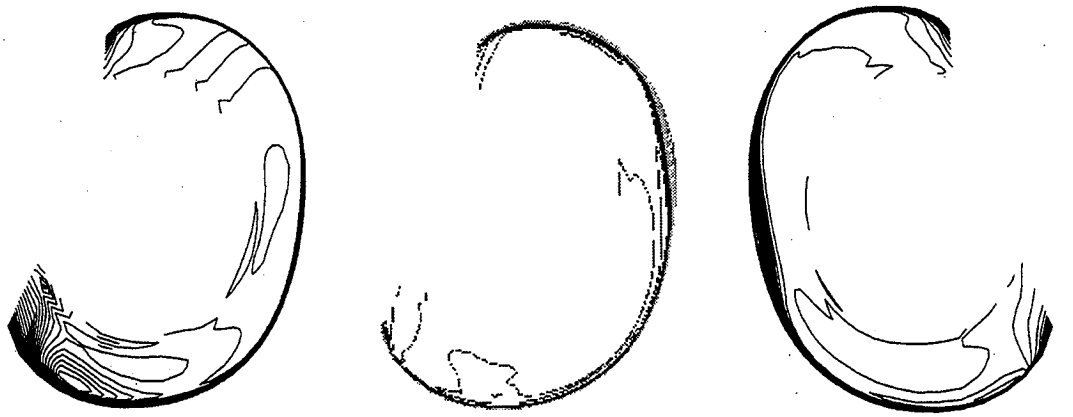

(d) α=30°, β=–10°, M_∞=0.4 α=30°, β=0°, M_∞=0.4 α=30°, β=+10°, M_∞=0.4

Fig. 7: Inlet Entrance Total Pressure Contours

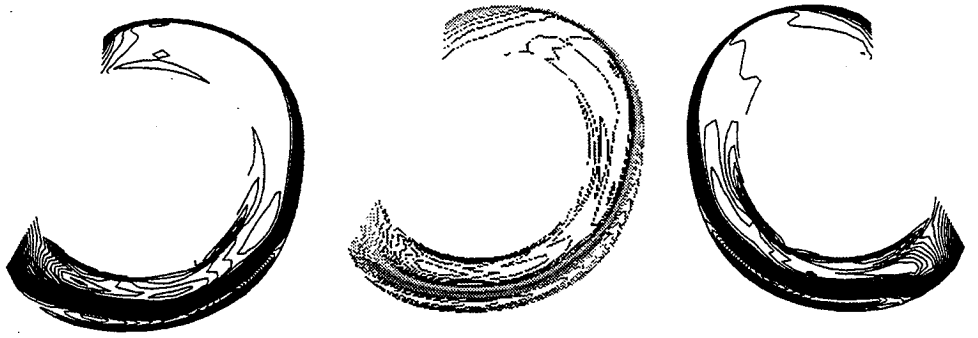

α=60°, β=–5°, M_∞=0.3 α=60°, β=0°, M_∞=0.3 α=60°, β=+5°, M_∞=0.3

(e) α=60°, β=±5°, M_∞=0.3

Fig. 7: Inlet Entrance Total Pressure Contours

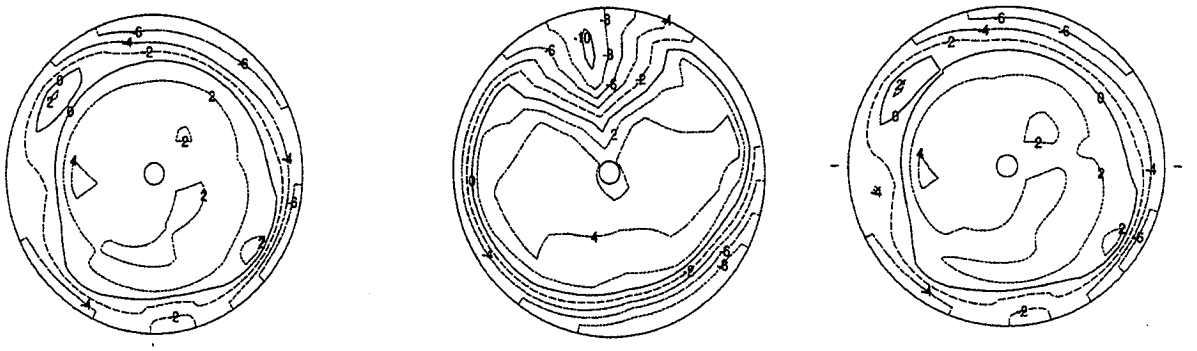

(a) α=3°, β=0°, M_∞=0.3

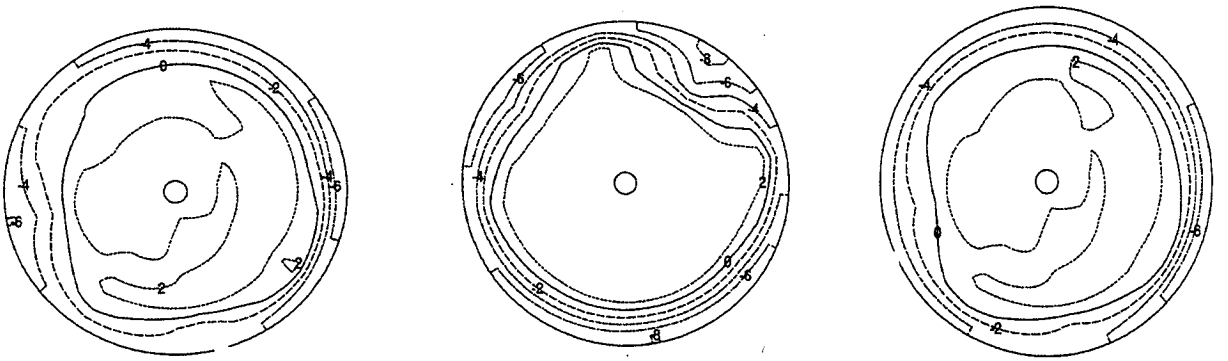

(b) α=3°, β=0°, M_∞=0.4

Extreme 1 **NPARC** **Extreme 2**

Fig. 8: Engine Face Total Pressure Contours

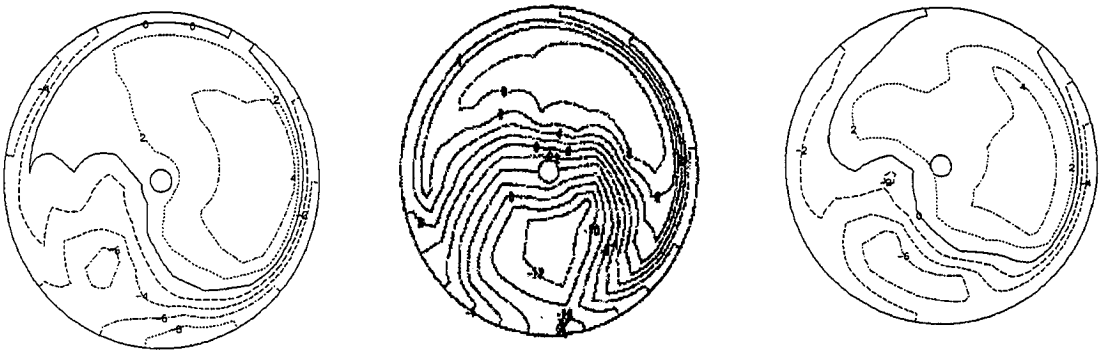

α=30°, β=–10°, M_∞=0.3

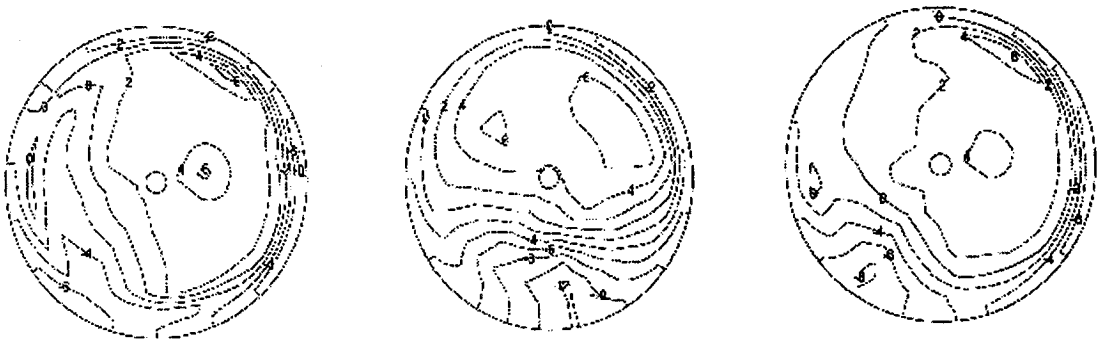

α=30°, β=0°, M_∞=0.3

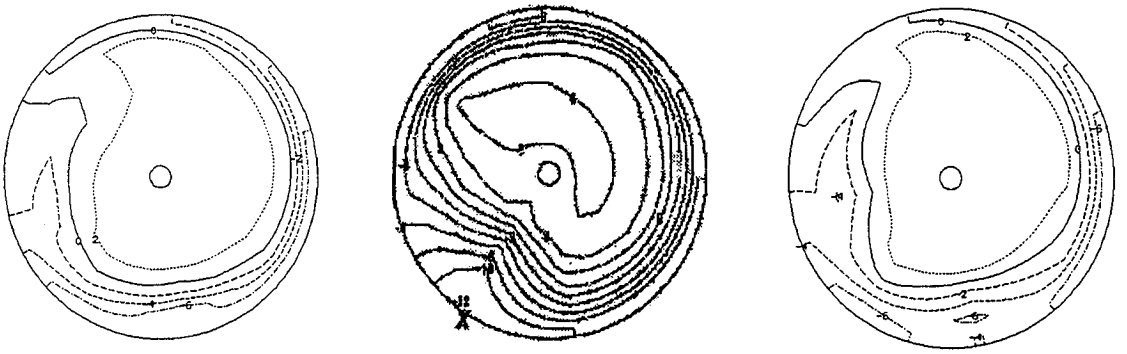

α=30°, β=+10°, M_∞=0.3

Extreme 1 **NPARC** **Extreme 2**

(c) α=30°, β=±10°, 0°, M_∞=0.3

Fig. 8: Engine Face Total Pressure Contours

α=30°, β=–10°, M_∞=0.4

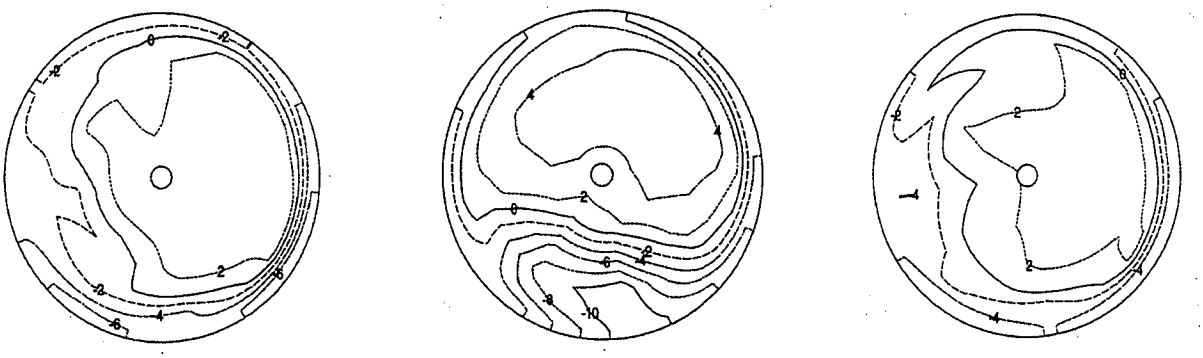

α=30°, β=0°, M_∞=0.4

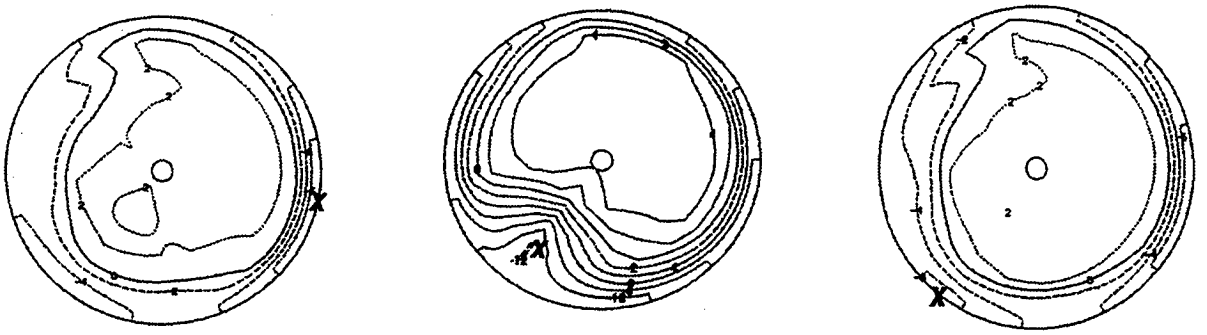

α=30°, β=+10°, M_∞=0.4

Extreme 1 **NPARC** **Extreme 2**

(d) α=30°, β=±10°, 0°, M_∞=0.4

Fig. 8: Engine Face Total Pressure Contours

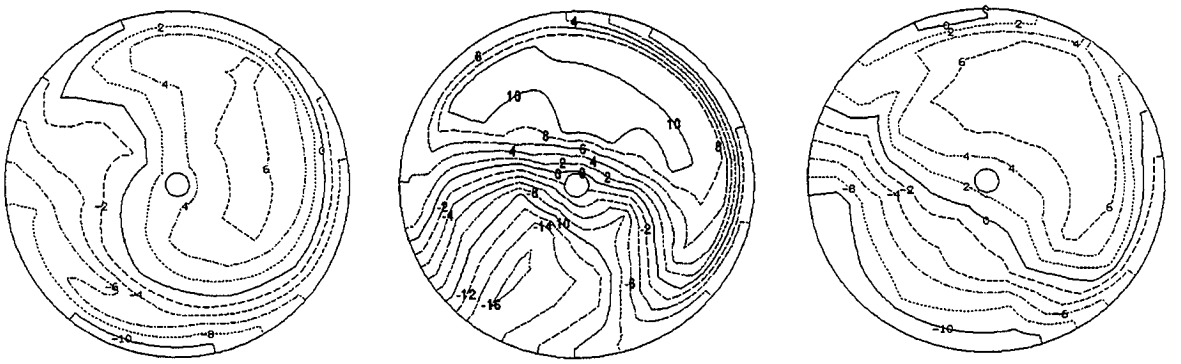

α=50°, β=–5°, M_∞=0.3

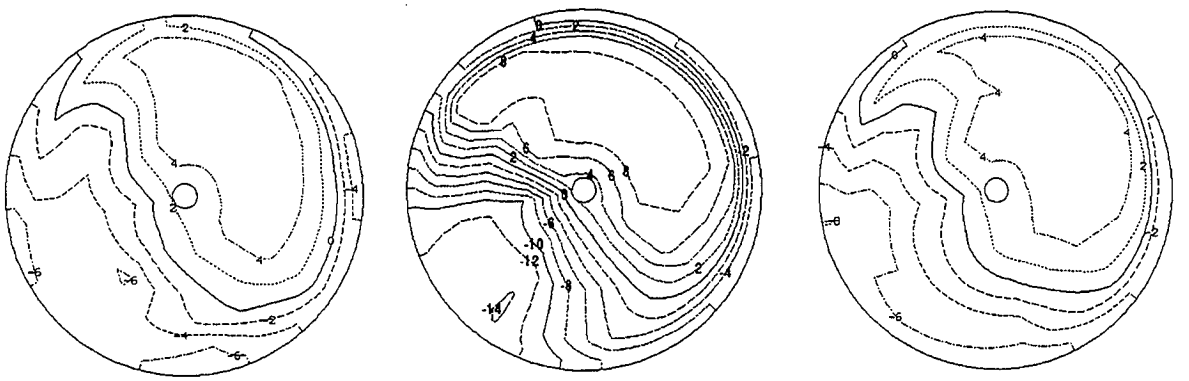

α=50°, β=+5°, M_∞=0.3

Extension 1 **NPARC** **Extension 2**

(e) α=50°, β=±5°, 0°, M_∞=0.3

Fig. 8: Engine Face Total Pressure Contours

α=60°, β=–5°, M_∞=0.3

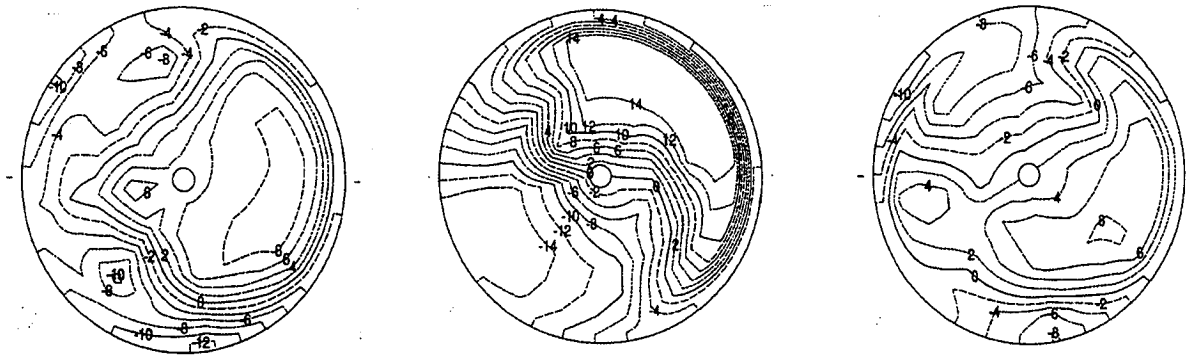

α=60°, β=0°, M_∞=0.3

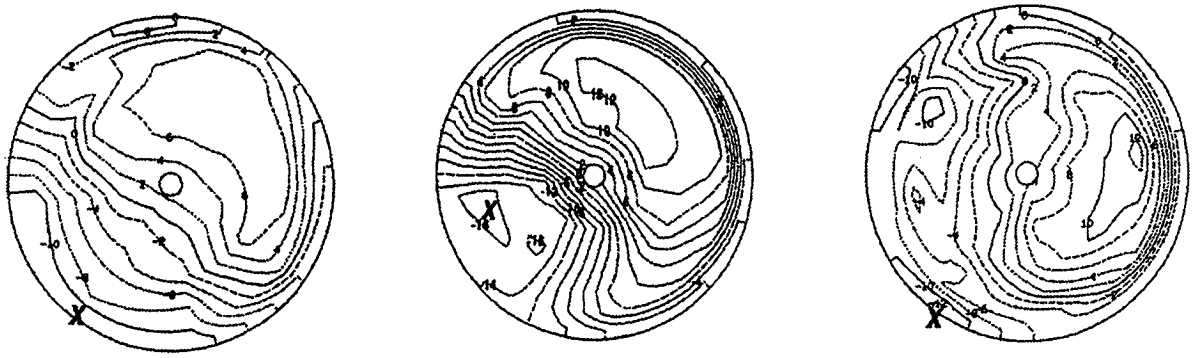

α=60°, β=+5°, M_∞=0.3

Extreme 1 **NPARC** **Extreme 2**

(f) α=60°, β=±5°, 0°, M_∞=0.3

Fig. 8: Engine Face Total Pressure Contours

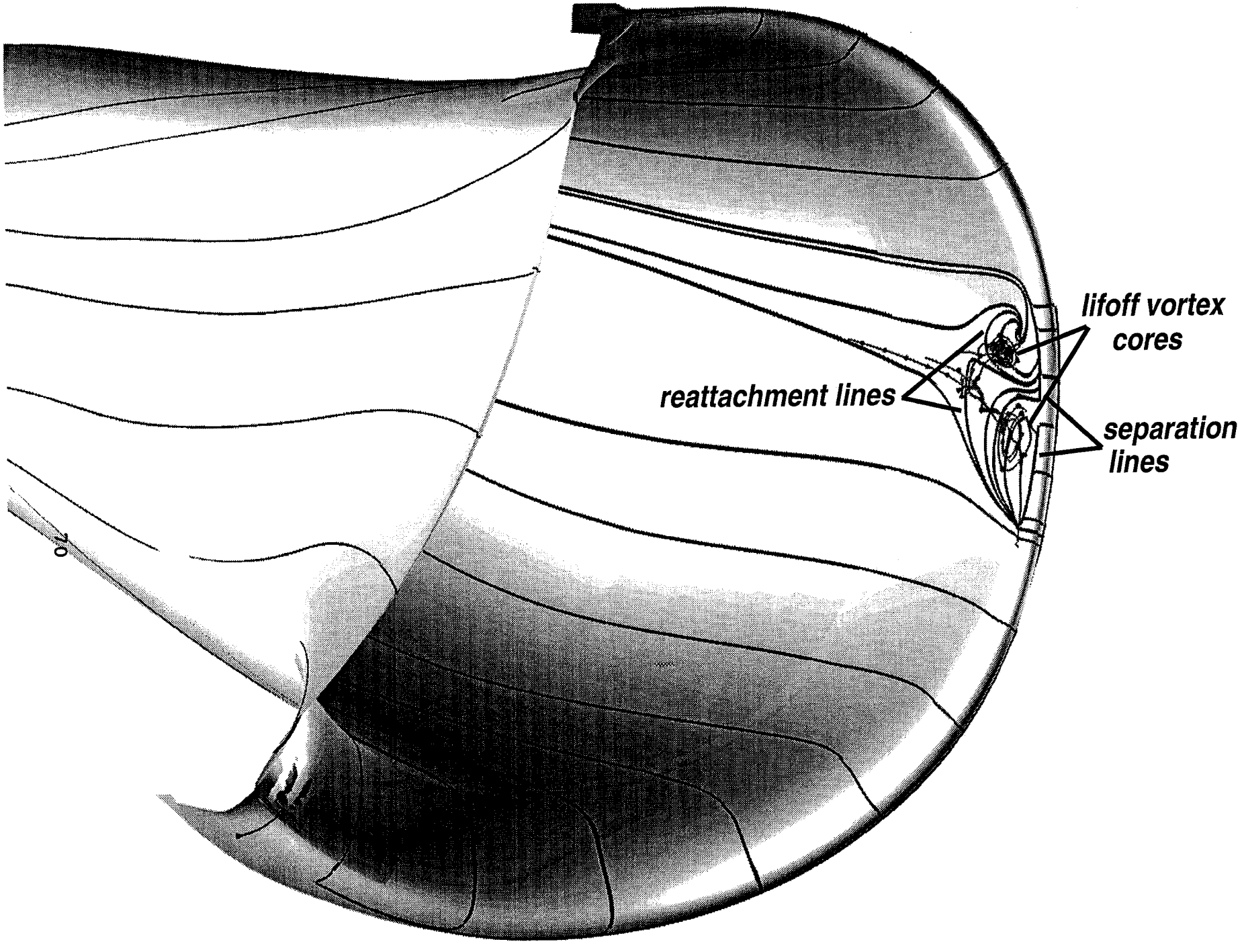

Fig. 9(a) Particle Traces along High-Density Grid Inlet

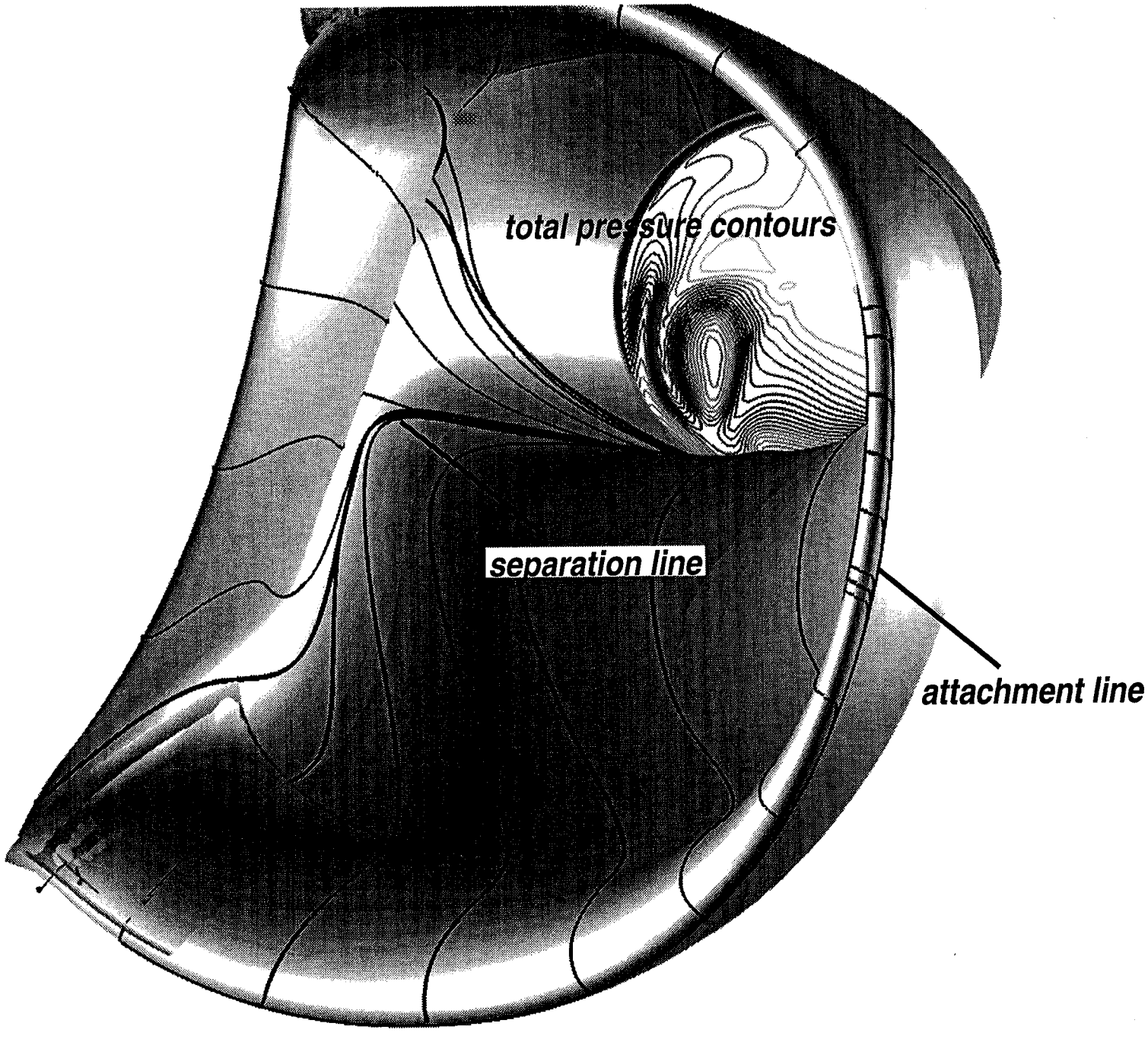

Fig. 9(b) Particle Traces for High Density Grid Inlet

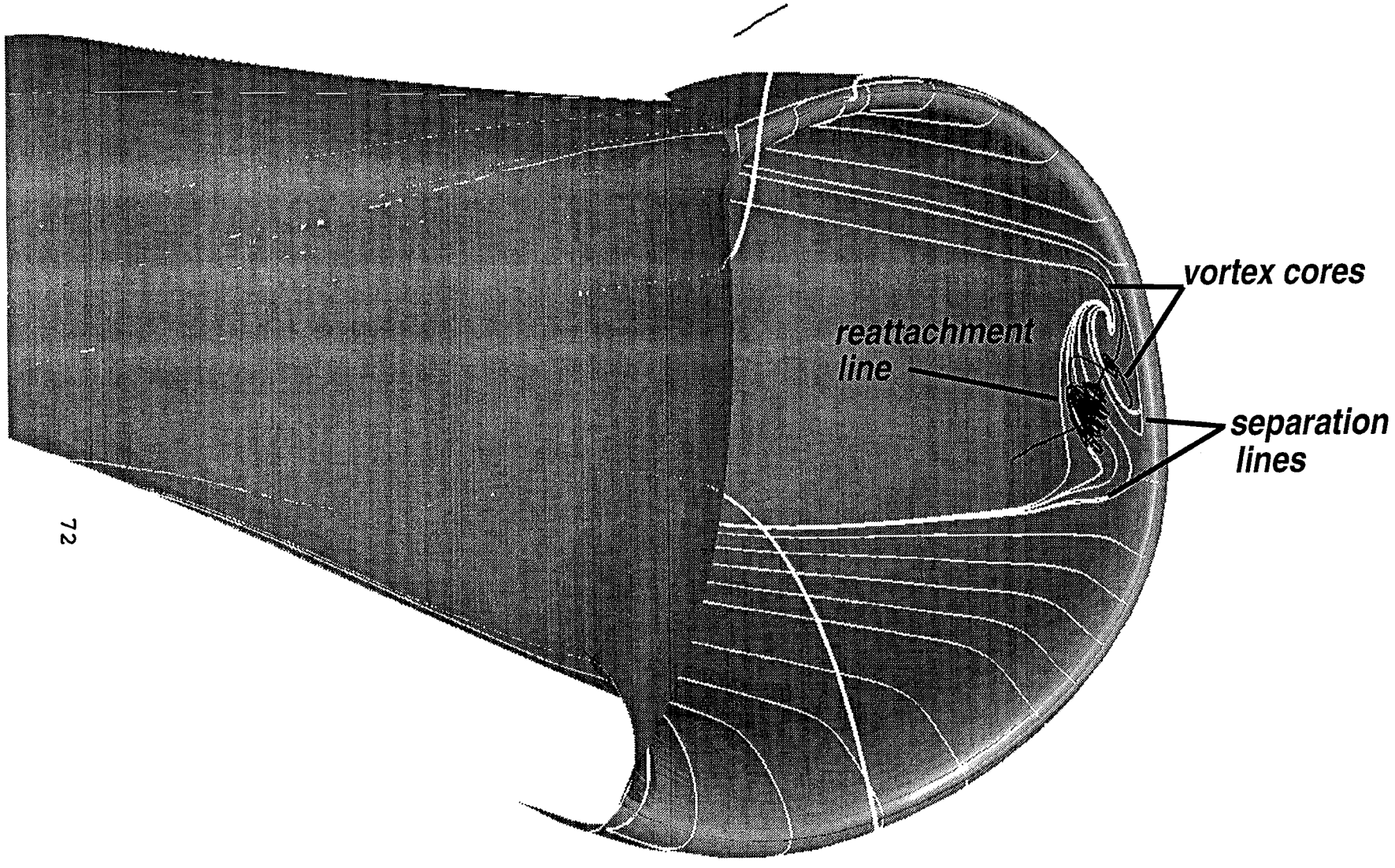

Fig. 9(c) Particle Traces Along Low-Density Grid Inlet

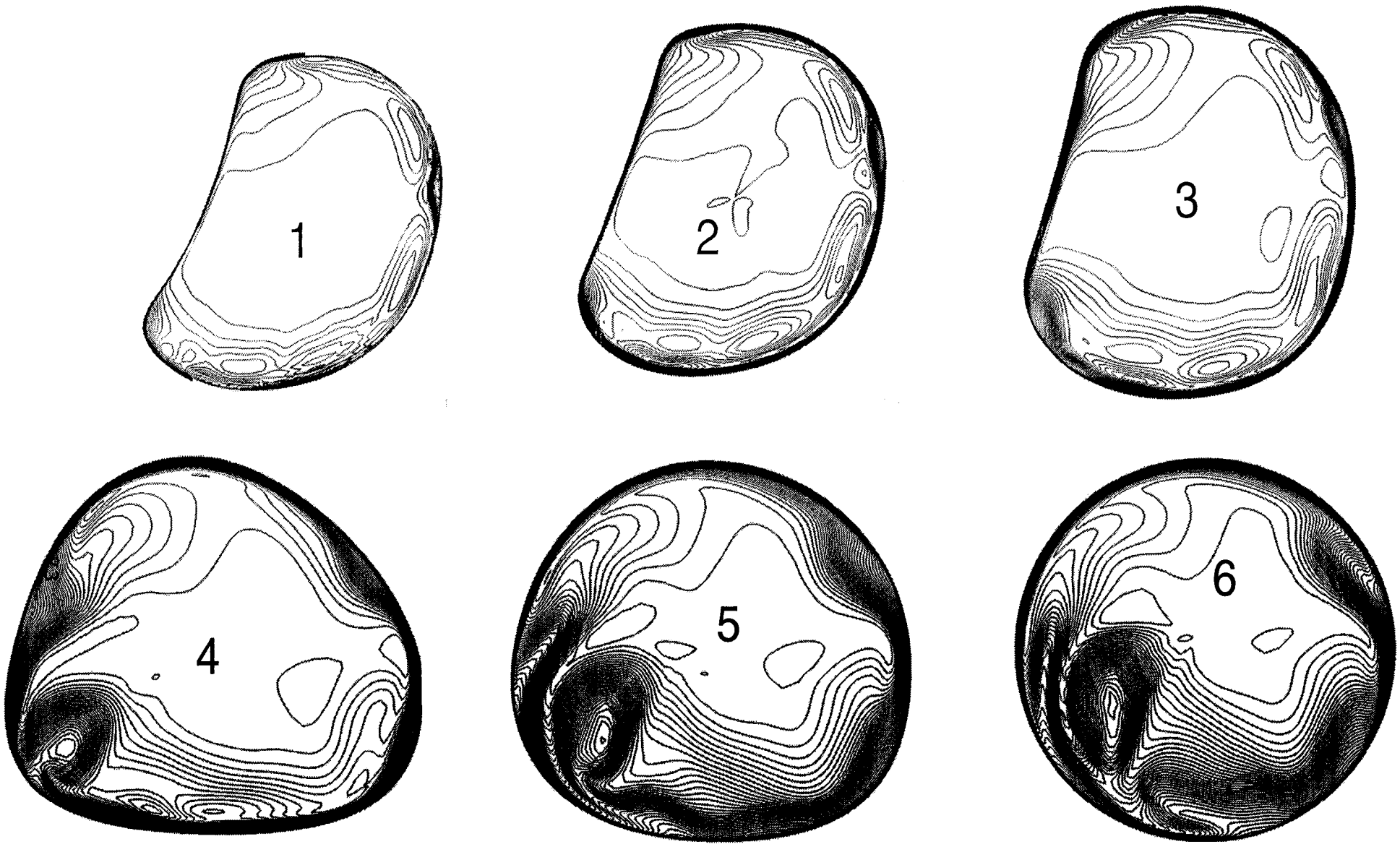

Fig. 10(a) Total Pressure Contours Along Inlet Duct

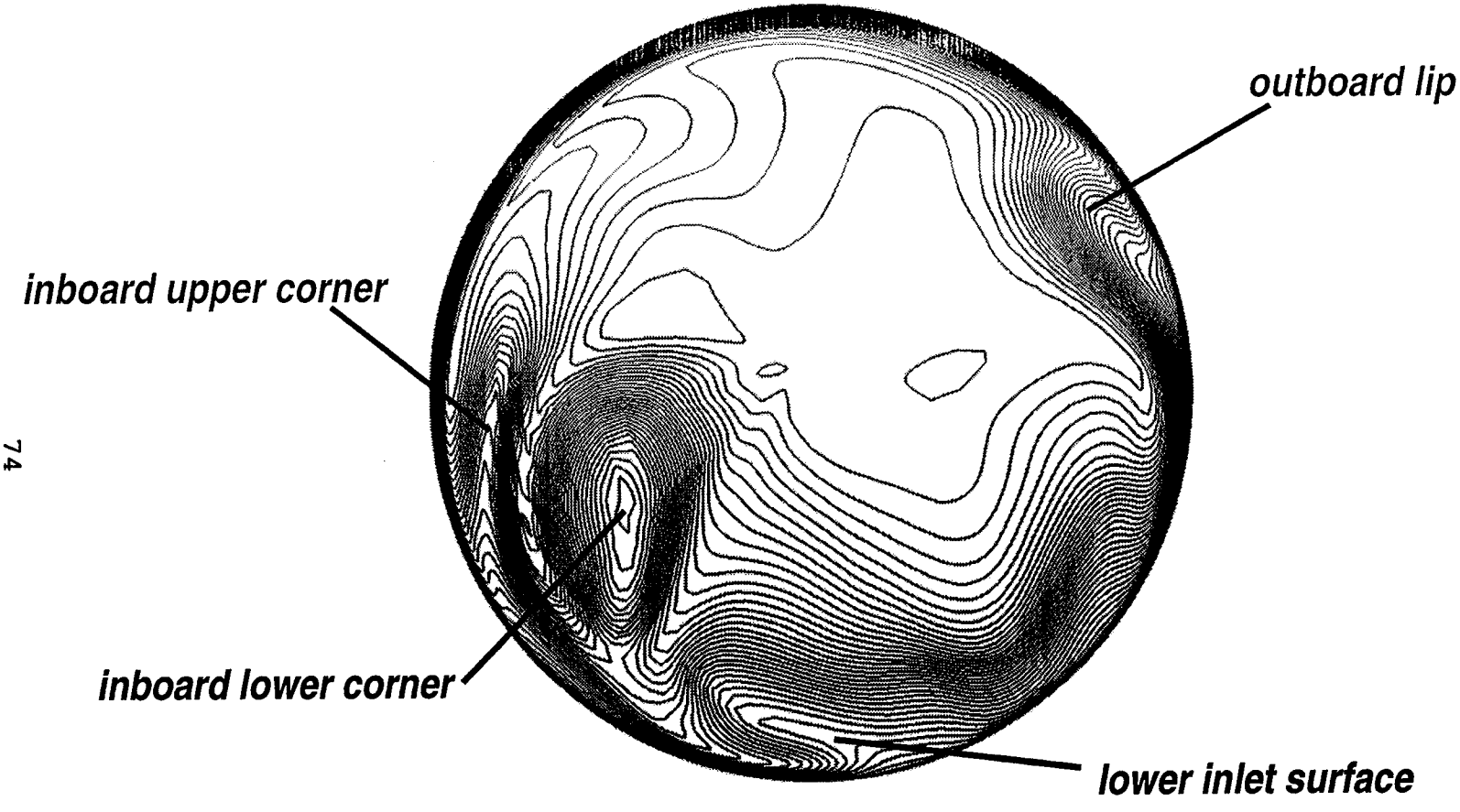

Fig. 10(b) Total Pressure Contours at Engine Face

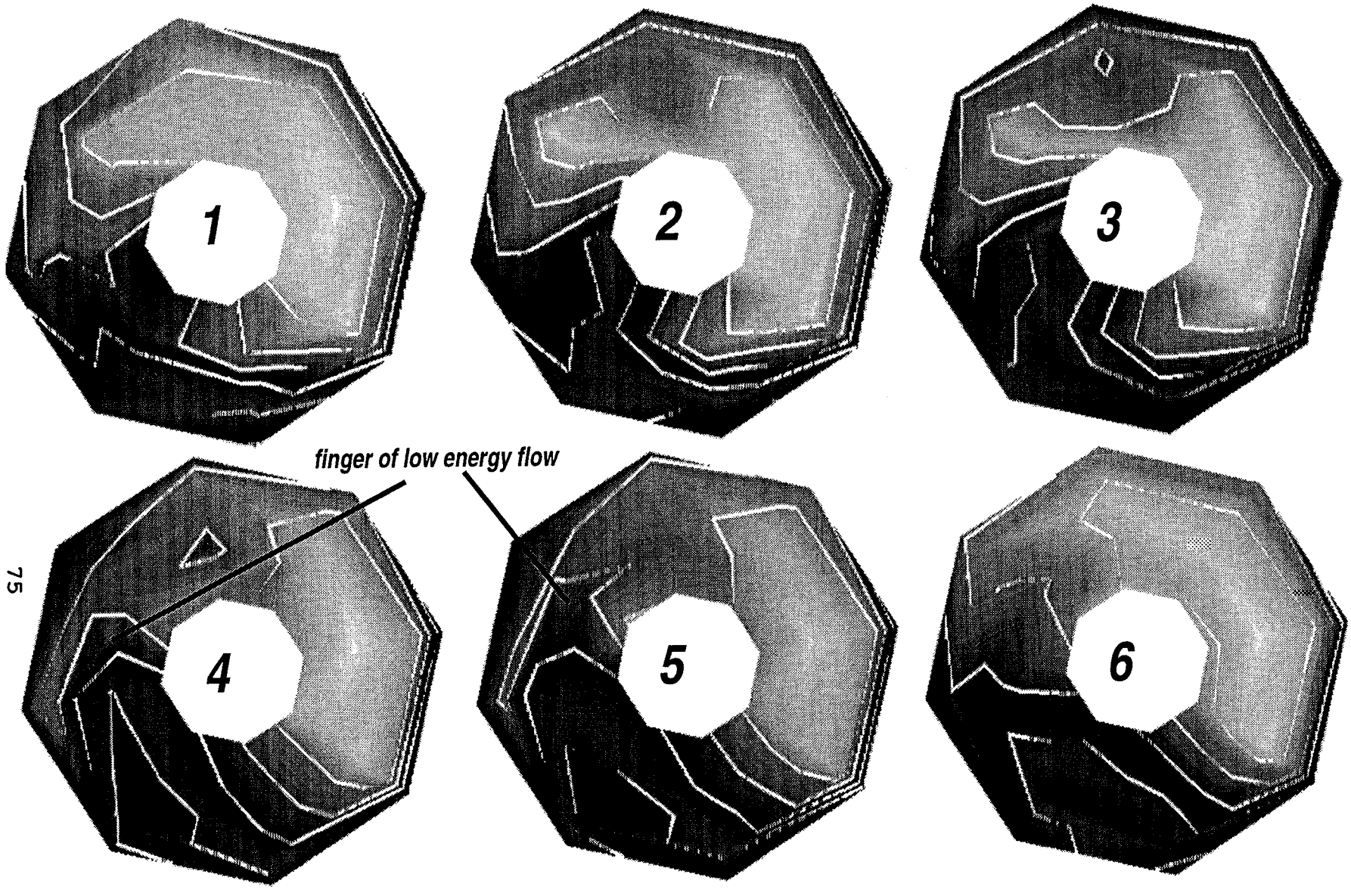

Fig.10(c) Time Sequence of Flight-Test Engine Face Total Pressure Contours

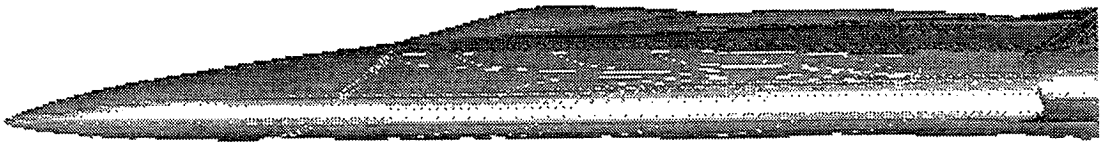

(a) Baldwin–Lomax

(b) Baldwin–Barth

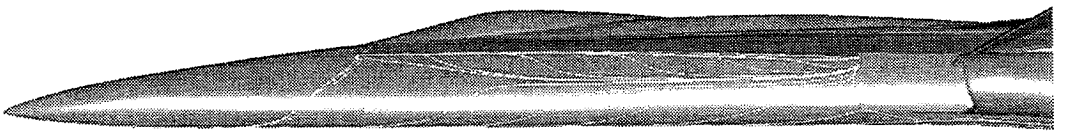

(c) K–ε

Restricted Particle Traces

Fig. 11: External Flow Field

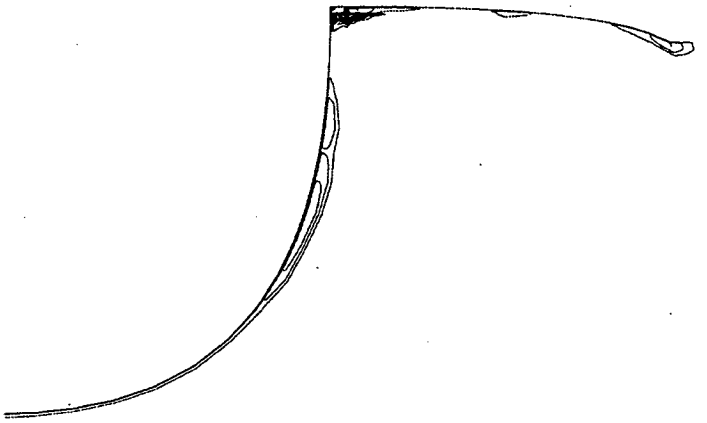

(d) Baldwin–Lomax Turbulence Model

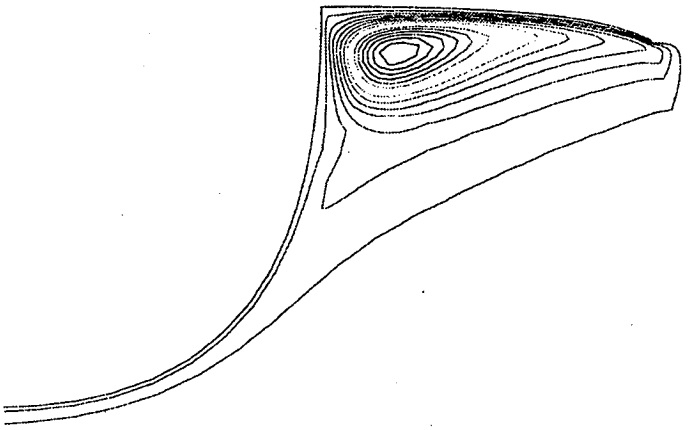

(e) Baldwin–Barth Turbulence Model

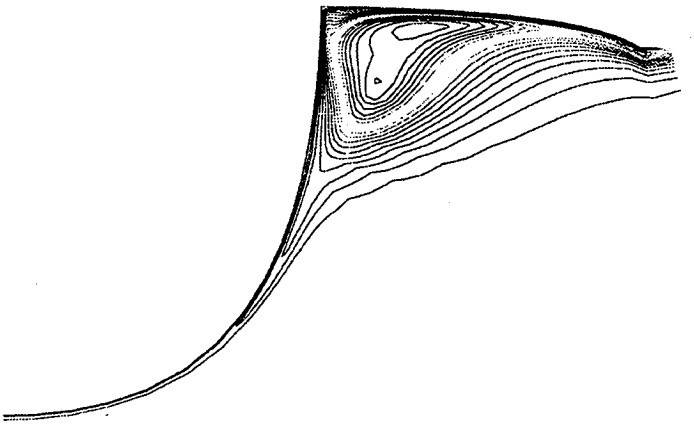

(f) k–ε Turbulence Model

Turbulent Viscosity Contours

Fig. 11: External Flow Field

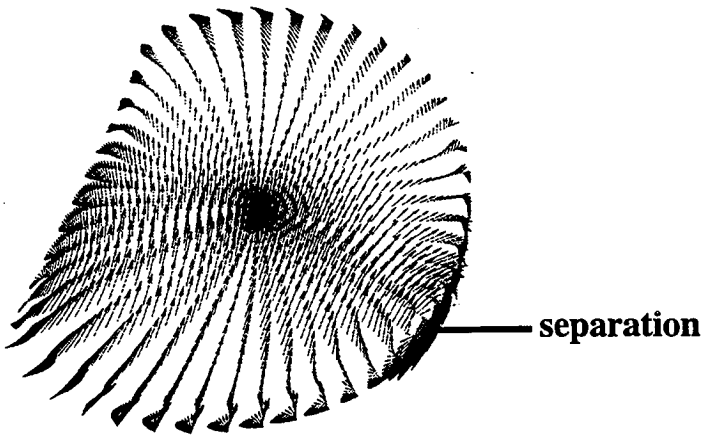

(a) Baldwin–Lomax Model

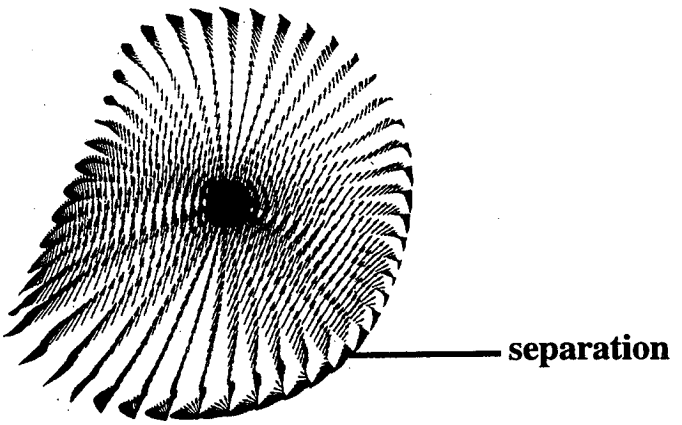

(b) Baldwin–Barth Turbulence Model

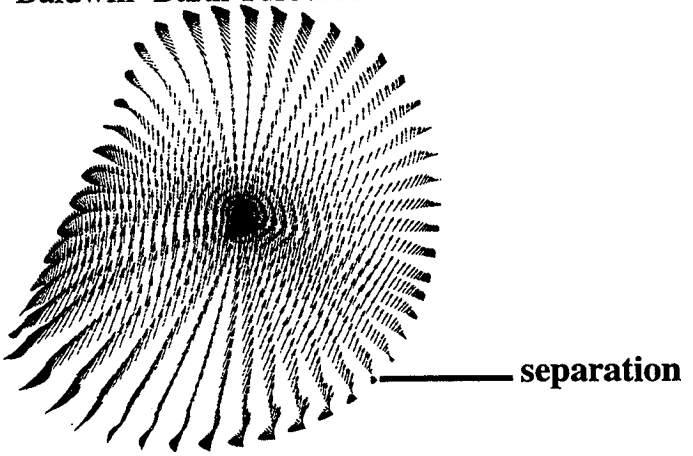

(c) k–ε Turbulence Model

Velocity Vectors

Fig. 12: Inlet Entrance Flow Field

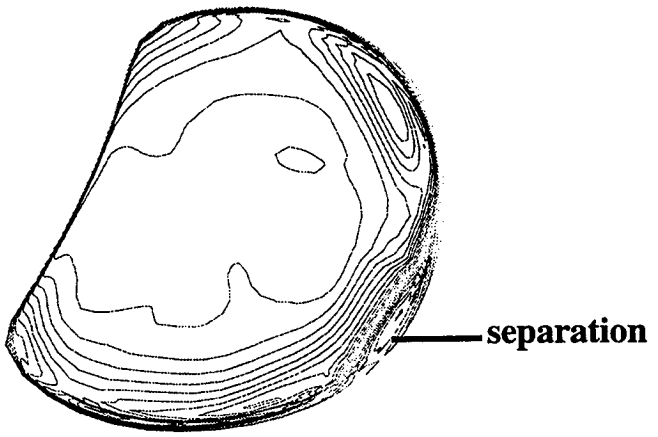

(d) Baldwin–Lomax Model

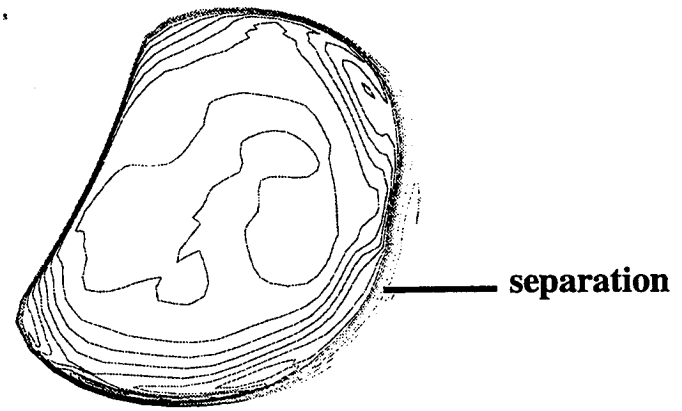

(e) Baldwin–Barth Turbulence Model

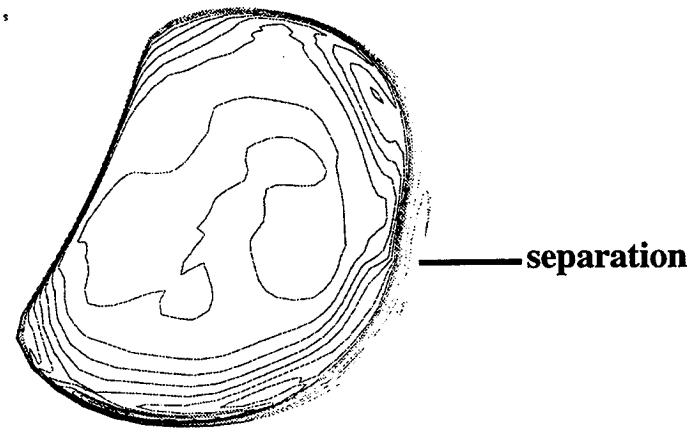

(f) Baldwin–Barth Turbulence Model

Total Pressure Contours

Fig. 12: Inlet Entrance Flow Field

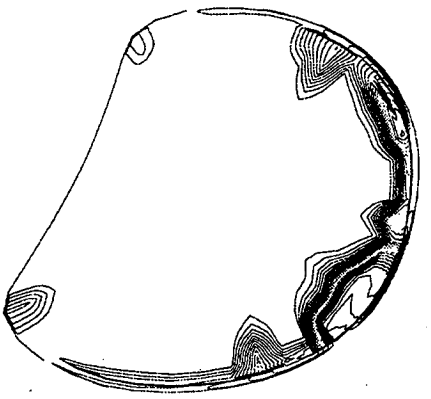

(g) Baldwin–Lomax Turbulence Model

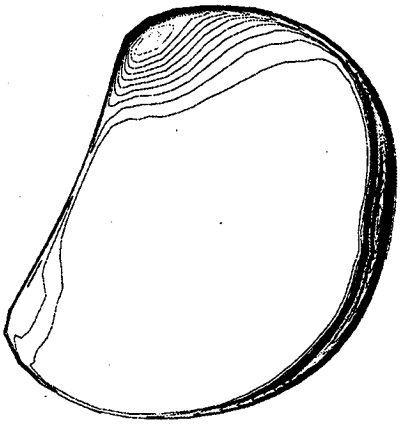

(h) Baldwin–Barth Turbulence Model

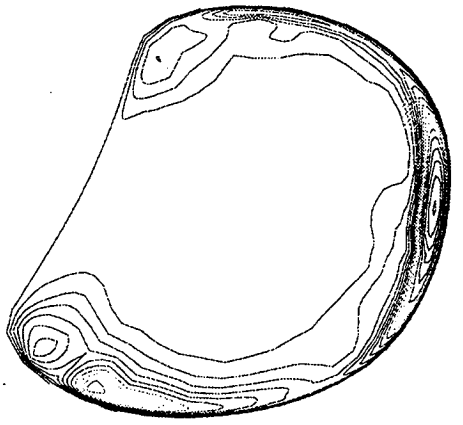

(i) k–ε Turbulence Model

Turbulent Viscosity Contours

Fig. 12: Inlet Entrance Flow Field

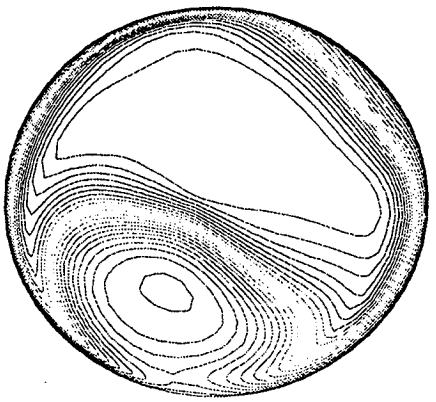

(a) Baldwin–Lomax Model

(b) Baldwin–Barth Turbulence Model

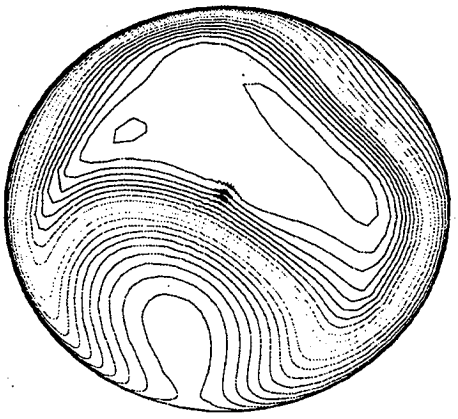

(c) k–ε Turbulence Model

Total Pressure Contours

Fig. 13: Engine Face Flow Field

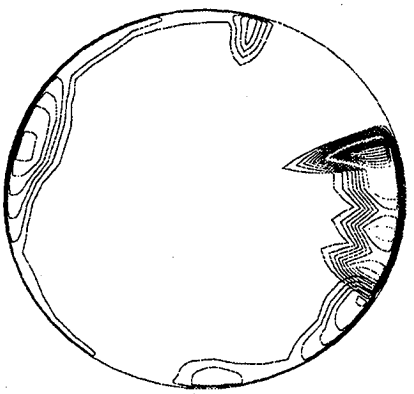

(d) Baldwin–Lomax Model

(e) Baldwin–Barth Turbulence Model

(f) k–ε Turbulence Model

Turbulent Viscosity Contours

Fig. 13: Engine Face Flow Field

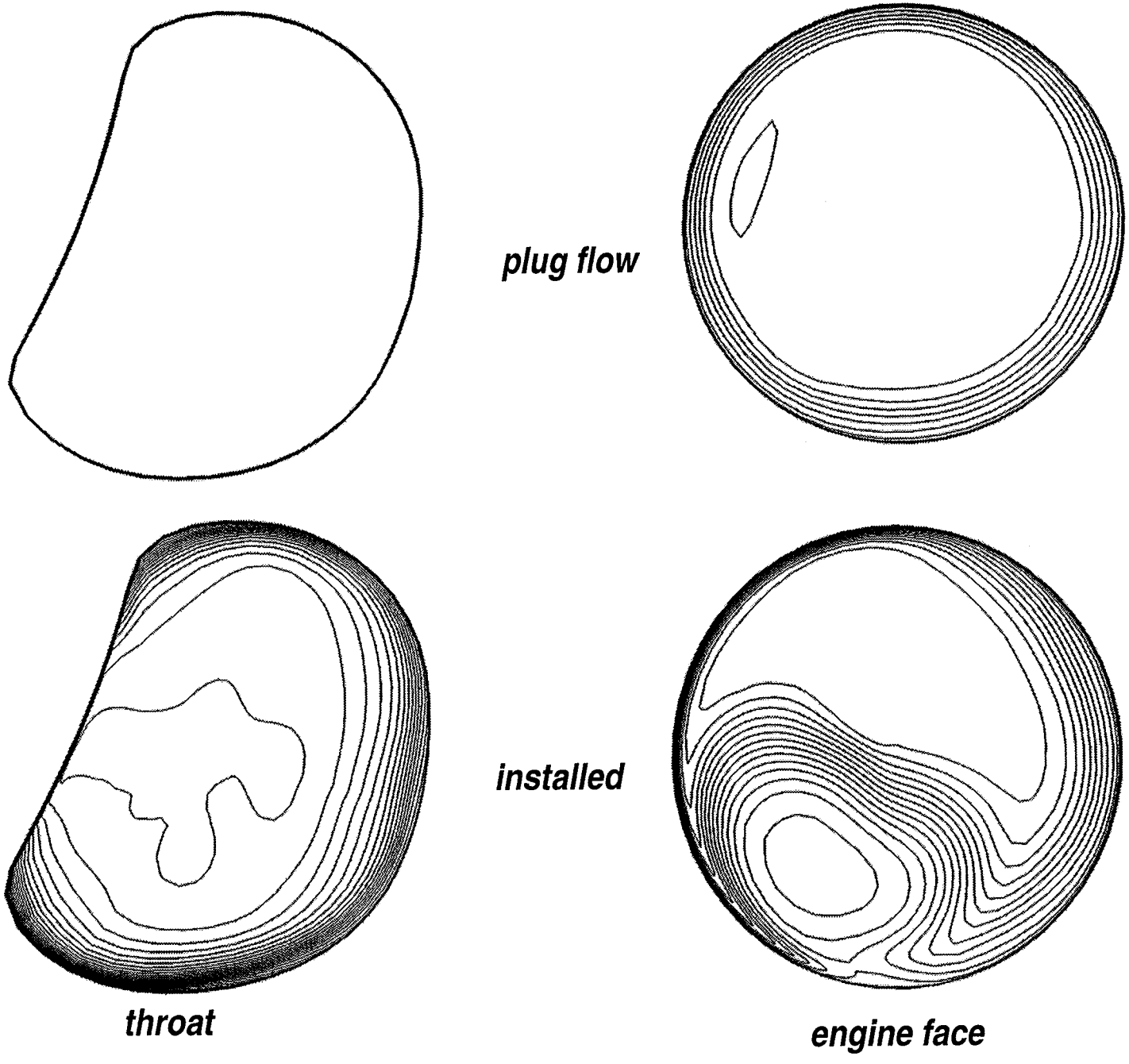

Fig. 14 Total Pressure Contours with Plug Flow Inflow

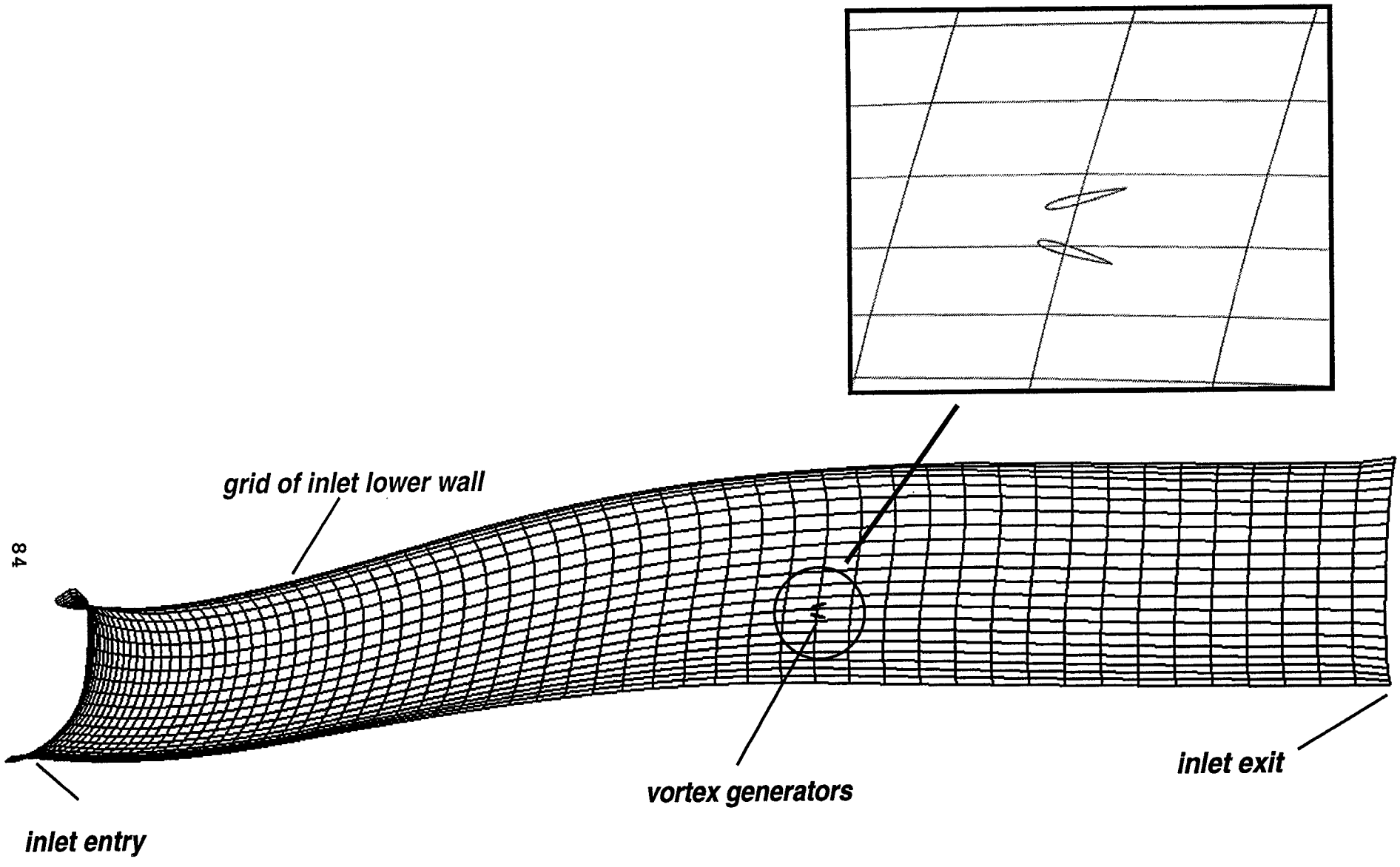

Fig. 15(a) Inlet and Vortex Generators Grid Topologies

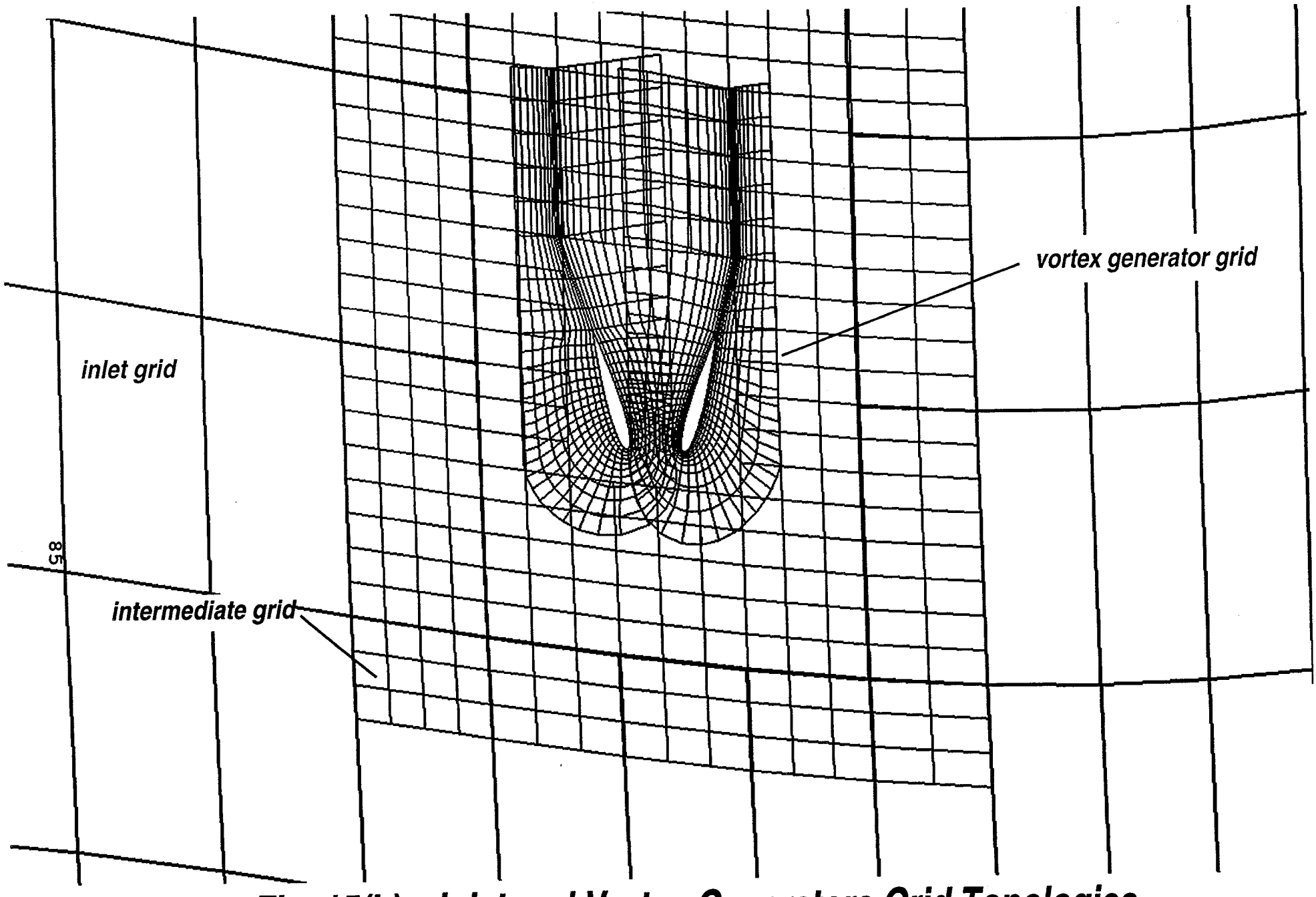

Fig. 15(b) Inlet and Vortex Generators Grid Topologies

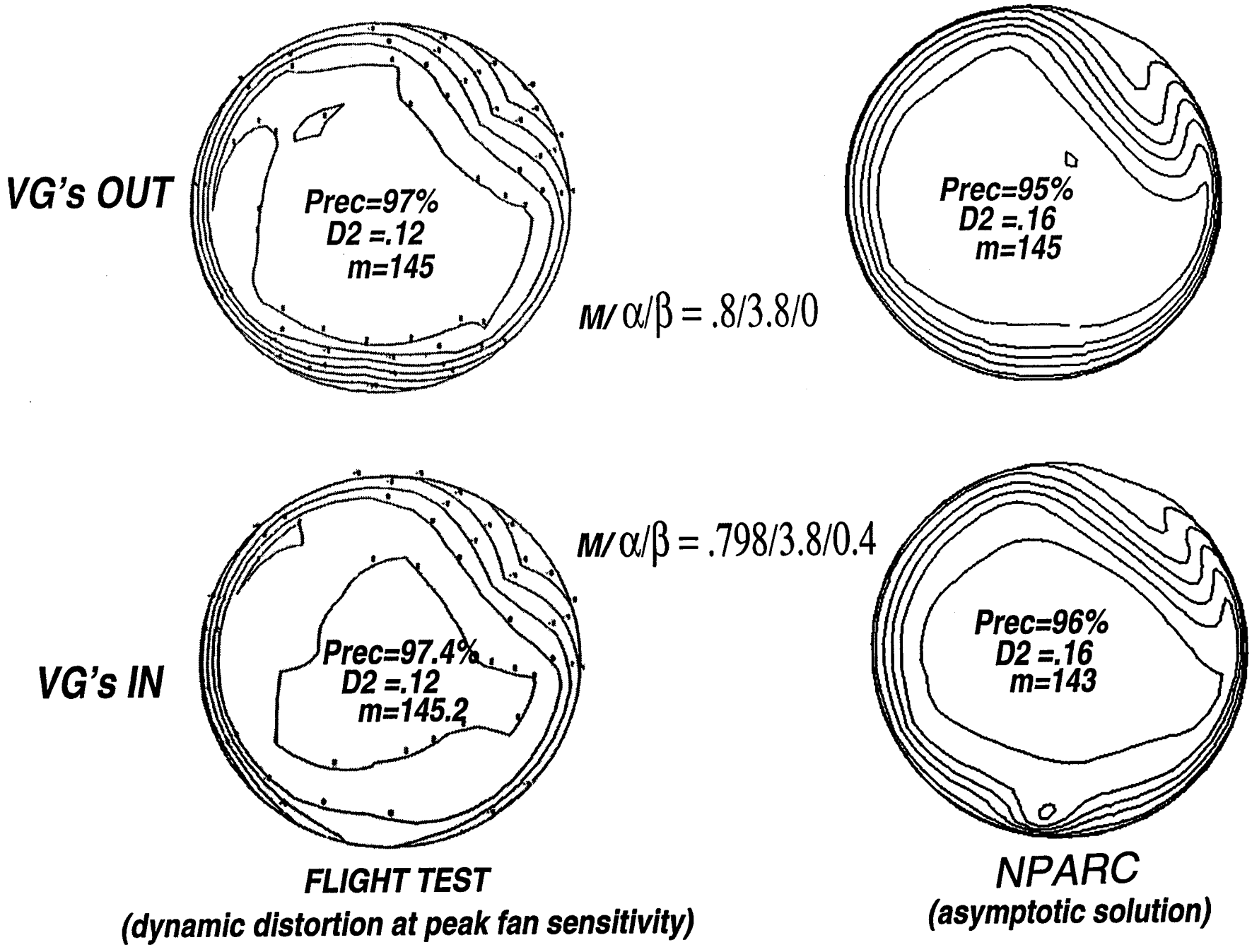

Fig. 16(a) Engine Face Total Pressure Contours

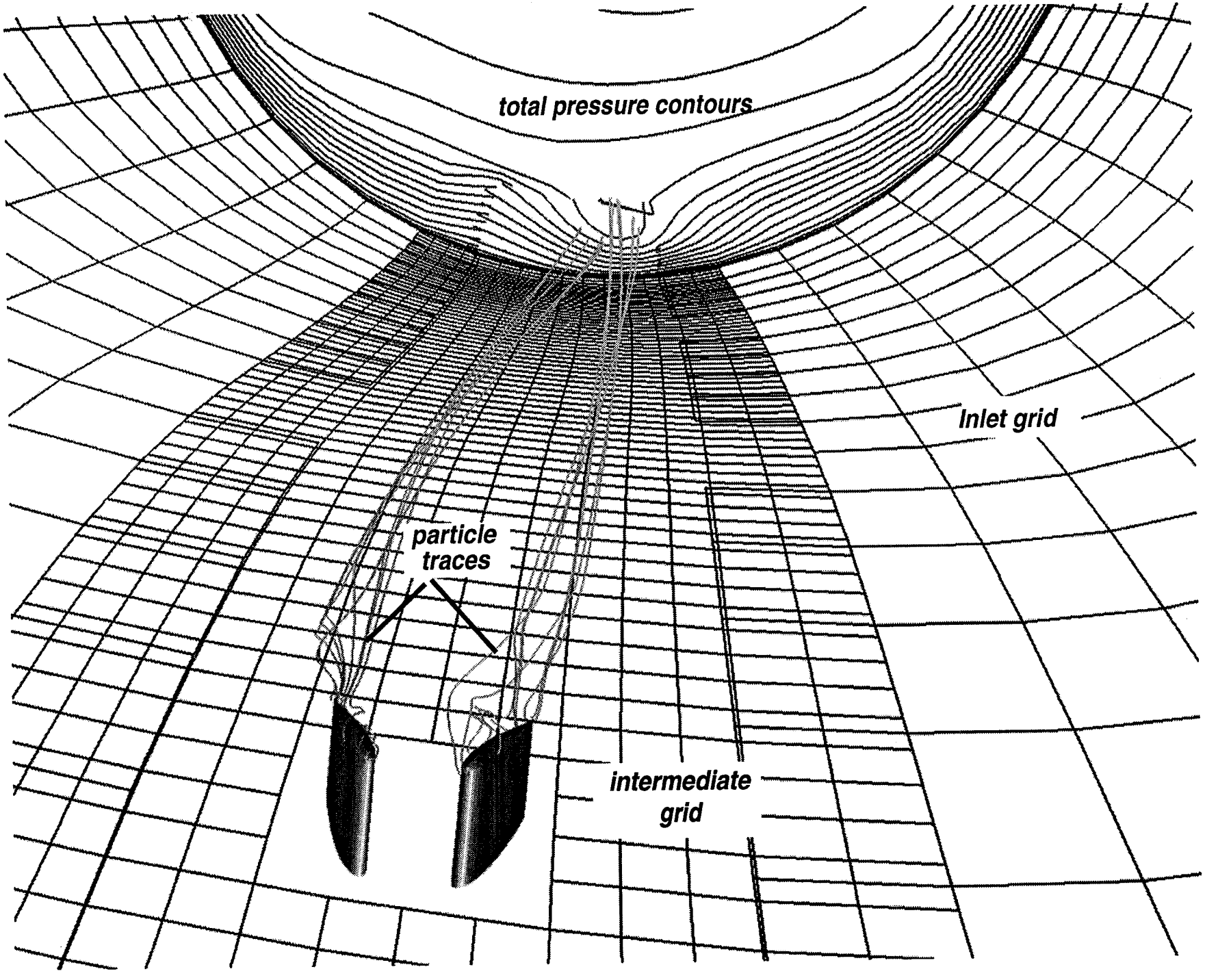

Fig. 16(b) Particle Traces off Vortex Generators

REPORT DOCUMENTATION PAGE

Form Approved
OMB No. 0704-0188

1. AGENCY USE ONLY (*Leave blank*)	2. REPORT DATE	3. REPORT TYPE AND DATES COVERED
	December 1995	Technical Memorandum

4. TITLE AND SUBTITLE
Evaluation of F/A–18A HARV Inlet Flow Analysis With Flight Data
Final Report

5. FUNDING NUMBERS
WU–505–68–30

6. AUTHOR(S)
C. Frederic Smith, Steve D. Podleski, Wendy S. Barankiewicz, and
Susan Z. Zeleznik

7. PERFORMING ORGANIZATION NAME(S) AND ADDRESS(ES)
National Aeronautics and Space Administration
Lewis Research Center
Cleveland, Ohio 44135–3191

8. PERFORMING ORGANIZATION REPORT NUMBER
E–10056

9. SPONSORING/MONITORING AGENCY NAME(S) AND ADDRESS(ES)
National Aeronautics and Space Administration
Washington, D.C. 20546–0001

10. SPONSORING/MONITORING AGENCY REPORT NUMBER
NASA TM–107130

11. SUPPLEMENTARY NOTES
C. Frederic Smith, Steve D. Podleski, and Susan Z. Zeleznik, NYMA Inc., 2001 Aerospace Parkway, Brook Park, Ohio 44142 (work funded by NASA Contract NAS3–27186); Wendy S. Barankiewicz, NASA Lewis Research Center. Responsible person, Wendy S. Barankiewicz, organization code 2780, (216) 433–8706.

12a. DISTRIBUTION/AVAILABILITY STATEMENT
Unclassified - Unlimited
Subject Category 07
This publication is available from the NASA Center for Aerospace Information, (301) 621–0390.

12b. DISTRIBUTION CODE

13. ABSTRACT (*Maximum 200 words*)
The F/A-18A aircraft has experienced engine stalls at high angles-of-attack and yaw flight conditions which were outside of its flight envelope. Future aircraft may be designed to operate routinely in this flight regime. Therefore, it is essential that an understanding of the inlet flow field at these flight conditions be obtained. Due to the complex interactions of the fuselage and inlet flow fields, a study of the flow within the inlet must also include external effects. Full Navier-Stokes (FNS) calculations on the F/A-18A High Alpha Research Vehicle (HARV) inlet for several angles-of-attack with sideslip and free stream Mach numbers have been obtained. The predicted forebody/fuselage surface static pressures agreed well with flight data. The surface static pressures along the inlet lip are in good agreement with the numerical predictions. The major departure in agreement is along the bottom of the lip at 30° and 60° angle-of-attack where a possible streamwise flow separation is not being predicted by the code. The circumferential pressure distributions at the engine face are in very good agreement with the numerical results. The variation in surface static pressure in the circumferential direction is very small with the exception of 60° angle-of-attack. Although the simulation does not include the effect of the engine, it appears that this omission has a second order effect on the circumferential pressure distribution. An examination of the unsteady flight test data base has shown that the secondary vortex migrates a significant distance with time. In fact, the extent of this migration increases with angle-of-attack with increasing levels of distortion. The effects of the engine on this vortex movement is unknown. This implies that the level of flow unsteadiness increases with increasing distortion. Since the computational results represent an asymptotic solution driven by steady boundary conditions, these numerical results may represent an arbitrary point in time. A comparison of the predicted total pressure contours with flight data indicates that the numerical results are within the excursion range of the unsteady data which is the best the calculations can attain unless an unsteady simulation is performed.

14. SUBJECT TERMS	15. NUMBER OF PAGES
Inlets; High angle of attack; Flight	96
	16. PRICE CODE: A05

17. SECURITY CLASSIFICATION OF REPORT	18. SECURITY CLASSIFICATION OF THIS PAGE	19. SECURITY CLASSIFICATION OF ABSTRACT	20. LIMITATION OF ABSTRACT
Unclassified	Unclassified	Unclassified	

END DATE FEB 7, 1996